A Mobile Electrophysiology Board for Autonomous Biorobotics

by

Leslie I. Ortiz

A Thesis Submitted to the Faculty of the

Electrical and Computer Engineering Department

In Partial Fulfillment of the Requirements
For the Degree of

Master of Science

In the Graduate College

The University of Arizona

2 0 0 6

Acknowledgments

Table of Contents

List of Figures

Abstract

Neuromorphic engineering has been taking inspiration from biology to create artificial systems, but up until now none of those systems has been more successful than any biological system. An insect can perform tasks like collision avoidance far more successfully than the most sophisticated artificial system. On the other hand, neuromorphic systems have helped substantially to advance our understanding of behavioral, computational and neurobiological mechanisms in insects, especially those involving sensorimotor control. Hybrid biorobotic systems formed by interactions between biological and artificial systems are an alternative platform for studying those issues. This thesis mainly consists of the development of the interface between the biological and artificial system of a mobile biorobot. This involves the design and fabrication of an electrophysiology amplification, filtering, and data acquisition board tailored to insect recordings. The constructed board produces reliable data comparable to that obtained from commercially available electrophysiology equipment, but because of its size and wireless communication is more suitable for experiments involving mobile robotics. The board was used to collect real-time electrophysiological data from living hawkmoths. The data was processed by the board and it was used to successfully control a mobile robot in a closed-loop environment. The results obtained from this experiment suggest that this platform will work on various experiments of similar nature.

Chapter 1

Introduction

Neuromorphic engineering is a research area that has been inspired by biology to create artificial systems that are successful to a certain extent but that are still outperformed by insects in simple tasks such as small-target tracking or collision avoidance. Overall, building artificial systems that implement biological models has proven to be very useful for testing those models in a more controlled and unified way. However, it might not be necessary to build the entire system artificially. Why not combine biological structures with artificial systems to build a hybrid system where specific biological mechanisms can be better studied, and artificial systems can be improved? For instance, biological sensors have been imitated artificially, but the early processing of the input has proven to be too complex to replicate artificially. The use of biological sensors provides the artificial system with a more sophisticated sensor that allows the system to perform better, and at the same time the early processing in the biological system can be better understood. Figure 1.1 shows an example of a neuromorphic system as well as a hybrid system or biorobot.

This chapter gives an overview of the project. It also gives a review of several investigations of similar nature previously executed. And finally, it gives an overview of the organization of the rest of this document.

1.1 Overview of the Project

This work was motivated by the need for the creation of a well-developed and practical platform for closed-loop experiments that involve hybrid systems formed by living insects and mobile robotics. Figure 1.2 shows an overview of the project. This thesis focuses on the design and construction of two Printed Circuit Boards (PCBs) which constitute the interface between the artificial system (the robot) and the biological system (the insect). Commercially available electrophysiology amplifiers are obviously not suitable for this task because of their size as shown in Figure 1.3. Therefore, a suitable electrophysiology board had to be developed. The required board needed to be small enough to fit on a mobile platform together with the biological system. More importantly, the board needed to record reliable data comparable to data obtained from professional equipment. The first prototype board built in this project handles electrophysiology amplification.

In addition to the electrophysiology board, a data acquisition board is also required for these experiments. Its main purpose is to sample the amplified signal in a real-time manner. This board can also provide a way of processing the data and to compute
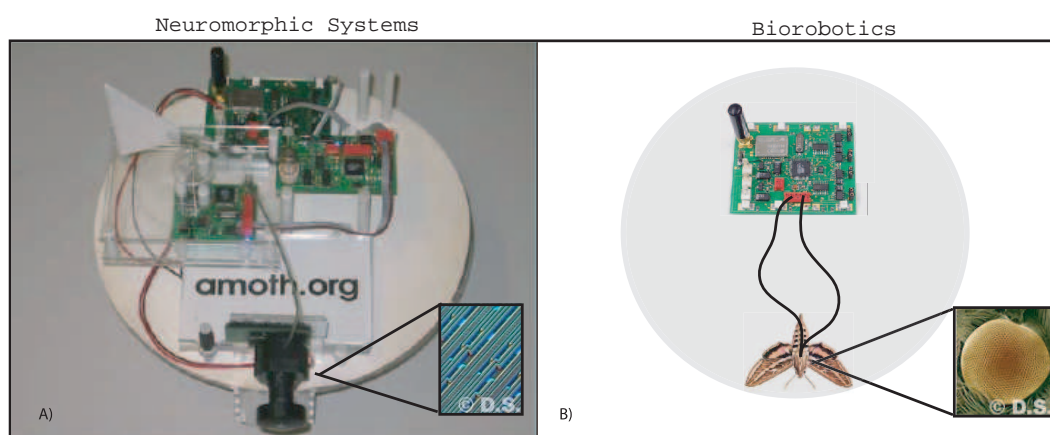
FIGURE 1.1. Neuromorphic engineering versus biorobotics. a) An "artificial moth" called AMOTH. This example of a neuromorphic system consists of a mobile robot platform that implements a neuronal model of a moth optomotor anemotactic search (Pyk *et al.*, 2006). It uses various artificial sensors including a CMOS color camera that acts as an "eye". b) An illustration of a biorobotic system. This system also consists of a mobile platform that implements a particular neuronal model in software or hardware. However, instead of using artificial sensors it uses the real eyes of the moth so that early processing of visual information is done in the brain of the moth. Insets labeled @D.S. were obtained without permission from www.scharfphoto.com.
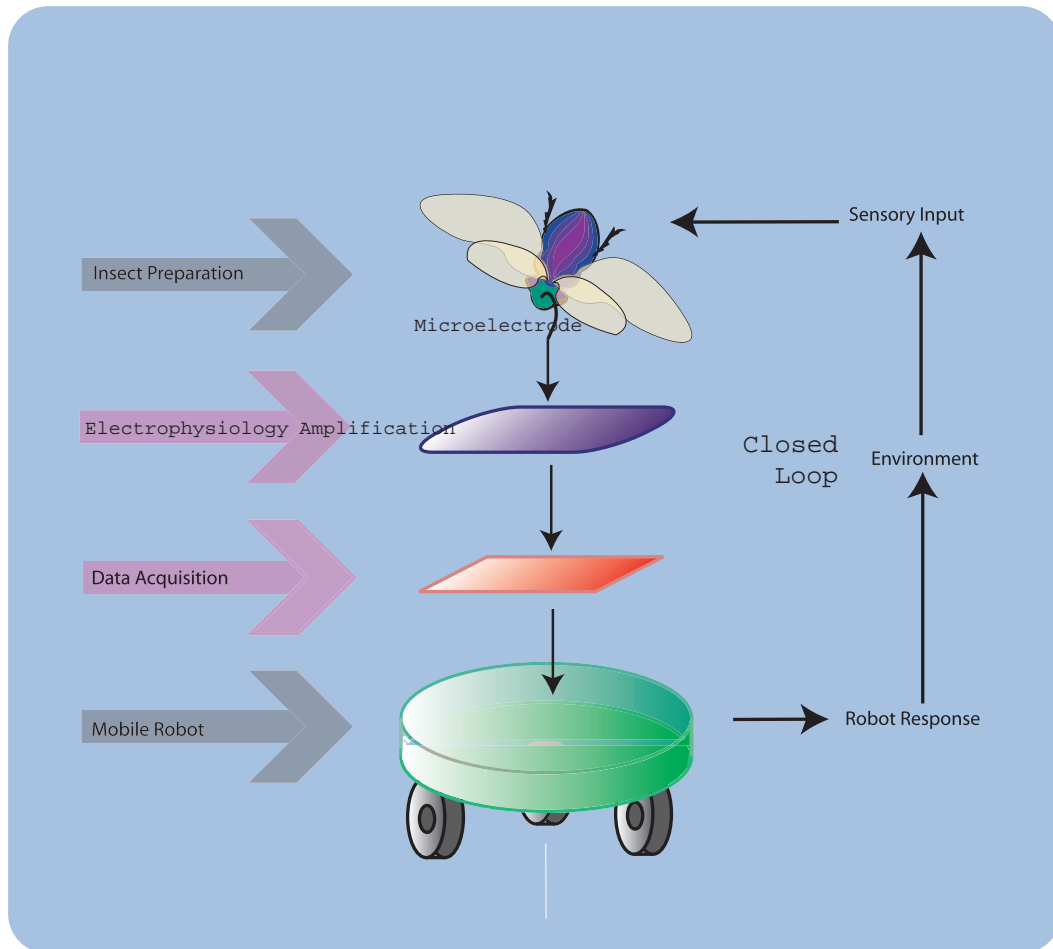
FIGURE 1.2. Overview of the project. A hybrid biorobotic system is developed by interfacing an insect with a mobile robot. The interface is composed of an electrophysiology amplifier and a data acquisition board and it constitutes the work of this thesis. The electrophysiology board will amplify and filter the biological signals obtained from the microelectrodes placed in the insect. The acquisition board will sample the data to digitize it and later use it to compute control signals that will go to the mobile robot. The system will be used in closed-loop experiments.

FIGURE 1.3. Commercially available electrophysiology equipment. a) Axon Instruments data acquisition system for electrophysiology model CyberAmp 380. b) Extracellular electrometer model 1700 from A-M Systems. Dimension: 43.2 cm x 12.1 cm x 28.6 cm. Weight: 19 lbs. Cost: $1,780. c)Intracellular electrometer model 1600 from A-M Systems. Dimension: 43.2 cm x 12.1 cm x 28.6 cm. Weight: 22 lbs. Cost: $1,650.

the control signals for the robot. Wireless communication is also desired to facilitate experiments. The second prototype built in this project combines this functionality with the electrophysiology amplifier in one board.

The system developed in this research work will be used in closed-loop experiments involving Electromyograms (EMG) and neural signals in the hawkmoth.

1.2 Related Work: Biorobotics

The work presented in this thesis involves connecting biological systems to artificial systems in real-time, forming a closed-loop interaction. Significant work previously conducted involving this interaction can be divided into two main categories. The first involves mobile robotics that have a biological sensor or input of some kind, and the second involves implantable devices where the artificial system is a smaller part of the system.

One of the biggest areas of research involving brain-machine interaction is in prosthetics. Currently, there is a lot of research in this field where the investigations often involve small mammals like rats or rabbits (Giszter *et al.*, 2005) and other times involve primates (Chapin, 2004). In Giszter *et al.*, 2005, a cortical or spinal neural interface biorobotic system is developed. The system has the capability of providing real-time control of a robot which attaches to rats or frogs, with the goal of applying forces to the pelvis or hindlimbs by bone implants. Neural signals in this research were obtained with commercially available equipment from AM-Systems, Neuralynx, and Cyberkinetics. The robot used was a Phantom Model T or Model A 1.0 3DOF. A closed-loop experiment was formed between animal and robot as follows. Information from the animal was obtained from electrophysiology data (neural activity and EMG signals) and from force-plates located underneath the animal. The information was sampled and transmitted to a PC were the robot control signals were computed. The robot is attached to the animal, but long wires are used to connect to the equipment, which is what the present project is trying to avoid. Those systems use an expensive apparatus to record and sample electrophysiological signals. Also, there is not a unified integration between the biological system and the electronics. In other words, the animal is separated from the electrophysiology equipment and thus the experiments can only be performed on the lab bench.

In another related project, closed-loop interactions have been created between neural tissue of the Sea Lamprey and a mobile robot to generate autonomous behaviors that help to understand distinctive features of the biological system under study (Reger *et al.*, 2000). A difference between that investigation and the research presented in this document pertains to the type of biological system used; experiments presented in this thesis will involve intact insects, the study in Reger *et al.*, 2000 uses tissue. Their project also uses commercially available equipment (AM-Systems Model 1800 and National Instruments PCI-MIO-16E-4) to collect and process elec-

trophysiological signals (Reger, 2000).

Another type of research related to the work presented involves implanting electrical chips in biological systems for stimulation and amplification of neural activity (Mavoori *et al.*, 2004). In this work a miniature (1 cm x 1.25 cm x 0.25 cm) computer for functional electrical stimulation and amplification of neuromuscular activity was implanted in a freely behaving hawkmoth (*Manduca sexta*). The electrophysiology amplification circuit includes filters that implement a bandpass of 200 Hz - 2.6 KHz, and amplification of 250x to 12000x using Texas Instruments OPA4336 Op-amps. Then the data is sampled by ADCs at 5.8 KSps using a Programmable System on Chip (PSoC) which also implements additional functions including a digital stimulator. A wireless interface is implemented with an infrared (IR) device that has a range of 1 m along the line-of-sight; the system has an on-board memory of 4 Mb. There is a closed-loop system in these experiments since the artificial stimulation affects the neural activity and vice versa (new stimulation is applied based on recorded activity). However, the artificial system involved is not a mobile robot and the type of experiments that can be performed in such system is somewhat limited. In addition, the system has a big limitation due to the lack of a suitable power supply. Batteries currently available weigh enough to impair the hawkmoth flight. Therefore, this system is not completely wireless in spite of the system's IR capability.

The Neurochip BCI (Jackson *et al.*, 2006) is another example of an implantable device which in this case has been used in monkeys. This device measures 5.5 cm x 5 cm x 3 cm and is capable of collecting EMG and neural activity for up to 40 h. The electronics mainly consist of two PSoCs that are sampling at 11.7 KSps, as well as processing the data. Additionally, front-end filtering and amplification are implemented. For neural signals a bandwidth of 500 Hz - 5 KHz and gain of 1500x is provided. For EMG signals a bandwidth of 20 Hz - 2 KHz and a gain of 250x is provided. For both type of signals there is also a variable gain of 1-48x in addition to the previously mentioned. Additionally, the Neurochip incorporates stimulation circuitry that delivers a stimuli of up to 100 μA, it has 8 Mb of memory, and handles the IR communication.

Other similar devices are found in Ando *et al.*, 2002; Neihart and Harrison, 2005. Implantable devices are not optimal for the biorobotic experiments presented in this research since they sacrifice features for minimizing space and power consumption. While size and power consumption are important for this project, the device is not intended for implantation and therefore more space can be allocated. Additionally, the experiments to be performed on this system are not intended to last more than a few hours and therefore power consumption is not as restricted. Ultimately, more features can be implemented when dealing with non-implantable devices.

1.3 Presented Work

This thesis is a collection of findings, experiments, and results gathered throughout a research project of more than a year and a half. It includes background on the topic, description of the designed system, results of experiments performed, and a discussion of the system and future work. The contents of each chapter are described below.

Chapter two talks about electrophysiological signals. This chapter provides the reader with some details of available methods and problems encountered when obtaining extracellular and intracellular signals.

Chapter three is the main core of this thesis. The proposed electrophysiology board is described here from design to fabrication. Two prototypes were constructed during this research and a detailed description of both is included.

In Chapter four, the characterization results of both prototypes are shown. The testing performed on the boards was done with artificial as well as real electrophysiological data, and the results are compared to those obtained from PSpice simulations in the previous chapter.

Chapter five presents closed-loop experiments involving mobile robotics controlled by electrophysiological data recorded using the presented board. The software and hardware tools used on the experiments are described; also included are the results and their implication.

In Chapter six, limitations and possible improvements of the electrophysiology board are discussed to conclude this thesis.

Chapter 2

Electrophysiological Signals

Electrophysiology is the study of electrical signals found in biological systems. It is widely practiced in various biology fields since it provides information at a cellular level pertaining to the structure and function of internal organs as well as information that helps explain behavioral issues. Modern electrophysiology was founded by the German scientist Emil Heinrich Du Bois-Reymond (Du Bois, 2006). His main research was on electrical activity in nerve and muscle fibers, and the collection of his studies created the field (1848-1888). Obtaining electrophysiological data entails having some degree of knowledge of electrical circuit theory as well as of biology. This chapter gives a summary of the basic knowledge required to perform electrophysiology. It introduces the reader to concepts commonly seen when dealing with electrophysiological data; and more importantly, it shows some techniques for solving some of the issues encountered when designing electrophysiological instruments.

Electrophysiology has two major methods of recording: intracellular (inside the cell) and extracellular (outside the cell). In turn, each method has several variations that usually give different results, and therefore each is suitable for particular phenomena. This chapter introduces concepts that are relevant to intracellular and extracellular methods in general, but it will not include all variations of those methods.

An important issue in electrophysiology is that of choosing the proper electrode to perform the recordings. Nowadays, there are a variety of electrodes available and each has specific properties that impose limitations on recordings. Usually a good recording will depend, among other things, on the proper choice of electrode. Because a good understanding of the benefits and drawbacks of using specific electrodes is important, this chapter includes a brief description of the major types of electrodes.

2.1 Insect Electrophysiology

Even though electrophysiology has been around for more than a century, early research did not involve insects due to the limitations inherent to their small size. Since much of neurophysiological research is an application of electronics to biology (Miller, 1979), it is not a surprise that research on insects proliferated as electronics became more advanced and tools easier to manipulate. Early electrophysiology instruments did not have the precision to allow good manipulation of small specimens. In fact, the size and nature of insects still present special problems to the student of entomology in general (Miller, 1979). However, electrophysiology of invertebrate systems also has

a lot of advantages. First of all, although most insect neurons are quite small, some nerve cells are larger and easier to identify (often $10 - 50\mu$ in diameter Dichter, 1973) than in vertebrates. In addition, specimens do not need anesthesia prior to the procedure. Another advantage is that it is possible to isolate the part under study and thus eliminate problems involved when recording from whole animals. This control of recording conditions makes the recordings really stable, making it relatively easy to record for long periods of time with consistent results. Overall, the relative simplicity of their structure compared to other animals makes insects ideal candidates for electrophysiology studies.

The following sections cover the topics that are crucial for a good understanding of the next chapter. However, the general topic is not covered in depth. More information on electrophysiological methods can be found in numerous publications including Bures, 1962.

2.2   Intracellular Recordings

Intracellular recording is characterized by the penetration of the cell by the electrode (see Figure 2.1). These recordings are known to be very powerful as far as providing a lot of information about the cell because the change in potential is recorded from the inside and the Signal to Noise Ratio (SNR) is very high. On the other hand the complexity involved in this method demands more complex hardware than extracellular recording. In the following subsections some major technical challenges pertaining to this method are explained.

2.2.1   Microelectrode Resistance

One of the major parameters of microelectrodes used for intracellular recording is their tip resistance. Resistance in this context can be determined by injecting a small current (nA) through the electrode and measuring the change in voltage. The electrode resistance is then defined as the change in potential of the electrode divided by the injected current. This value will depend on several factors including the size of the electrode tip. The microelectrodes need to have a tip size smaller than the cell to be able to penetrate without inflicting significant damage. Finely drawn glass micropipettes are usually used for this task (Dichter, 1973); their resistance is proportional to the tip diameter and to the thickness of the walls. Specifically, the resistance is higher for smaller tip diameters and for micropipettes with thicker walls. In other words, having thinner walls yields lower resistance for a given outside tip diameter. It should be noted that the thickness of the wall also determines the strength and flexibility of the pipette, and therefore it is important to choose the proper thickness. Typical resistance values for a glass micropipette with a $500nm$ tip are in the range of $10 - 50M\Omega$ (Dichter, 1973); micropipettes with smaller tips ($50 - 120nm$) can have a resistance as high as $200M\Omega$ (D. O'Carroll, personal communication, 2006).
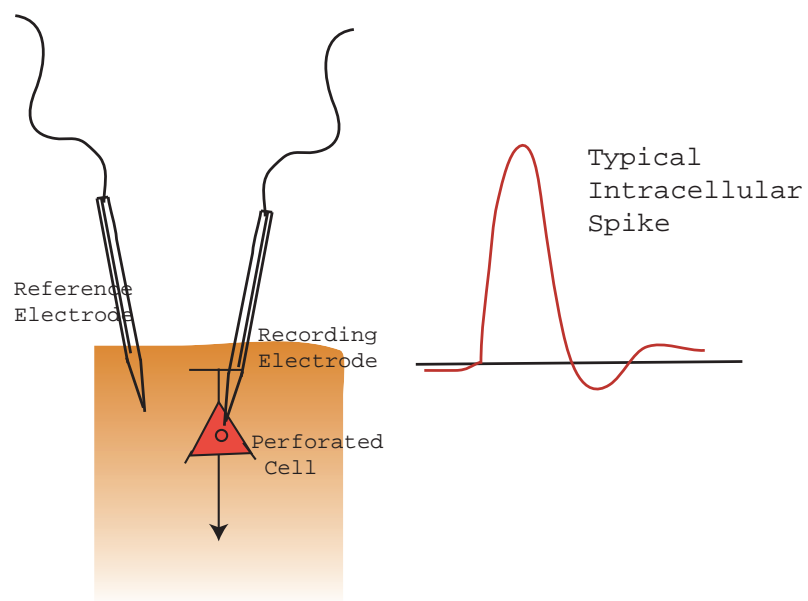
Figure 2.1. Intracellular recording method. A very sharp electrode is introduced into the biological tissue until a cell is penetrated. The reference electrode is placed in the tissue somewhere close to the recording electrode. A typical intracellular spike has a protuberant positive part and then a smaller negative portion.

This presents a potential problem associated with recording intracellular potentials. Figure 2.2 illustrates how a voltage divider is formed by the electrode resistance and the first stage input resistance. The problem occurs when the electrode resistance, R_e, is much higher than the input resistance, R_i, and thus takes most of the voltage drop across it. The recording amplifier will only see a small fraction of the true intracellular potential and it would probably be significantly distorted by noise because of its extremely small magnitude. This problem can be avoided if the first stage of the electrophysiology board has an input resistance 100 or 1000 times higher than the electrode (Purves, 1981).
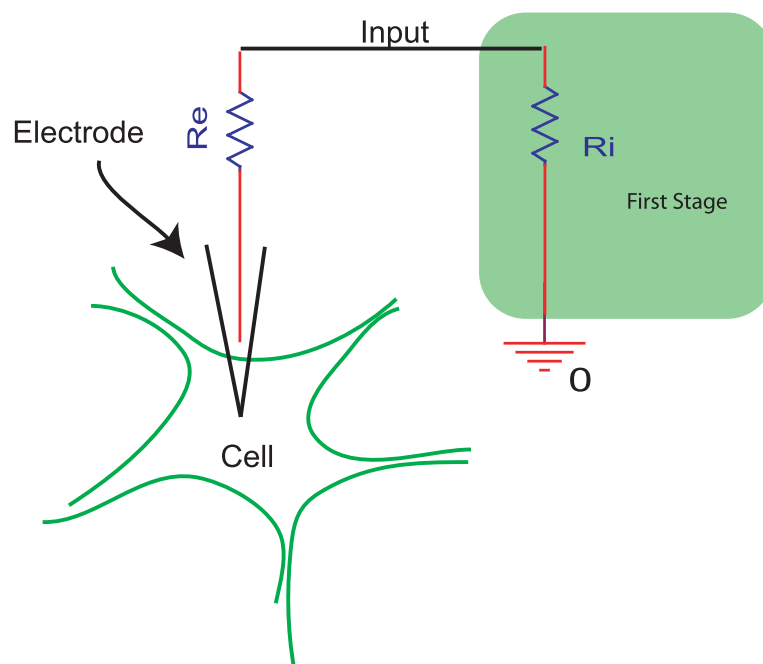
FIGURE 2.2. Illustration of voltage divider effect occurring between the electrode high resistance R_e and the first stage input resistance R_i. If the first stage of the amplifier has an input resistance much lower than the electrode resistance $(10 - 50M\Omega)$ V_e, the voltage drop across R_e will be most of the signal and the input to the first stage will only be a small fraction of the true intracellular potential and could be significantly distorted by the noise inherent in the amplifier.

Even when the resistance is very high at the input of the amplifier, there will be a voltage drop across the electrode. This voltage will depend on the current going through the electrode; therefore, one would like to minimize it. A microelectrode with resistance of $10M\Omega$ and with a current of 100nA will produce a voltage of 100mV, which is more than enough to produce biological effects in the cell under

study (Dichter, 1973). To avoid this, the first stage components must have small input current ratings (much less than 1 nA).

2.2.2 Capacitance

There are various sources of capacitance in the recording setup. This capacitance together with the electrode resistance forms a low-pass filter that prevents the propagation of high frequencies and, thus, creates distortion of the signal.

First, there is the transmural capacitance C_t, which is the capacitance formed in a micropipette between the solution inside the pipette and the biological tissue. This is a distributed capacitance modeled as being made out of individual elements (see Figure 2.3) and there is usually no way to eliminate it. Nonetheless, it can definitely be reduced by using solutions that are of similar components as those in the biological tissue. This unwanted capacitance may range from less than 1 pF to 10 pF or more (Purves, 1981).
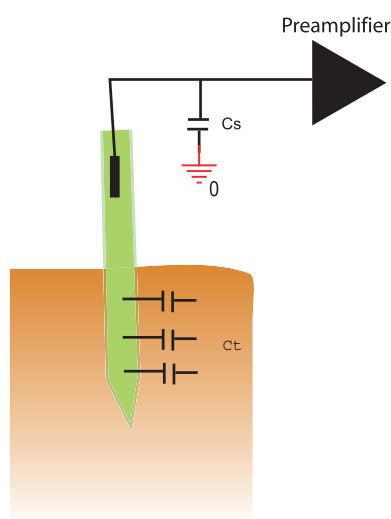
FIGURE 2.3. Undesired capacitances in intracellular recording. This figure shows a simplified model of the capacitance introduced by the recording electrode when inside the biological tissue. First there is a transmural capacitance C_t which is formed across the micropipette between the solution inside and the solution in the biological tissue. This is a distributed capacitance modeled as being composed of multiple elements; only three are shown in this figure. The other significant capacitance is the stray capacitance C_s that originates at the microelectrode's stem and the lead joining it to the preamplifier. This is a capacitance with respect to ground.

The other capacitance of significance is a stray capacitance C_s that originates in the microelectrode's stem and the lead joining it to the preamplifier (Purves, 1981).

The value of this capacitance depends on the length of the joining lead (usually a few pF) and can be significantly reduced by placing the first amplifier stage as close as possible to the electrode.

Usually, both unwanted capacitances add up to less than 20pF (Purves, 1981). They can be overcome by a specialized circuit in the electrophysiology board that provides negative capacitance, as later explained in this section.

The undesired effects on the recorded signal can be explained as distortion due to the transient flow of current through C_{tot}, which is the total unwanted capacitance. This loss cannot be prevented but it can be compensated by supplying the lost current from another source. The circuit required to supply precisely the right amount of current uses a capacitor and it is said to create "negative capacitance". Figure 2.4a shows an example of such a circuit. The voltage across C_f is $V_{in}(A - 1)$ and by definition the current going through C_f is:

$$I_{cf} \quad = \quad C_f \cdot \frac{dV_{in}}{dt} \cdot (A - 1) \tag{2.1}$$

The desired current is the current flowing through the capacitance formed in the microelectrode (C_s and C_t) is defined as:

$$I_{cs} \quad = \quad C_{tot} \cdot \frac{dV_{in}}{dt} \tag{2.2}$$

where C_{tot} is the combination of C_s and C_t. By equating 2.1 and 2.2, we obtain the following relationship:

$$C_f \cdot (A - 1) \quad = \quad C_{tot} \tag{2.3}$$

If we have the value of C_{tot}, we could just assign a value to C_f and calculate the adequate gain A for the amplifier. Unfortunately, finding C_{tot} is not easy at all; instead, there are methods of finding out if the compensation is done right. One method is to include a current pump circuit in the electrophysiology board so that a constant pulse of current can be injected into the electrode while the voltage at the input is observed. Figure 2.4b shows several waveforms where the voltage ranges from bad to proper compensation. The idea is that at the beginning of each recording the gain A is adjusted until optimal compensation is achieved. If there is undercompensation, the waveform will show signs of capacitance. If there is overcompensation, the signs are overshoot and oscillation.

Finally, other things that can be used to decrease undesired capacitance are using short wires to join the electrode to the amplifier and avoiding insertion of the tip of the microelectrode too deeply in the tissue.

2.2.3 Other Issues

There are other things that need to be taken into account when performing intracellular recordings. An important one is the concept of tip potential. The potential
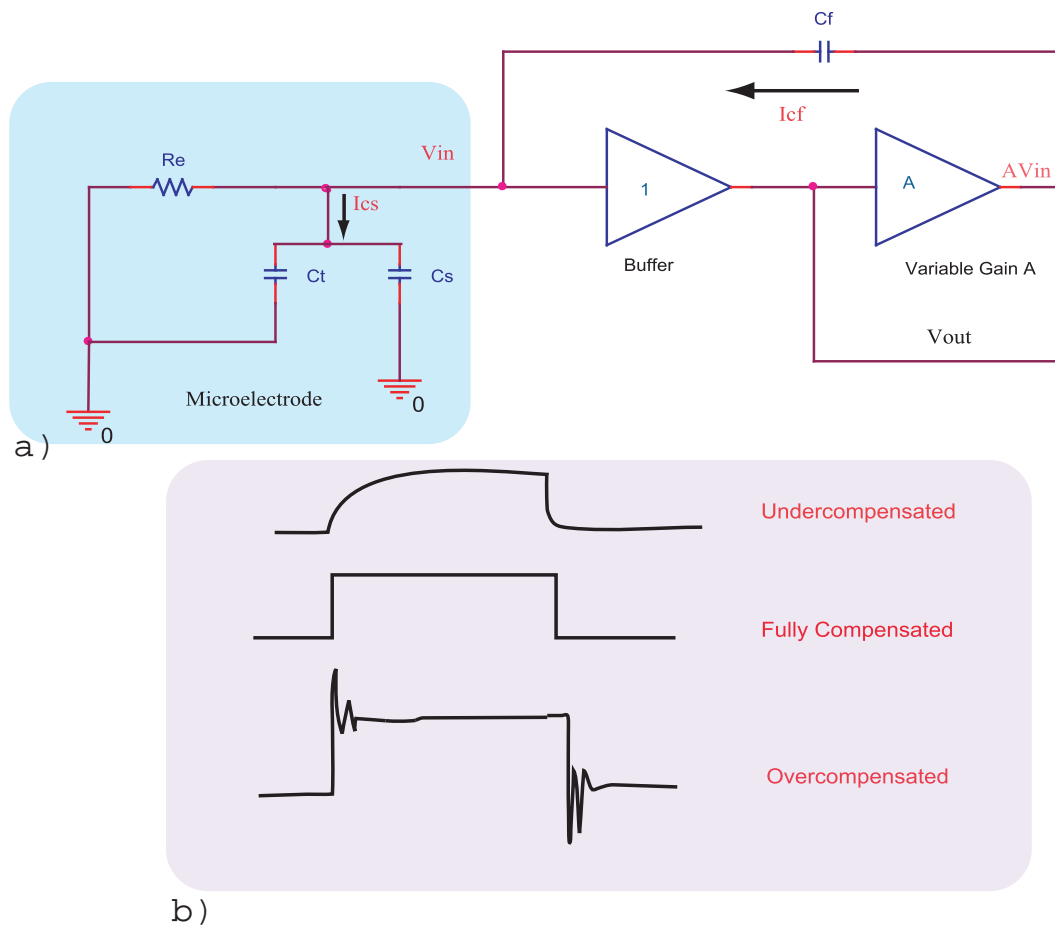
FIGURE 2.4. Negative capacitance. a) A specialized circuit to provide "negative capacitance" to compensate for the undesired capacitance introduced by the microelectrode. The main idea is to provide a current I_{cf} of equal amount as I_{cs} that is lost through C_t and C_s. The gain A of the amplifier controls the amount of current provided. b) In order to know when the right amount of current is being provided, the shape of the input voltage is observed while a current pulse of a few nA is being injected into the microelectrode. The different shapes indicate if the capacitance has been undercompensated, fully compensated, or overcompensated.

recorded by the electrode when inserted in the extracellular fluid is usually not zero (as expected) but there is some offset present called tip potential. Tip potentials have three components: the liquid junction potential, potentials formed by dissimilarities between the electrode and the indifferent electrode, and an additional potential that is found at the tip.

The liquid junction potential is formed between the microelectrode's filling solution and the extracellular electrolyte (Purves, 1981). This can be minimized by choosing the proper filling solution which is not in the scope of this document. The second component involving dissimilarities between electrodes is mainly due to the placement of the electrode inside the preparation and can be minimized by placing the indifferent electrode in a way such that the extracellular chemistry as seen by the electrodes is similar. Symmetry of the electrodes is also very important. The last component in tip potentials is unwanted offsets present at the tip of the micropipette. This potential is different for different microelectrodes, but it can be calculated by breaking the tip of the micropipette at the end of the experiment. When the tip is carefully broken, this unwanted tip offset disappears; therefore, it can be defined as the difference of the potential recorded by an intact microelectrode and the potential after the tip has been broken (Purves, 1981). Overall, tip potentials have a negative sign and a magnitude of about -70mV (Purves, 1981). They are often confused (or combined) with the liquid junction potential since they seem to be abolished when the inside and outside solutions in the pipette are the same.

In practice, instead of reducing tip potentials it is easier to compensate for them by adding an offset control circuit to the recording apparatus.

2.3 Extracellular Recordings

Extracellular recording is performed when cells are not penetrated by the electrode and electrical signals are recorded from the outside of the cell (see Figure 2.5). Besides the recording electrode, a reference electrode is placed somewhere close in the tissue and it is used as the reference signal in the recording circuit.

Signals recorded by this method have particular properties that differentiate them from intracellular signals. First of all, the signals are much smaller (μV) than those recorded from inside the cell (mV). In fact, their magnitude depends on how close the electrode is from the cell as shown in Figure 2.6. Moreover, the polarity of the signal is reversed due to the fact that it is recorded from across the membrane. When positive potential occurs inside the cell, there is a transfer of positive charge (cations) from outside into the cell, leaving a negative charge (anions) outside the membrane. This results in an inverted image of the intracellular recording. This method has several variations and therefore you can obtain different results depending on several factors. For instance, the size of the electrode has a big impact on the recordings. If the electrode used has a tip of the same magnitude as the cells (a few microns), the
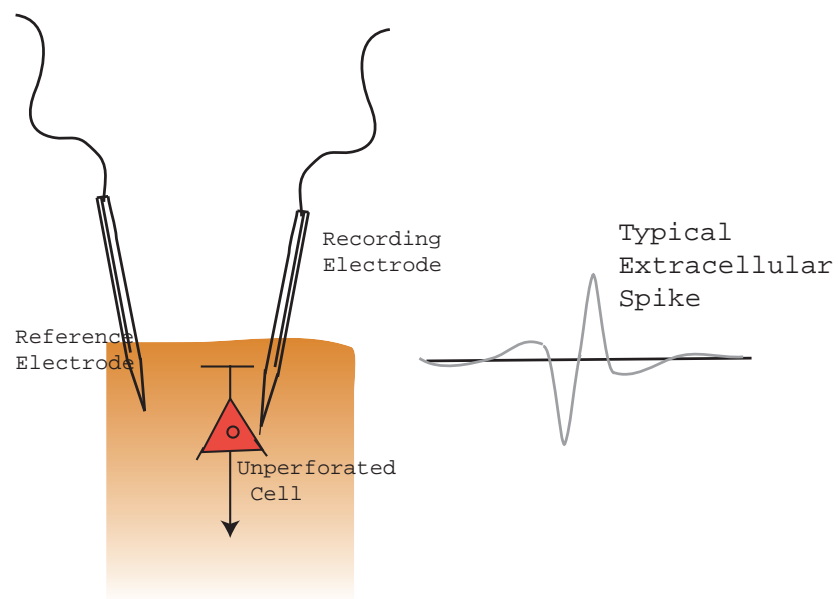
Figure 2.5. Extracellular recording method. The electrode is placed close to the cell without penetration as seen in Figure 2.6. The reference electrode is placed in the same tissue close to the recording electrode. Typical spike signals recorded using this method will have an opposite polarity from spikes recorded intracellularly.
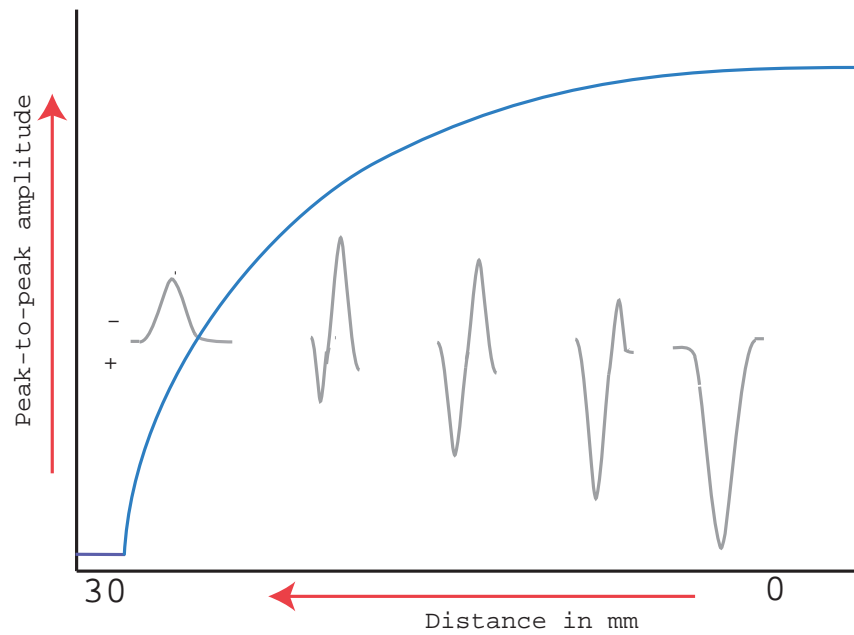
FIGURE 2.6. Microelectrode placement in extracellular recordings. The spikes recorded using this method will have different shapes according to how close the electrode is to the cell. If the electrode is too far away from the cell, the signal will have a very small magnitude (negative). On the other hand, if the electrode is placed too close to the cell, it could end up damaging or penetrating the cell. Ideally, the electrode must be placed around $15\mu m$ away from the cell. Reproduced after a figure from Towe, 1973.

action potentials detected belong to a single cell (Snodderly, 1973) and it is called single-unit recording. On the other hand, if the electrode has a bigger tip, it is more likely that the extracellular signals recorded come from multiple cells, which gives the term multiple-unit recording (Buchwald *et al.*, 1973).

In general, extracellular recordings do not encounter most of the technical complications found in the intracellular case. Usually, data obtained with this method are used merely as an indication of cell activity or the lack thereof. Consequently, signal distortion is not so crucial and signal detection is sufficient in most of the cases.

2.4   Noise in Recordings

In order to obtain good extracellular or intracellular recordings, external noise should be avoided. Some of the noise sources can be suppressed but others can be only reduced. This section talks about the most significant ones and introduces methods to avoid them as much as possible.

It should be mentioned that noise associated with the electrode is often dominant in electrophysiological recordings (The Axon Guide, 1993) and the thermal voltage noise is the most important. Usually that noise is not easy to control and mostly has to do with the physics of the electrode (The Axon Guide, 1993).

The first source of external noise that needs to be considered is the electrical noise from 60Hz power lines (hum). This is interference of 60Hz and harmonics from power supplies, fluorescent lights, etc., that are present especially in laboratories where electrical equipment is abundant.

Another source of noise that might also be present in the recording environment is mechanical interference from motors, radio and television stations, and computer monitors which produce timing signals at 16kHz or higher (The Axon Guide, 1993).

These external noises can be kept at a minimum by correctly grounding the recording setup, shielding the signal, and filtering. Filtering is always necessary when recordings are to be converted to digital data so that aliasing is prevented, and the bandwidth of the filter is chosen based on how fast the resolution needs to be. However, when noise is present at high or low frequencies (outside the signal's main frequencies), filtering is also used. In this case, the bandwidth needs to be chosen so that noise is reduced to acceptable levels while the desired signal can be sampled at a reasonable rate.

Another source of significant noise, especially in intracellular recordings, is vibration. In order to minimize this noise, special tables with vibration isolation can be used.

Finally, other common techniques for avoiding noise include using a shielded input cable, using short connecting cables, using common grounds, disconnecting unused electrical devices and lights, and the use of a shielded cage around the recording preparation.

2.5 Microelectrodes

Electrodes convert ionic current in solution into electron current in wires (The Axon Guide, 1993). Therefore the materials used to make electrodes are those that will have a reaction with the ions in the solution. For instance, when the solution contains chloride ions (Cl^-) and the electrode material is a silver (Ag) wire coated with silver chloride ($AgCl$), the following reaction is formed:

$$Cl^- + Ag \quad \Leftrightarrow \quad AgCl + e^- \tag{2.4}$$

The reaction produces $AgCl$ and the free electrodes dictate the current. In extracellular recordings two commonly used microelectrodes are those made of platinum and tungsten. The platinum electrodes normally give stable recordings, good isolation, and high signal to noise ratio (Snodderly, 1973). These platinum electrodes are suitable for most recording situations except when fine tips are required because they are considerably fragile. Tungsten electrodes are also commonly used. They are very stiff and also give stable recordings. However, tungsten electrodes have a major flaw when using small tips for single-cell isolation because they tend to get noisy at low frequencies (Snodderly, 1973). These electrodes are still the best option when the signals of interest are fast and a high-pass filter can be used without losing the signal.

In intracellular recordings, glass micropipettes with small tips filled with conducting solutions are used to penetrate cells. Then a silver wire (electrode) coated with silver chloride is immersed in the solution to create electrical contact to the recording device.

CHAPTER 3

AMPLIFICATION, FILTERING AND DATA ACQUISITION FOR ELECTROPHYSIOLOGY

This chapter describes the design and construction of two electrometer boards for electrophysiology. The prototype boards consolidate the major stages of a commercially available electrophysiology apparatus in a single printed circuit board minimizing the space required to perform electrophysiology, thus facilitating mobile experiments. The first part of this chapter presents the collection of circuits used in both prototypes. In order to perform intracellular and extracellular recordings, two separate set of circuits were implemented, each with the required features as described in Chapter 2. These circuits were directly obtained from Rivera-Alvidrez, 2004, and are presented in Sections 3.1.1 and 3.1.2 of this chapter. It should be noted that those circuits were previously simulated but they were never implemented with real components prior to this work. In addition to the intracellular and extracellular channels, this chapter details the design of spike detection and spike rate detection circuitry in Section 3.1.3. These analog circuits were designed to facilitate specific mobile experiments that were conducted during this research (Chapter 5). Simulation results from all analog circuits previously mentioned are presented in Section 3.2.

Digital design was also involved in the construction of the final board to incorporate data acquisition capability and wireless programmability. Sections 3.3.1 and 3.3.2 cover those features respectively. Finally, Section 3.4 describes the complete layout and construction process of the two printed circuit boards that were prototyped during this research. The first prototype board consists of pure analog circuitry for extracellular and intracellular recordings. The second prototype board contains only extracellular channels with the incorporation of the spike detection and rate computation circuitry, as well as digital circuitry for data acquisition and wireless programmability.

3.1 Analog Design

3.1.1 Extracellular Electrometer Channel

Recording extracellular signals presents various challenges inherent to some of the signal's characteristics as discussed in Chapter 2. Mainly, the goal is to achieve large amplification minimizing the noise and maximizing the recording bandwidth. In order to accomplish this, extra care must be taken in selecting suitable components. The circuitry must have large amplification and filtering to suppress undesired frequencies

(high and low). Additionally, a notch filter should be included to attenuate 60 Hz electrical noise (hum) as much as possible.
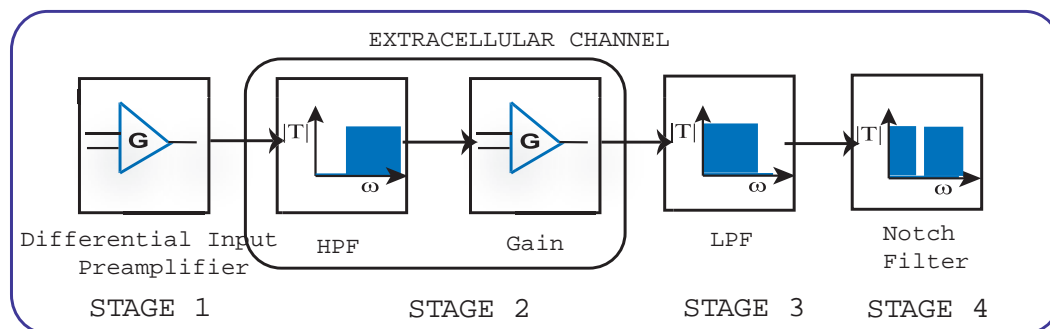
FIGURE 3.1. Extracellular channel block diagram. The first stage is a differential input amplifier with a small optional gain whose main purpose is to transition from very high microelectrode resistance to very low output resistance while maintaining the signal undistorted. This amplifier needs to have an input resistance much higher than the microelectrode resistance. The second stage is a high-pass filter which eliminates DC drift from the signal. Additionally, this stage amplifies the signal for further processing. In the third stage a low-pass filter attenuates high frequency noise. Lastly, the final stage shows a notch filter that prevents 60 Hz noise from interfering with the signal.

The design of the extracellular channel was obtained from an independent study report by Zuley Rivera Alvidrez (2004). The report contained some analysis of circuits suited for this task. The final two versions of the electrophysiology board presented in this document contain all of these circuits with minor modifications.

The extracellular channel can be conceptually divided into four parts as shown in Figure 3.1: differential input preamplifier, high-pass filter with gain, low-pass filter and notch filter. The first concern presented when designing this channel was the gain bandwidth restrictions of the available components. According to relevant literature in the field (Dichter, 1973; Bures, 1962; Purves, 1981), the board should have a bandwidth of around 10 KHz. Amplifiers usually have a gain bandwidth not greater than 1 MHz, therefore the maximum gain that a single amplifier can provide would be 100. In order to provide the required gain (at least 1000) the amplification had to be divided into several stages. For the purpose of this document the extracellular channel design is separated into four separate stages.

Differential Input Preamplifier The first stage consists of a differential input amplifier. The criteria for a good preamplifier is to have low input capacitance, low noise level, and high input resistance (Snodderly, 1973). For this purpose, this stage should be as close as possible to the microelectrode. In fact, it is also called a "head stage" because it is placed on the head of the animal when performing electrophysiology recordings

on bigger animals. In this stage the noise must be kept strictly at a minimum since it is here where the signal is the smallest (typical recorded signals are 10μV to 500μV in amplitude (The Axon Guide, 1993)). In order to meet the criteria previously mentioned, an instrumentation amplifier with high Common Mode Rejection Ratio (CMRR) is used as the differential amplifier (Purves, 1981). This stage is DC coupled allowing for better CMRR. Additionally, since the DC offset at the input terminals is going to get amplified by this stage, the gain must be small in order to prevent saturation. The schematic symbol of an instrumentation amplifier is shown in Figure
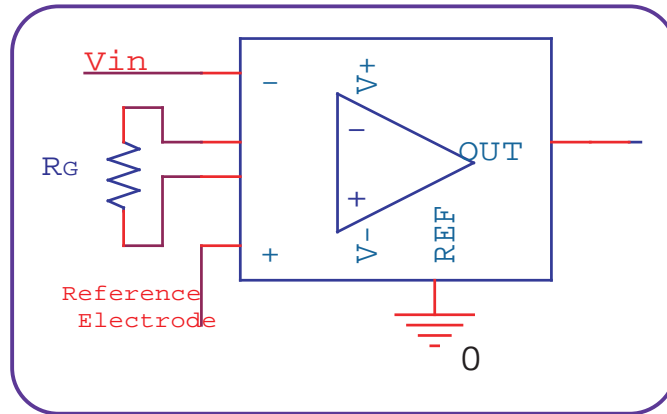
FIGURE 3.2. Extracellular channel first stage. This stage is implemented as a differential input using an instrumentation amplifier with a high CMRR and an input resistance much higher than the microelectrode resistance. The negative terminal input is connected to the recording electrode while the positive terminal input is connected to the reference electrode. This stage must be as close as possible to both electrodes. The resistor R_G determines the gain of this stage as shown in Equation 3.1.

3.2. The internal circuit of an instrumentation amplifier is not in the scope of this discussion but the transfer function can be obtained from the datasheet specific to the used component. In the case of the INA121 from Texas Instruments the relation between the gain of the preamplifier G_{pre} and the resistor R_G is as follows:

$$R_G = \frac{50K\Omega}{G_{pre} - 1} \tag{3.1}$$

In order to have a gain (G_{pre}) of 10 the value of the resistor R_G must be $5.56K\Omega$.

High-Pass Filter With Non-Unity Gain For the next stage, a second order high-pass filter was desired in order to provide good attenuation (-40dB/decade) on frequencies lower than the cutoff frequency (ω_0). For this purpose two cascaded AC-coupled

high-pass filters with non unity gains were designed as seen in Figure 3.3. A single pole high-pass filter has a transfer function T_1 specified as:

$$T_1(s) = -\frac{R_2 C_1 s}{1 + R_1 C_1 s} \tag{3.2}$$

$$= G_1 \cdot \frac{s}{\omega_{0_1} + s} \tag{3.3}$$

From Equations 3.2 and 3.3 we can easily obtain the passband gain (G_1) as well as the cutoff frequency (ω_{0_1}) as follows:

$$G_1 = -\frac{R_2}{R_1} \tag{3.4}$$

$$\omega_{0_1} = \frac{1}{R_1 C_1} \tag{3.5}$$

Now, if we add a second high-pass filter at the output of the first we obtain a transfer
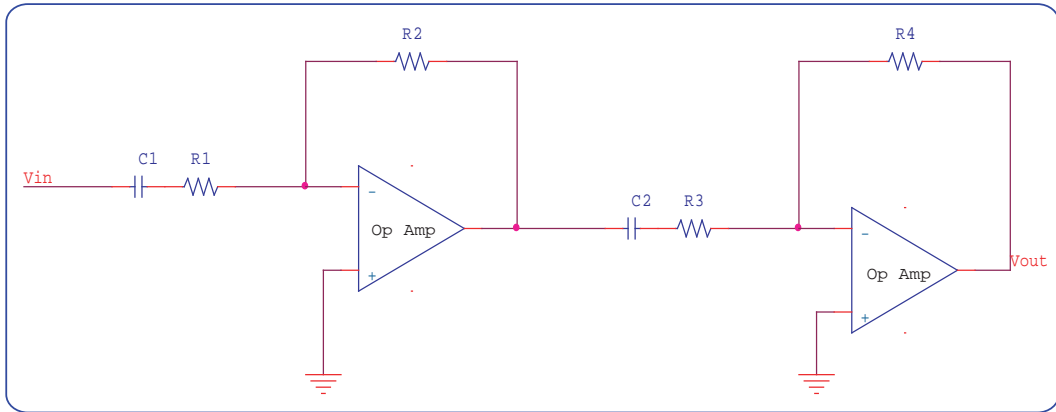
FIGURE 3.3. Extracellular channel second stage. This stage is formed by two cascaded high-pass filters creating a second order filter. To simplify the design the cutoff frequency of both circuits is the same as determined by Equation 3.5. Each high-pass filter has a separate gain which determines the gain of the stage to be the product of R_2 and R_4 over R_1^2.

function which is the product of their separate transfer functions. Figure 3.3 shows the cascaded filters and their transfer function is:

$$T(s) = G_1 \cdot G_2 \cdot \frac{s^2}{s^2 + (\omega_{0_1} + \omega_{0_2})s + \omega_{0_1} \cdot \omega_{0_2}} \tag{3.6}$$

The cutoff frequency of the second high-pass filter in Figure 3.3 is $\omega_{0_2} = \frac{1}{C_2 R_3}$ and the gain is $G_2 = -\frac{R_4}{R_3}$. Therefore the cutoff frequency of the cascaded filters is defined as:

$$\omega_0 = \frac{1}{\sqrt{C_1 C_2 R_1 R_3}} \tag{3.7}$$

In order to maintain the cutoff frequency shown in Equation 3.5, we set $R_3 = R_1$ and $C_2 = C_1$. Then, Equation 3.6 can be simplified as:

$$T(s) \;\; = \;\; G \cdot \frac{s^2}{s^2 + 2 \cdot \omega_{0_1} \cdot s + \omega_{0_1}^2} \tag{3.8}$$

$$G \;\; = \;\; \frac{R_2 R_4}{R_1^2} \tag{3.9}$$

While the cutoff frequency stays the same after adding the second filter, the gain can be determined by changing R_2 and R_4. These two resistors can be assigned separately and the combination of them will result in various gains as shown in Equation 3.9.

The required cutoff frequency for this stage depends on several factors including the noise existent at the moment of recording as well as the type of signals that are to be recorded. On one hand, if recording spike signals, noise contamination or DC drift can be avoided by attenuating small frequencies. On the other hand, excessively high cutoff frequencies will radically distort spike signals. A good option is to have multiple cutoff frequencies so that the user can experiment which one will work better for specific recordings. Ultimately, the cutoff frequencies included as suggested in Rivera-Alvidrez, 2004 are 20 Hz and 300 Hz. These cutoff frequencies are accomplished with resistor $R_1 = 100K\Omega$ and a capacitor C_1 that can be selected from two values by a switch. The values are 124 nF to make a 20 Hz high-pass filter and 5.1 nF to obtain a cutoff frequency of 300 Hz.

The output signal of the board is likely further processed by a digital device and thus must go through an Analog to Digital Converter (ADC). In order to minimize the noise contamination during further processing of the signal the amplitude must be as large as possible with the restriction that most ADCs have an input range of 5V. Taking this into account the first high-pass filter was designed to provide selectable gains of 10x or 100x and the second high-pass filter gains of 1x, 10x or 25x. Therefore the total gains available on the board (including stage one and two) are: 100x, 1000x, 2500x, 10000x or 25000x. These gains adequately amplify signals in the range of $50 \mu V$ to 50 mV.

Low-Pass Filter The third stage is composed of a low-pass filter with unity gain. A second order Sallen and Key Butterworth low-pass filter was chosen for this stage
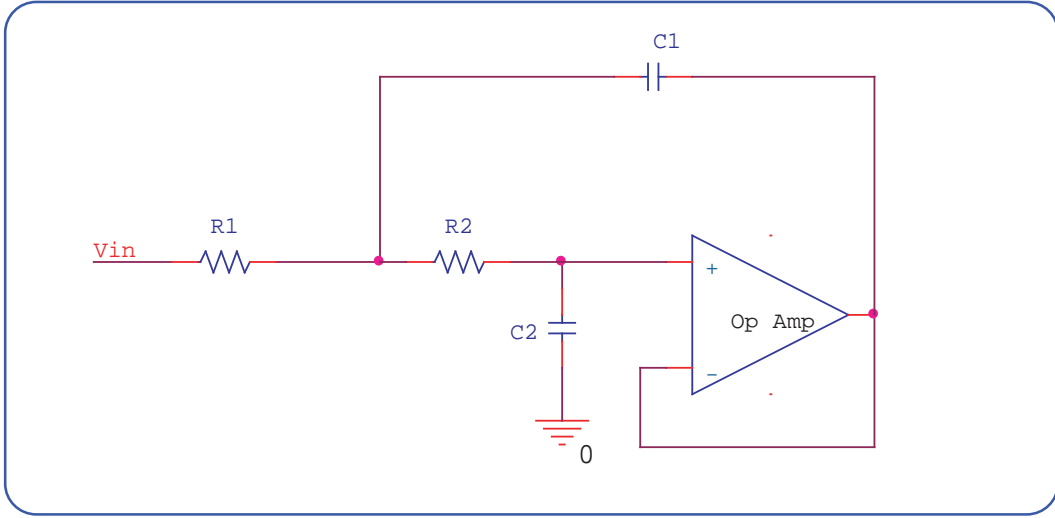
FIGURE 3.4. Extracellular channel third stage. This stage consists of a second order Sallen and Key Butterworth low-pass filter. The cutoff frequency is determined as seen in Equation 3.12. This stage has a unity gain.

(see Figure 3.4) and the transfer function is defined as:

$$T(s) = \frac{1}{C_1 C_2 R_1 R_2 \cdot s^2 + (R_1 C_2 + R_2 C_2) \cdot s + 1} \tag{3.10}$$

$$T(s) = \frac{\omega_0^2}{s^2 + \left(\frac{\omega_0}{Q}\right) \cdot s + \omega_0^2} \tag{3.11}$$

$$\omega_0 = \frac{1}{\sqrt{R_1 R_2 C_1 C_2}} \tag{3.12}$$

$$Q = \frac{1}{R_1 + R_2} \cdot \sqrt{\frac{R_1 R_2 C_1}{C_2}} \tag{3.13}$$

Q is the quality factor of the filter which determines the magnitude of the response at the cutoff frequency, and ideally it is set to $\frac{1}{\sqrt{2}}$ so that this magnitude does not go above the bandwidth gain. To simplify the design we want unity gain and set $R_1 = R_2 = 100K\Omega$. With this simplification the relationship of the capacitors to provide the ideal Q can be calculated. In this case the relationship between capacitors is $C_1 = 2 \cdot C_2$ so when C_2 is changed, the value of C_1 will always be changed to be twice as big. Based on published extracellular amplifier designs (Banks *et al.*, 2002; Land *et al.*, 2001; Obeid *et al.*, 2003), the cutoff frequencies implemented on the board were 6 KHz and 10 KHz.
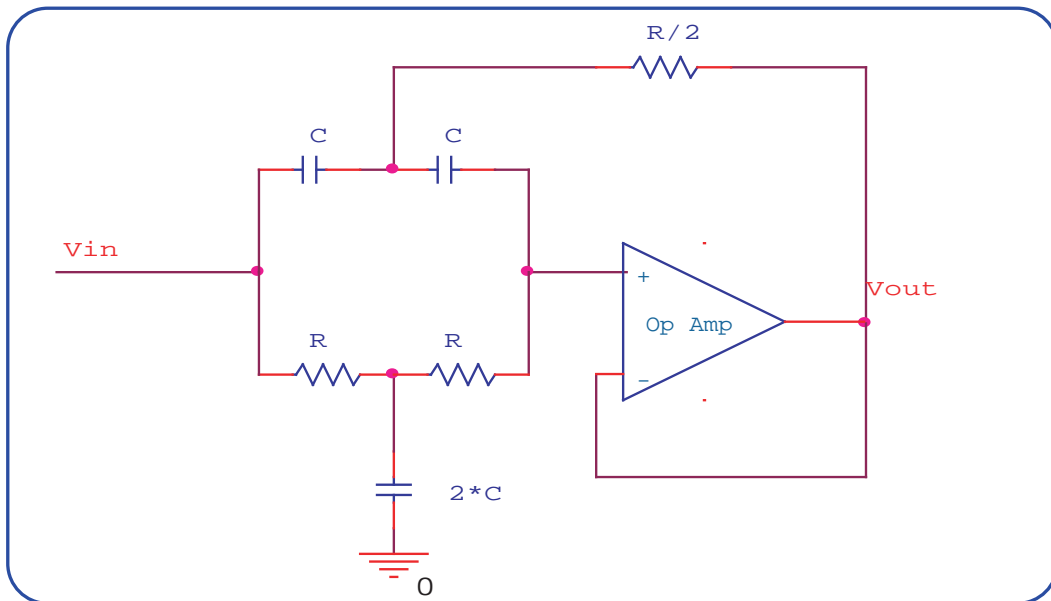
FIGURE 3.5. Extracellular channel fourth stage. The last stage of the extracellular channel is a Twin-T notch filter that attenuates 60 Hz noise (hum) as much as possible. This circuit is formed by a low-pass filter and a high-pass filter in parallel with the same cutoff frequency so that their responses overlap allowing all frequencies to pass except the 60 Hz frequency. The cutoff frequency is selected by choosing appropriate values for R and C based on Equation 3.15.

Notch Filter The last stage adds a notch filter to the design. As seen in Figure 3.5 a Twin-T Notch filter was designed to attenuate 60 Hz signals as much as possible. This circuit only uses one amplifier and thus is simple to design, but the drawback is that it is extremely sensitive to the capacitor and resistor values, and so it is very important to find low tolerance components to assure the precise tuning of the filter to 60 Hz. The principle of this circuit is to combine a low-pass and a high-pass filter in parallel, both first order with the stop bands overlapping (Calvert, 2001), and therefore creating a notch filter that allows all frequencies to pass except for a narrow band, in this case around 60 Hz. The transfer function for this notch filter is:

$$T(s) = \frac{s^2 + \omega_0^2}{s^2 + 2 \cdot \omega_0 \cdot s + \omega_0^2} \tag{3.14}$$

$$\omega_0 = \frac{1}{RC} \tag{3.15}$$

An operational amplifier is then added to this RC filter network to increase the quality factor (Q), to provide a low output resistance, and to allow the use of large resistance values so that small capacitance is required even for a small cutoff frequency. The design process for this stage consists of setting one of the parameters to a starting value $R = 100K\Omega$, and then solving for the other parameter C = 26.5 nF, making sure that the values obtained are standard values and are easily available. In this case, the closest standard value for the capacitor is 27 nF, which results in a theoretical cutoff frequency of 58.9 Hz.

3.1.2   Intracellular Electrometer Channel

Intracellular signals can be much larger than their extracellular counterparts, but that does not mean that the required circuitry is simpler. This type of electrometer requires specialized circuits to compensate for stray capacitance and high electrode resistance and to prevent unintentional current injection as explained in Section 2.2.1. Also, noise must be kept at a minimum by avoiding unnecessary components and by choosing them carefully. Other circuits in the intracellular channel are the same as those used in the extracellular channel. For the purpose of this document the intracellular channel can be divided into four stages as shown in Figure 3.6. The first stage contains three specialized circuits to provide voltage offset compensation, capacitance compensation and current injection; all of those circuits will be explained in this section. The second stage is a low-pass filter explained in Section 3.1.1. Next, a notch filter to avoid 60 Hz noise is included (see Section 3.1.1 for a description). Lastly, a gain stage is included to provide some amplification. Figure 3.6 shows the block diagram with all the main concepts needed for a functional intracellular channel as mentioned above.

Offset Compensation Microelectrodes used in these type of recordings must be extremely sharp in order to penetrate a cell and therefore have very high resistance (see
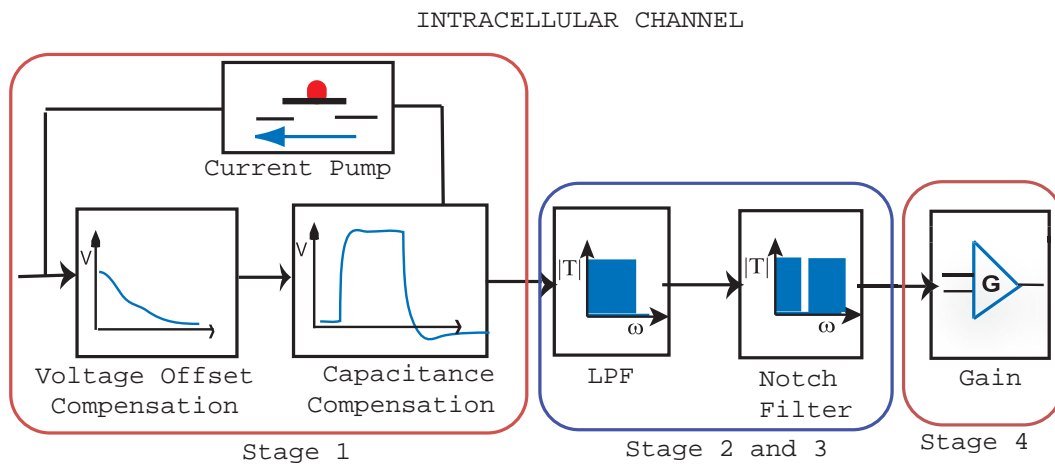
FIGURE 3.6. Intracellular channel block diagram. The first stage is composed of three blocks whose main purpose is to compensate the input signal for distortions introduced by the recording electrode as mentioned in Section 2.2. The first block compensates for the voltage offset that is not part of the signal. The second block compensates for undesired capacitance that reduces the bandwidth of the recording. This compensation must be precise in order to be effective, and that is accomplished by using a current pump which is shown in the third block of this stage. The second and third stage are a low-pass and a notch filter respectively. These filters are the same as those implemented in the extracellular channel. The final stage is a gain stage that amplifies the signal to an acceptable level for further processing.

Section 2.2). This creates a significant voltage drop across the microelectrode with even the smallest current. The offset voltage must be compensated before processing the signal since that voltage is not part of the signal itself. A simple circuit found in Purves, 1981 was implemented for this purpose (see Figure 3.7). The circuit has two precision voltage reference diodes D_1 and D_2 to provide a fixed voltage across their terminals. The diodes are biased by resistors R_3 and R_4 which are connected to the positive and the negative power supply respectively. The value of these resistors will depend on the voltage supply used; ideally, the current pulled from each supply ($I_{v_{cc}}$) should be around $500\mu A$ to provide enough current to the circuit and to the current pump which will be later attached (see below). The equation showing this relation is as follows:

$$R_3 \quad = \quad \frac{V_{cc} - V_{in} + V_D}{I_{v_{cc}}} \tag{3.16}$$

V_D is the diode reference voltage, which is 1.2 V for the part selected (LM385BD-1.2), and V_{in} represents the input signal which includes the voltage offset. The value of this offset is usually in the 100 - 200 mV range including tip potentials (see Section 2.2). For a conservative design we want to be able to compensate up to 300 mV. If we set $V_{in} = 1$ V, and if $V_{cc} = 9$ V, then $R_3 = 18.4K\Omega$. It should be noted that this is a symmetrical circuit, therefore the value of $R_4 = R_3$. The capacitors C_1, C_2, C_3, and C_4 are bypass capacitors and are included in the circuit to improve noise performance. These bypass capacitors have the function of preventing sudden changes in voltages by allowing the AC component to pass through the capacitor to ground. Once we have a fixed voltage across R_{off}, R_1, and R_2, the output is taken from the variable terminal of the potentiometer R_{off} and a voltage divider is formed. The values of these resistors are chosen so that the current going through them (I_1) is well below the $500\mu A$ provided by the supplies as previously designed. The equation is simply:

$$I_1 \quad = \quad \frac{2 \cdot V_D}{R_{off} + R_1 + R_2} \tag{3.17}$$

As mentioned in Section 2.2, the voltage offset present in the input signal is usually less than $\pm 300mV$. If we set $R_{off} + R_1 + R_2 = 40K\Omega$ then 3.17 gives $I_1 = 60\mu A$. In order to obtain $\pm 300mV$ we need a potentiometer with a nominal value of $10K\Omega$ as defined by:

$$R_{off} \quad = \quad 2 \cdot \frac{300mV}{I_1} \tag{3.18}$$

Now the value of R_1 can be easily obtained because of symmetry, $R_2 = R_1 = 15K\Omega$. The voltage offset is then adjusted by moving the wiper terminal up or down, when no offset compensation is needed the wiper terminal must stay in the middle. Finally an op-amp is included to provide high load resistance to the output.
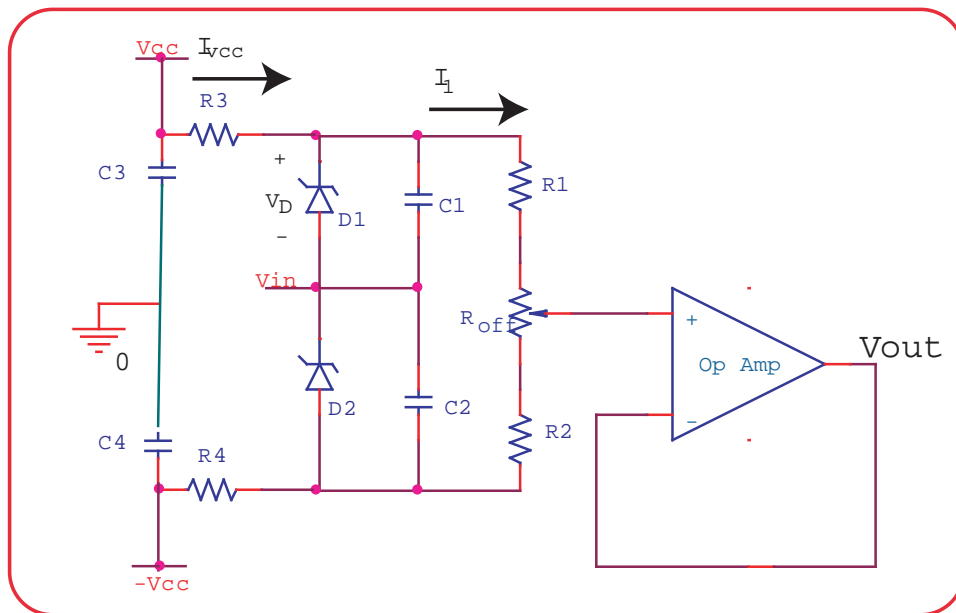
FIGURE 3.7. Intracellular channel offset compensation. This circuit shows how the offset in V_{in} can be compensated by adding an offset of the same magnitude and opposite polarity. Resistors R_3 and R_4 pull currents from the power supplies to keep the diodes D_1 and D_2 active and thus creating a DC reference voltage. A voltage divider is formed by R_1, R_2, and the potentiometer R_{off}, which adjusts the offset. C_1, C_2, C_3, and C_4 are bypass capacitors and are included for noise performance.

Capacitance Compensation Figure 3.8 shows the capacitance compensation circuit and a simple representation of a micropipette commonly used for intracellular recordings. The capacitance labeled C_m represents the stray capacitance mentioned in Chapter 2 and forms a low-pass filter with the resistance R_m. This will degrade some of the input signal at high frequencies preventing the faithful reproduction of fast transients in the signal. The capacitance C_m must be compensated prior to further processing. This is accomplished by adding "negative capacitance" (see Section 2.2.2) so that the effects of the stray capacitance C_m can be practically canceled.
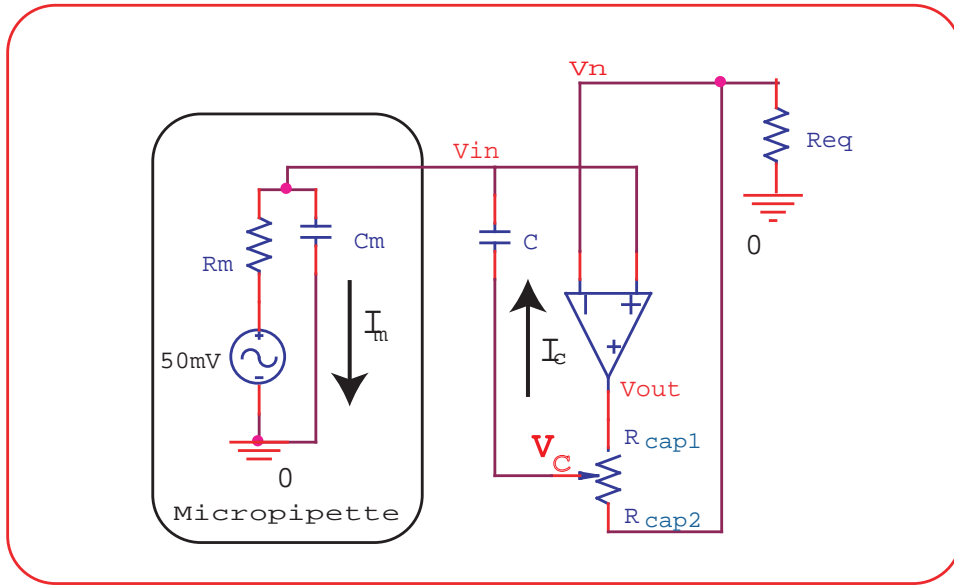
FIGURE 3.8. Intracellular channel capacitance compensation. The recording micropipette is represented by a resistor R_m and a capacitor C_m, which form a low-pass filter. The "true" biological signal is represented by an AC voltage supply. The high frequency current I_m lost through C_m is compensated by the current I_c provided by the specialized circuit composed of an amplifier, a capacitor C and a variable resistor R_{cap}. This variable resistor adjusts the magnitude of I_c by adjusting the gain of the amplifier.

The main idea is to add a current I_c to the input signal in compensation to the current lost through I_m (see Figure 3.8). So in the Laplace transform domain we have:

$$I_m = sC_m \cdot V_{in} \tag{3.19}$$
$$I_c = sC \cdot (V_c - V_{in}) \tag{3.20}$$

The voltage $V_{out} = V_{in} \cdot G$ where G is the gain of the op-amp in this configuration; with maximum compensation $R_{cap1} = 0$ and $R_{cap2} = R_{cap}$ (the maximum value of the

potentiometer), then the voltage across C is:

$$V_c - V_{in} \quad = \quad V_{in} \cdot (G - 1) \tag{3.21}$$

Using Equations 3.19, 3.20, and 3.21, we set $I_c = I_m$ and the effective capacitance (C_{eff}) that is compensated is:

$$C_{eff} \quad = \quad C \cdot (G - 1) \tag{3.22}$$

$$G \quad = \quad 1 + \frac{R_{cap2}}{R_{eq}} \tag{3.23}$$

Where R_{eq} is the load resistance (at the negative input terminal V_n) and is defined by the input resistance of the offset circuit from Section 3.1.2. In Figure 3.7 we can see that the diodes D_1 and D_2 have insignificant resistance when active, and because they are in parallel with the arm containing R_1, R_2, and R_{off}, their resistance is neglected and R_{eq} can easily be calculated by:

$$R_{eq} \quad = \quad \frac{R_3 R_4}{R_3 + R_4} \tag{3.24}$$

$$= \quad \frac{R_3}{2} \tag{3.25}$$

This is the parallel combination of R_3 and R_4, and is calculated to be $9.2K\Omega$. To find the proper value for R_{cap} and C, we must decide on an adequate capacitance compensation. The stray capacitance is only a few pF in the worst cases (Thomas, 1997) and typical compensation ranges from 8 pF to 20 pF (The Axon Guide, 1993). Using Equation 3.22 with $C = 3pF$ and designing the circuit to provide a maximum negative capacitance of 20 pF we find that we need a gain G of 6. Finally using Equation 3.23, the value of R_{cap} is calculated and found to be $61.3K\Omega$. This is the minimum required value to provide compensation for at least 20pF of capacitance, any greater value will provide more capacitance. The compensation provided by this circuit is adjusted to the necessary value by moving the wiper terminal of R_{cap} up and down.

Current Pump The current pump provides an easy way to measure the micropipette resistance by injecting a known current into the micropipette and observing the change in voltage at the input node. The micropipette resistance R_m is just the change in voltage observed divided by the current injected (Ohm's law). Another use of the pump is to adjust the capacitance compensation. Constant current is injected for a small period of time and the voltage is observed during the same time; the shape of the voltage waveform indicates when the correct compensation is achieved (this method is fully explained in Section 2.2.2). Figure 3.9 shows the entire first stage of an intracellular channel; it consists of circuits from Sections 3.1.2 and 3.1.2
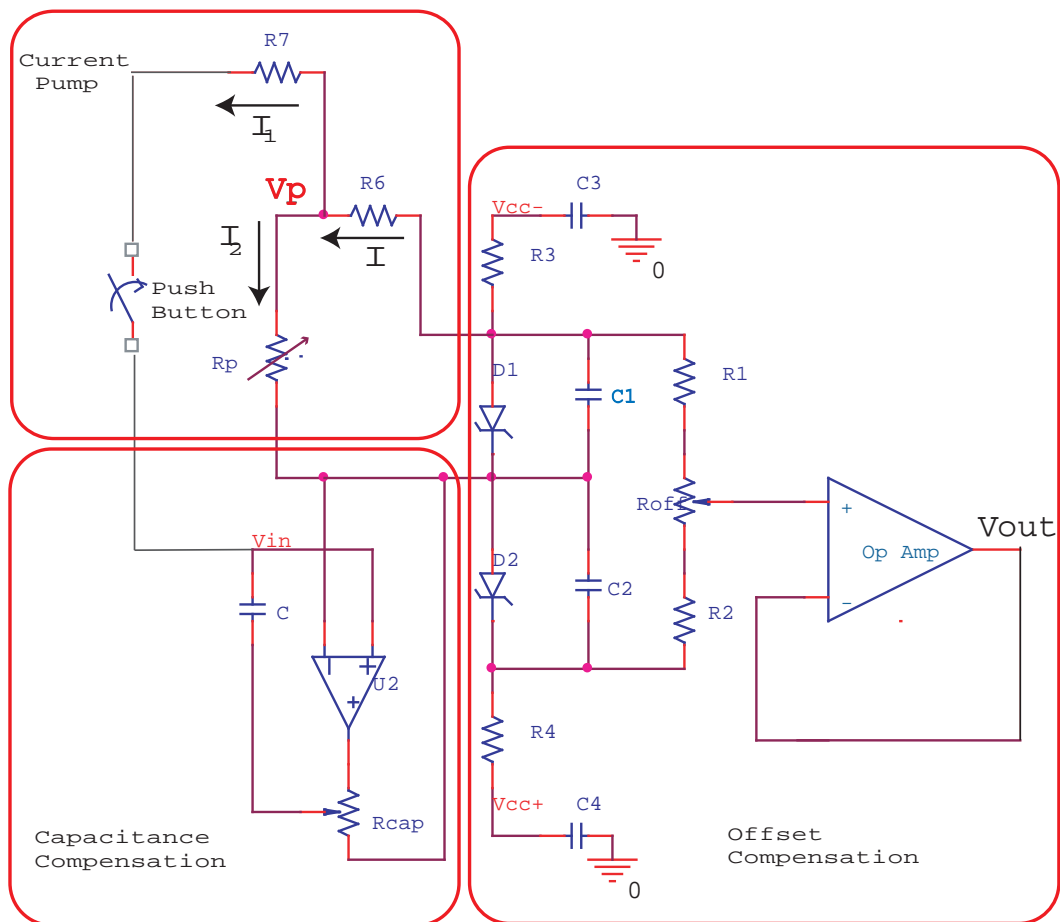
FIGURE 3.9. Intracellular channel first stage. This stage contains the offset and capacitance compensation circuits. A current pump is also included. This pump is used to inject current pulses to the microelectrode for two main purposes. The first is to calculate microelectrode resistance, and the second is to verify correct capacitance compensation. The current I_1 is injected when the line is connected by the push button, and the amount of current is determined by the variable resistor R_p.

joined together plus the current pump. The current pump takes advantage of the fixed voltage provided by diode D_1 and forms a current divider with resistors R_6, R_7, and the variable resistor R_p.

The following equations show the relationship between resistors and current to be injected:

$$I_1 = \frac{V_p - V_{in}}{R_7} \tag{3.26}$$

$$I_2 = \frac{V_p - V_{in}}{R_p} \tag{3.27}$$

$$I = \frac{V_{in} - 1.2V - V_p}{R_6} \tag{3.28}$$

$$= I_1 + I_2 \tag{3.29}$$

From Equations 3.26 through 3.29 we can get:

$$I = -\frac{1.2V}{R_6 + \frac{1}{\frac{1}{R_7} + \frac{1}{R_p}}} \tag{3.30}$$

The current pump is not required to provide more than a few nA of current (see Purves, 1981). Another constraint is that potentiometers are more easily available in small resistances, therefore the resistors R_6 and R_7 should be very high (MΩ). Taking this into account we can choose $R_6 = 1.5M\Omega$ which will be in charge of pulling current from the supply, $R_p = 50K\Omega$ and $R_7 = 10M\Omega$. R_p is used to determine the amount of current that goes through R_7 when the push button is pressed. The maximum current will be provided when R_p is at its maximum value; using Equation 3.30, $I = 0.774\mu A$ and using Equation 3.26 $I_1 = I \cdot \frac{R_7}{R_7 + R_p} = 3.84nA$.

Low-Pass and Notch Filters These stages use exactly the same circuits used in the extracellular channel shown in Figures 3.4 and 3.5. The low-pass filter is implemented with the optional cutoff frequency of 6 KHz or 10 KHz. The frequencies selected were the same as those selected in the extracellular case because both types of signals have similar frequency characteristics. The intracellular channel is as vulnerable to electrical noise (hum) as the extracellular channel; for that reason the same notch filter is implemented to significantly reduce 60 Hz noise. Refer to Section 3.1.1 for more information on these circuits.

Gain Stage Finally, the last stage of this channel consists of an amplification stage. Even though intracellular signals are much bigger in amplitude than extracellular signals, there is some gain required to amplify the signal to an optimal size for further processing (this signal usually goes to an ADC). The gain is accomplished by a non-inverting amplifier as seen in Figure 3.10 where the gain is governed by:

$$G = 1 + \frac{R_2}{R_1} \tag{3.31}$$

Intracellular amplifiers usually offer optional amplification of 1x to 100x (Purves, 1981). Two amplifications settings were chosen for this board: 10x and 100x. By setting $R_1 = 100K\Omega$ we can solve for R_2 using Equation 3.31 and we obtain : $R_2 = 900K\Omega, 9.9M\Omega$. The gain can be set by selecting the resistor indicated through a switch.
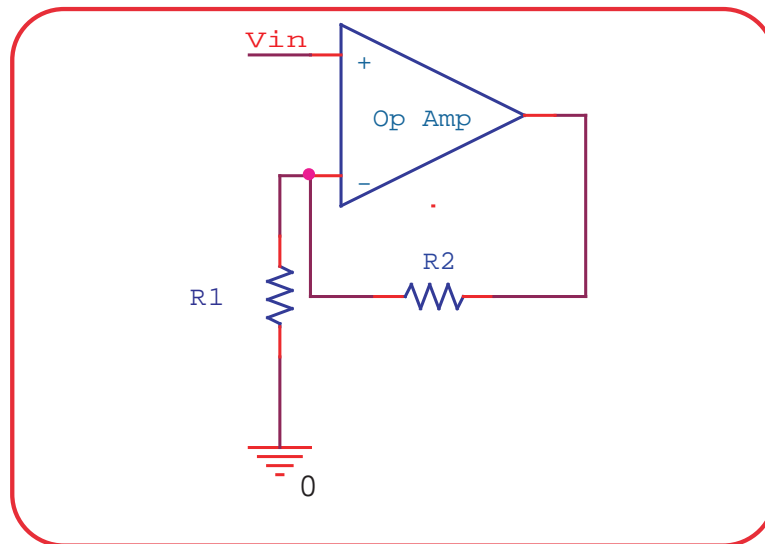

FIGURE 3.10. Intracellular channel fourth stage. This is a non-inverting amplification stage with a gain of usually 10x to 100x. The gain is determined by Equation 3.31.

3.1.3 Spike Detection and Spike Rate Circuitry

The electrometer will be used to obtain different types of electrophysiological data which will include mostly spikes. Spikes have a distinctive waveform and that can be used to detect them in a simple and effective manner. The design of spike detection and spike rate computation circuitry was necessary to process the recorded data sufficiently fast so that meaningful information could be extracted and closed-loop experiments involving robotics could be successfully performed. Most of the data processing required in the experiments conducted could be done in software, but the speed is constrained by the microprocessor used for this task. Additionally, the biological data would need to be sampled at high frequencies in order to avoid losing spikes. Therefore, it is desired to reduce the computation time in the microprocessor by conducting some processing in hardware. Since speed was a big concern, choosing to implement an analog circuit versus a digital design was an obvious choice.

Figure 3.11 shows the main components of the circuitry which can be conceptually divided into three stages: spike enhancement, spike detection, and spike rate compu-

tation. The first two stages were designed based on a circuit diagram from Rogers and Harris, 2004.
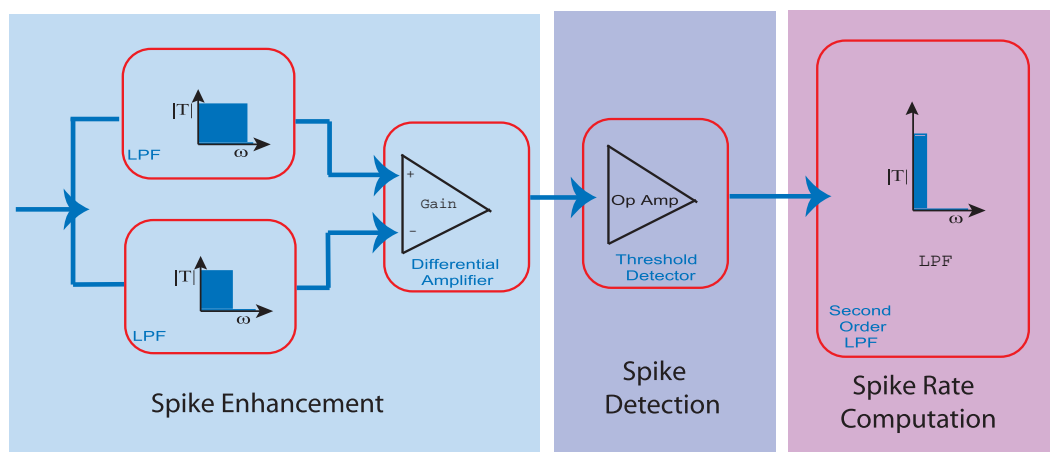

FIGURE 3.11. Block diagram of spike detection and spike rate computation circuitry. The first block enhances the spike by attenuating high frequency components and subtracting low frequencies including DC drift. This stage also has a gain that enhances the "significant" part of the spike. The second stage consists of an amplifier that saturates the output to the positive rail when the input signal goes above a preset threshold. The output saturates to the negative rail when the input signal stays below the threshold. The last block computes the average of the output signal of the previous stage. This average is obtained by applying a second order low-pass filter with a very small cutoff frequency which then indicates the spike rate with the assumption that spikes have constant widths.

Enhancing the Spike Enhancing the spike involves reducing the noise to prevent false detections. The main idea is to tune the circuit to a particular frequency where we are expecting most of our spikes to be, and to amplify those signals; thus increasing the Signal to Noise Ratio (SNR). The idea of enhancing the spike increases the complexity of the required circuitry but the result is a more reliable spike detector.

First, the signal goes concurrently through two low-pass filters that are designed with different cutoff frequencies. The filter with the higher cutoff frequency removes high frequency noise and the other has a low cutoff frequency to create a local average. Next, the difference of the output of those filters is computed by a differential amplifier. This results in a signal that does not have DC offsets (they get subtracted) and is not affected by changes in noise level, making it a robust method and suitable for long term neural recordings (Rogers and Harris, 2004). This stage can also have non-unity amplification if required.

The optimal cutoff frequencies for error-free detection depend on different factors such as the type of electrophysiological data to be recorded and the environment

noise present during the recording, which means the filters must be tuned every time accordingly. This implies that tuning must be as easy and accessible as possible and that is the reason why Operational Transconductance Amplifiers (OTAs) where chosen for this circuit. OTAs implementing current controlled filters are best suited for this task. A current controlled filter can be tuned for a particular cutoff frequency without the need of changing capacitors just by providing an appropriate current. Moreover, the current can be indirectly supplied by using a variable resistor R_{var} as seen in Figure 3.12. The variable resistor will determine the amplifier bias current I_{ABC}, which in turn will determine the transconductance of the amplifier g_m. This relation will change in accordance to the thermal voltage V_T; the relation at room temperature ($V_T \approx 25.8mV$) is:

$$g_m \quad = \quad \frac{I_{ABC}}{2 \cdot V_T} \tag{3.32}$$

$$g_m \quad = \quad 19.2 \cdot I_{ABC} \tag{3.33}$$

The transconductance of the amplifier (g_m) determines the voltage-to-current gain of the amplifier, therefore it also determines the cutoff frequency as follows:

$$w_0 \quad = \quad \frac{R_4 \cdot g_m}{(R_3 + R_4) \cdot C} \tag{3.34}$$

In order to find the correct values for all components involved, we need to know the approximate range of cutoff frequencies that will be used in this application. The experiment presented in Rogers and Harris, 2004 shows the desired cutoff frequencies to be 1.4 KHz and 5.3 KHz after some simulations in Matlab were performed. In those simulations neural recordings were used with added white noise, then the detection was tested for different cutoff frequencies and in the optimal case 90 percent of spikes were correctly detected. As mentioned before, the optimal cutoff frequencies will depend on several factors but having values that worked for some neural recordings is a good starting point. With resistors $R_1 = R_3 = 100K\Omega$ and $R_2 = R_4 = 200\Omega$ for both filters, the capacitors were chosen to be $C_1 = 150pF$ and $C_2 = 470pF$. In order to obtain similar cutoff frequencies as those previously mentioned, g_m should be around 2.3m℧. From Equation 3.34 we obtain $f_0 = 1.55KHz$ for one filter and $f_0 = 4.8KHz$ for the other filter. The current I_{ABC} needed is 119.8μA by Equation 3.32. These calculations assume that both filters will be using the same I_{ABC} but this does not need to be the case. Each filter is given a separate variable resistor to be able to fine tune them individually.

The value of the variable resistor R_{var} and the voltage across its terminals will determine the amount of current I_{ABC}. On one side of the resistor, V_{abc} will be internally determined by the OTA as two diode drops (approx. 1.2 V, National Semiconductors LM13700 datasheet, 1999) above the negative power supply $-V_{cc}$. On the other side, R_{var} is connected to ground. In order to have a current of 119.8μA
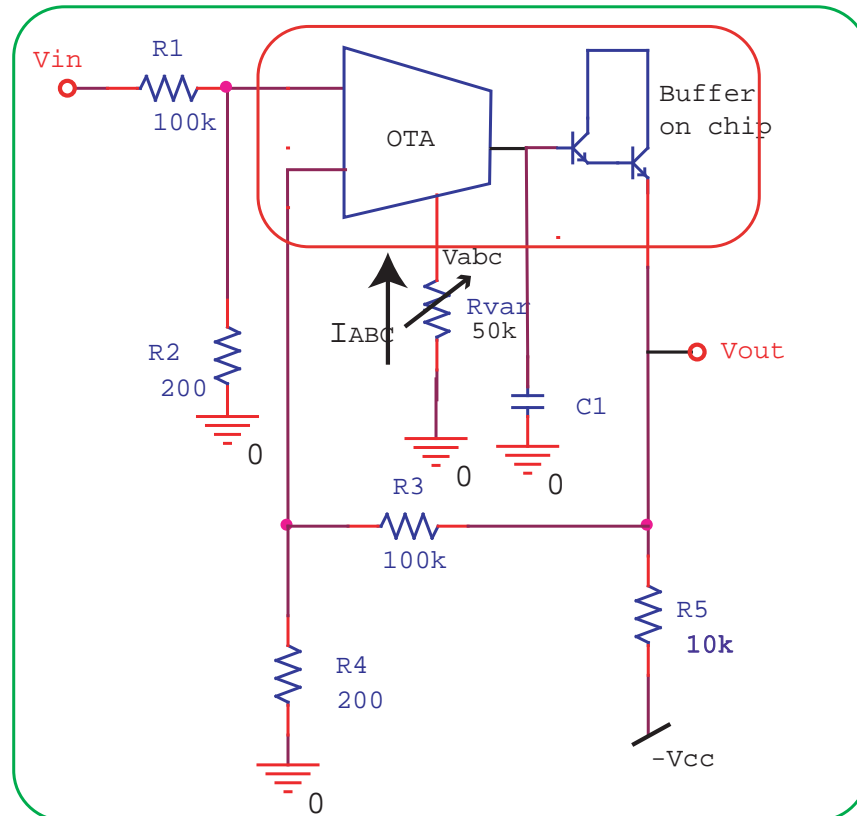
FIGURE 3.12. Spike filtering. The spike is filtered by two low-pass filters with different cutoff frequencies; this figure only shows one of them. Operational Transconductance Amplifiers (OTAs) are used to make the filters easily tunable. The configuration shown here uses a variable resistor (R_{var}) to control the cutoff frequency. The cutoff frequency increases as the current I_{ABC} increases without the need to change the rest of the components. In normal operation, the node V_{abc} sits at a negative voltage 1.2 V higher than the negative supply rail, which will make I_{abc} go in the direction shown. The value of C_1 is selected based on the approximate cutoff frequency that it is needed based on Equation 3.34. This figure is a modified version of a circuit from National Semiconductors LM13700 datasheet, 1999.

as previously calculated, R_{var} must be $75.062K\Omega$ when $-V_{cc} = -9V$. The final values used for one of the filters can be seen in Figure 3.12. The new generation of OTAs include an output buffer composed of two transistors whose job is to decrease the output resistance so that OTAs can be used as Op-Amps and drive resistive loads.

After the input signal has been filtered simultaneously by two low-pass filters, the difference is computed by the differential amplifier in Figure 3.13. This is just a regular differential amplifier formed by an operational amplifier where the output is determined by:

$$V_{out} = V_{in1} \cdot \frac{(R_1 + R_2)R_4}{(R_3 + R_4)R_1} - V_{in2} \cdot \frac{R_2}{R_1} \qquad (3.35)$$

This equation can be reduced when $R_1 = R_3$ and $R_2 = R_4$ to the following transfer function:

$$T(s) = \frac{R_2}{R_1} = \frac{V_{out}}{V_{in1} - V_{in2}} \qquad (3.36)$$

The gain of this stage should be chosen so that the spikes will not hit the rails and thus saturate the amplifier output voltage. Even though saturation will occur in the next stage, it is prevented at this stage because it might be useful to observe the undistorted signal at this point. For this circuit a gain of 40 gives a favorable result.
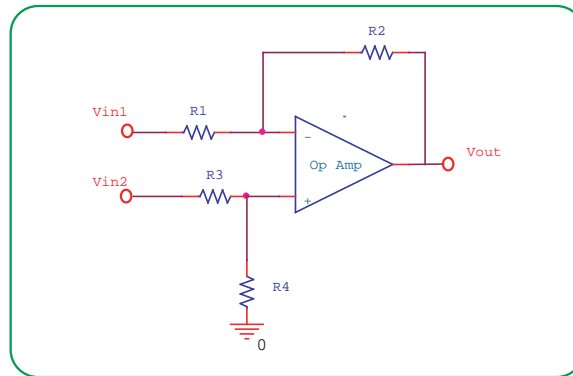
FIGURE 3.13. Differential stage in spike enhancement. This circuit is a differential amplifier with non-unity gain whose purpose is to subtract lower frequencies from the spikes. The idea is to amplify only an optimized bandwidth that enhances the distinctive features of the spike. The gain is determined by Equation 3.36.

Spike Detection This stage is fairly simple; it consists of a non-inverting Schmitt Trigger detector composed of an operational amplifier and three resistors as shown in Figure 3.14. The idea is that a variable resistor R_{det} will adjust the reference voltage

V_{ref}, which is a fixed voltage input to the negative terminal. The circuit does not work as an amplifier; instead, it saturates to the positive rail when the input on the negative terminal is higher than V_{ref}, and to the negative rail when the opposite is true. Additionally, this circuit implements a hysteresis which allows you to set two switching levels that deviate from the preset reference voltage, one for high-to-low transitions (V_{HL}) and one for low-to-high transitions (V_{LH}). The switching levels are obtained according to the following equations:

$$V_{HL} = V_{ref} \cdot (1 + \frac{R_1}{R_2}) - V_{cc} \cdot \frac{R_1}{R_2} \tag{3.37}$$

$$V_{LH} = V_{ref} \cdot (1 + \frac{R_1}{R_2}) + V_{cc} \cdot \frac{R_1}{R_2} \tag{3.38}$$

The hysteresis is defined as the gap between the two switching levels, using Equations 3.37 and 3.38 can be calculated as $2 \cdot V_{cc} \cdot \frac{R_1}{R_2}$. The ratio of resistor R_1 to R_2 adjusts the hysteresis of the circuit. When $R_1 << R_2$ the switching levels are the same and there is no hysteresis. On the other hand when $R_1 = R_2$, the switching values are $-V_{cc}$ and V_{cc}. The desired hysteresis is in the middle of those two scenarios. The value of the potentiometer R_{det} is not of importance as long as the current going through it falls within maximum ratings of the device. If $V_{cc} = 5V$, $R_1 = 15K\Omega$, $R_2 = 930K\Omega$, and the reference voltage is 2.5 V, then the high-to-low switching level is 2.46 V and the low-to-high switching level is 2.63 V. The output of this stage is just a binary signal
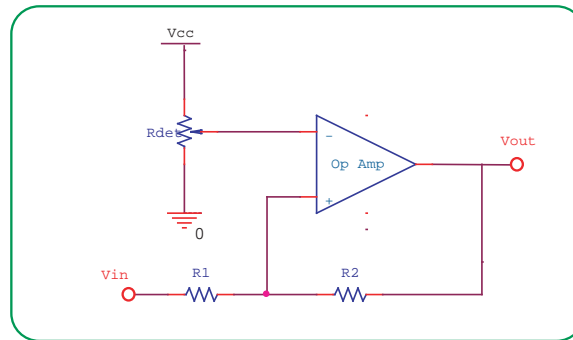
FIGURE 3.14. Spike detection circuit. A non-inverting Schmitt Trigger circuit is used to detect the spike. The threshold is adjusted with the variable resistor R_{det}. Two switching levels are created by the ratio of resistor R_1 over R_2, one for low-to-high and other for high-to-low transitions.

and in principle can go directly to the digital input of a microprocessor.

Spike Rate Computation This stage takes the digital signal from the previous stage and calculates the spike rate by computing an average of the positive pulses in the

signal. The task is accomplished by a two-pole (second order) low-pass filter with a very small cutoff frequency (see Figure 3.15). The idea of using a two pole filter instead of a single pole is to have a response closer to that of an ideal filter so that the local average computation is more closely realized. The filter was made out of two single-pole filters similar to those from Section 3.1.3 connected in a cascaded manner. The same resistor values were used and the only change made was in the value of the capacitors. The relationship between the capacitors in order to maintain the same resistor values is:

$$C_2 \quad = 2 \cdot C_1 \tag{3.39}$$

The cutoff frequency can be calculated from Equation 3.34 by setting $C = C_1$. For instance, if we want a cutoff frequency of 25 Hz and the transconductance is approximately $g_m = 2.4m\mho$, then we can solve for the capacitors to get $C_1 = 30nF$ and $C_2 = 60nF$. When the cutoff frequency is very small the output signal will be nearly a DC value that will be changing only when the spike rate increases or decreases.
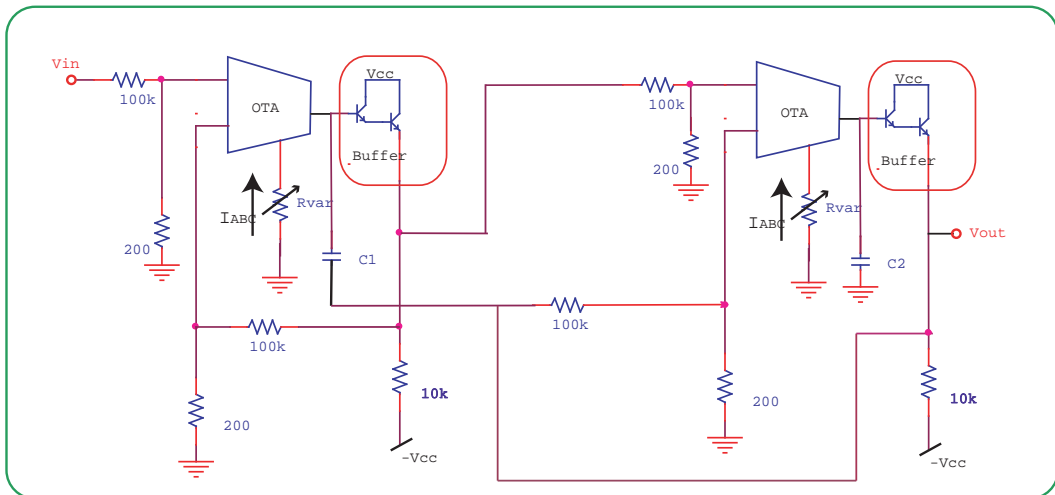
FIGURE 3.15. Spike rate computation using a two-pole LPF. This LPF is formed by cascading two LPFs from Figure 3.12. A very small cutoff frequency is chosen so that the output of this stage is nearly a DC value based on Equation 3.34.

3.2 PSpice Simulations

Once the circuits were chosen for the design, the analog circuit simulation program PSpice from Cadence Design Systems was extensively used as a tool to verify and fine-tune the design. In this section, the entire circuit design is tested and plots of the

results are included. These plots show the output signal once it has been processed by the channel as well as the signal at different stages of the circuit.

3.2.1 Extracellular Channel

Figure 3.16 shows the entire extracellular channel including all component values used in the simulations. An AC analysis was performed using a sinusoidal input of 1 mV amplitude by sweeping the frequency from 1 Hz to 100 KHz. The frequency response is shown in Figure 3.17. In Figure 3.17a the settings for 20 Hz HPF and 10 KHz LPF are simulated. In Figure 3.17b, the circuit shows a bandwidth of 300 Hz to 6 KHz, which are the other available settings. Figure 3.18 shows a test of the different selectable gains. In conclusion, the extracellular channel works as designed based on the simulation results shown in the figures presented.

3.2.2 Intracellular Channel

Figure 3.19 shows the entire intracellular channel as simulated in PSpice. The low-pass and notch filters are identical to those in the extracellular channel, therefore the frequency response for those filters is not repeated. In order to test the capacitance compensation two simulations were performed. The first one involves the use of a current pulse simulating the current pump. This pulse injected 3.84 nA to the micropipette simulated by a capacitor and a resistor in parallel (see Figure 3.19). Then the voltage at the input node was observed for different compensations. A pulse current was applied into the simulated micropipette and Figure 3.20 shows the voltage at the input node. These results include three cases: undercompensation, full compensation, and overcompensation. The second simulation conducted was a frequency response of the circuit for different compensations. As shown in Figure 3.21, this also shows the three different cases of compensation. The offset compensation circuit was verified simply by observing the DC offset at the output while trying different positions of the potentiometer R_6, and the results are shown in Figure 3.22. Finally the different gains available in this channel are shown in Figure 3.23. All simulations illustrate the intracellular channel works as designed.

3.2.3 Spike Detection and Spike Rate

Figure 3.24 shows the entire spike detection and spike rate calculation circuit as simulated in PSpice. This circuit is composed of three filters which can be fine tuned for each application. These simulations assumed the optimal cutoff frequencies for the first stage filters were 1.4 KHz and 5.3 KHz. Results for the frequency response of the first stage is shown in Figure 3.25. The second stage of this circuit involves detection of a spike and a transient response simulation was performed. For this simulation a sinusoid was used as input and the reference voltage was selected for 2.5 V which theoretically creates switching levels of 2.46 and 2.63. Figure 3.26 shows the
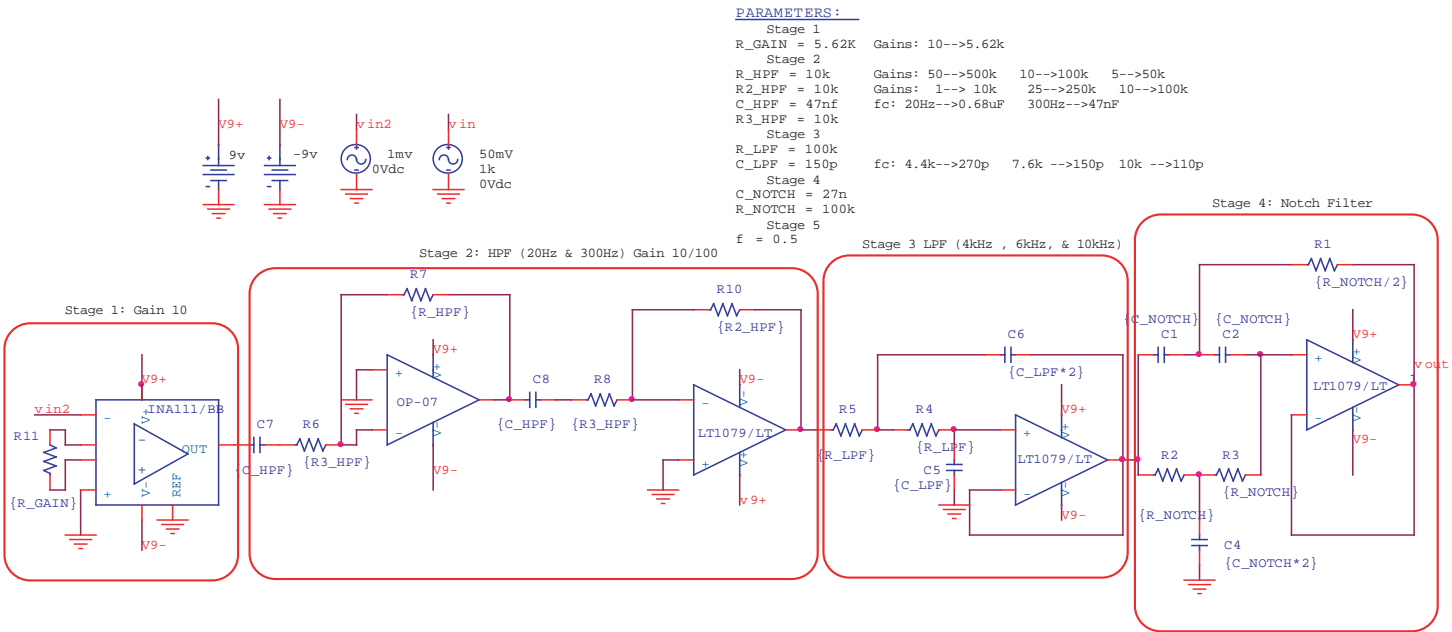
FIGURE 3.16. Extracellular channel circuit. This schematic shows the entire extracellular channel as it was simulated in PSpice.

PARAMETERS:
    Stage 1
R_GAIN = 5.62K   Gains: 10-->5.62k
    Stage 2
R_HPF = 10k   Gains: 50-->500k   10-->100k   5-->50k
R2_HPF = 10k   Gains: 1--> 10k   25-->250k   10-->100k
C_HPF = 47nf   fc: 20Hz-->0.68uF   300Hz-->47nF
R3_HPF = 10k
    Stage 3
R_LPF = 100k
C_LPF = 150p   fc: 4.4k-->270p   7.6k -->150p 10k -->110p
    Stage 4
C_NOTCH = 27n
R_NOTCH = 100k
    Stage 5
f = 0.5

V9+   9v
V9-   -9v
vin2 1mv 0Vdc
vin   50mV 1k 0Vdc

Stage 1: Gain 10
vin2
R11
{R_GAIN}
INA111/BB
+
OUT
REF
V9+
V9-

Stage 2: HPF (20Hz & 300Hz) Gain 10/100
R7
{R_HPF}
OP-07
V9+
V9-
C7
C_HPF}
R6
{R3_HPF}
C8
{C_HPF}
R8
{R3_HPF}
R10
{R2_HPF}
LT1079/LT
V9-
V9+

Stage 3 LPF (4kHz , 6kHz, & 10kHz)
R5
{R_LPF}
R4
{R_LPF}
C6
{C_LPF*2}
C5
{C_LPF}
LT1079/LT
V9+
V9-

Stage 4: Notch Filter
R1
{R_NOTCH/2}
{C_NOTCH}
C1
{C_NOTCH}
C2
R2
{R_NOTCH}
R3
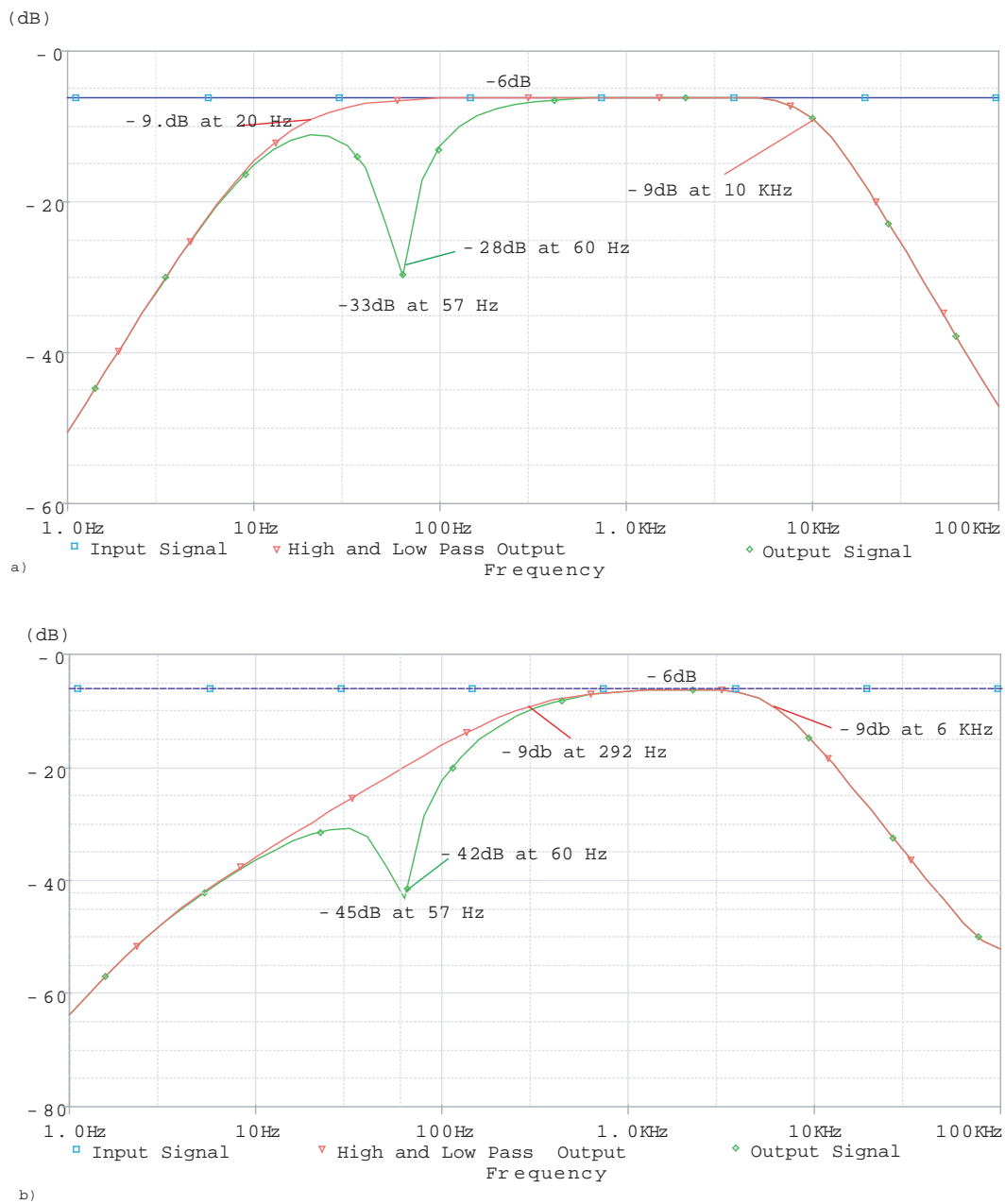{R_NOTCH}
C4
{C_NOTCH*2}
LT1079/LT
V9+
V9-
vout

FIGURE 3.17. Extracellular channel frequency response. The circuit in Figure 3.16 was simulated with an AC voltage input of 1 mV amplitude. These plots show the frequency response over the range 1-100K Hz frequency. a) This plot shows the response when the settings were 20 Hz HPF and 10 KHz LPF. One trace shows the signal before the notch and the other trace after the notch to show that the HPF cutoff frequency changes. b) This plot shows the filtered signal when the settings are 300 Hz HPF and 6 KHz LPF. Traces showing the signal before and after the notch are also included.
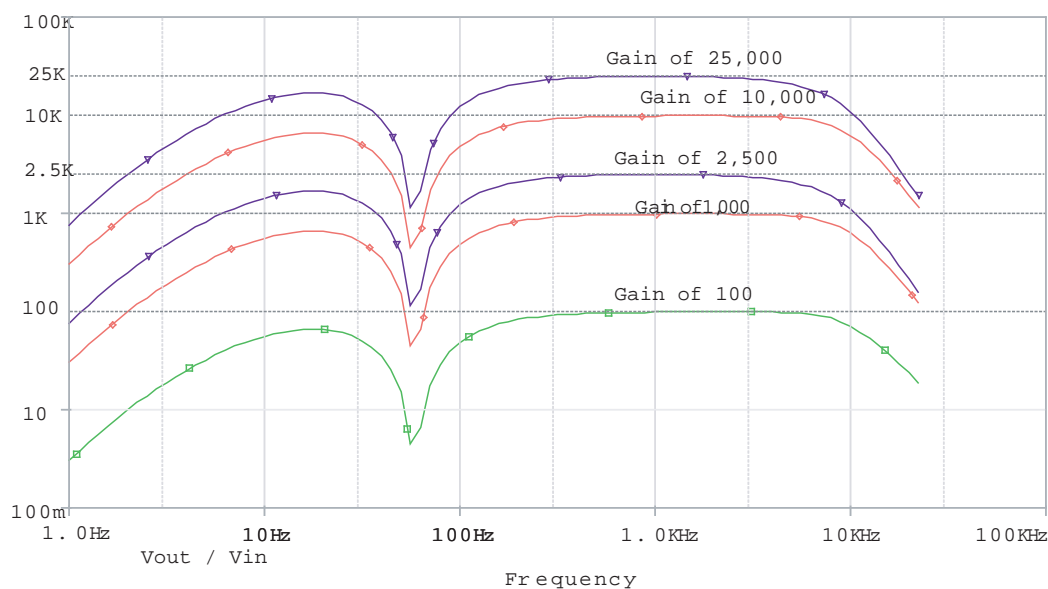
FIGURE 3.18. Extracellular channel gain. The circuit in Figure 3.16 was simulated to show all five available gains. A sinusoid input of 1 mV amplitude was used in this simulation, and the gain of the output was plotted over the 1-10K Hz frequency range.

plot obtained; the waveforms seem to cross at about 1.9 V (high-to-low), and 3.9 V (low-to-high). These are different from the switching levels because of the op-amp slew rate. The output of the spike detector starts changing from low to high at the correct switching level but the change is not immediate; when the waveforms actually cross, the spike waveform is at a higher voltage. In the last stage, a two-pole LPF is used to compute the average of the spike signal and thus calculate the rate. Figure 3.27a shows how the rate increases as the input signal increases its frequency just like neural data would spike faster when more active, and Figure 3.27b shows a plot of the input frequency against the average value at the output of this stage. Overall the simulations show this design works as expected.

3.3   Digital Design

As mentioned in the introduction in Chapter 1, the electrophysiology board needs to be suitable for closed-loop experiments involving mobile robotics. Besides the size constraint, performing closed-loop experiments in mobile robots implies that the data must be processed on board, and the system must have wireless programmability. For this reason a data acquisition system was designed and incorporated to the recording channels in a second prototype. Wireless programmability was achieved by incorporating digital components and a Bluetooth device as explained in this section.
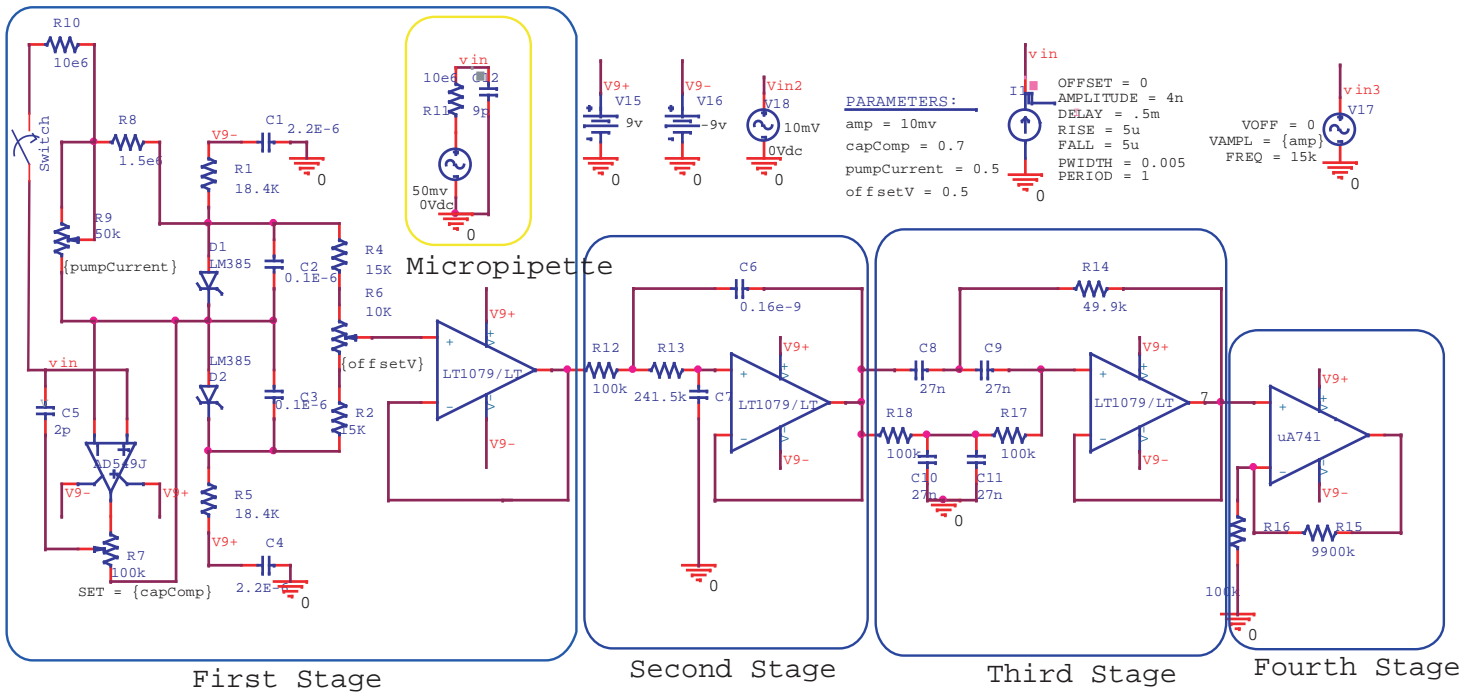
FIGURE 3.19. Intracellular channel circuit. This schematic shows the entire intracellular channel as it was simulated in PSpice.
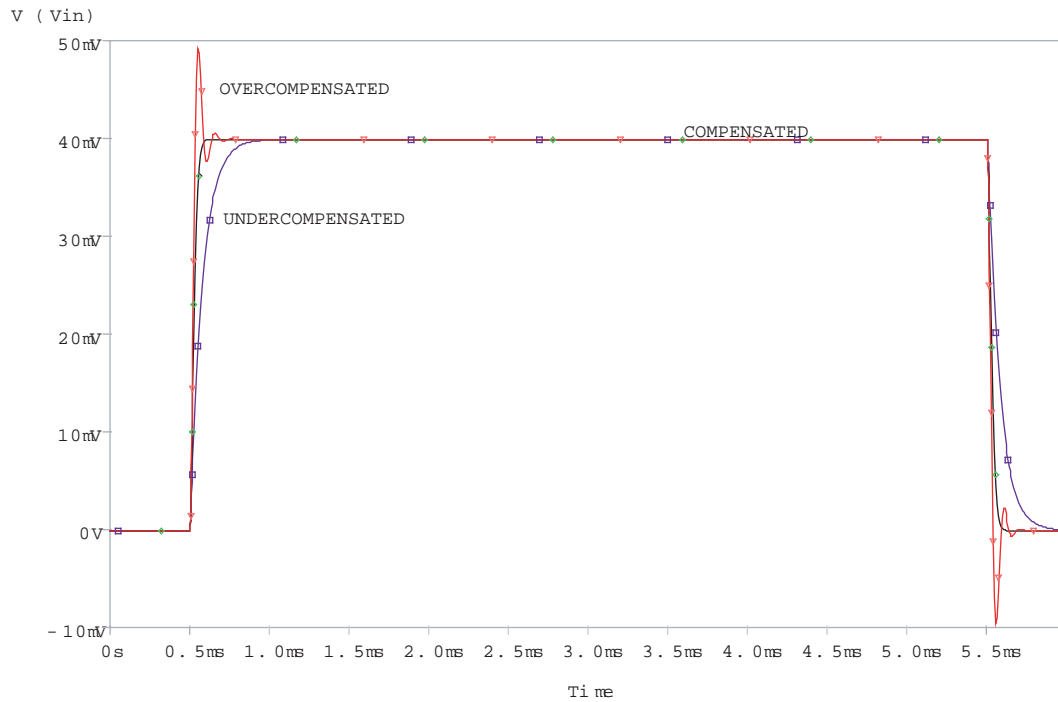
FIGURE 3.20. PSpice simulation of capacitance compensation transient response. The circuit in Figure 3.19 was simulated by applying a current pulse of 5 ms to the simulated micropipette. The voltage at the input was observed during the same period of time. This procedure was repeated for three different potentiometer values (R_7 in Figure 3.19). The result shows three traces where undercompensation, full compensation, and overcompensation are present as explained in Section 2.2.2. In the first case, undercompensation can be detected by the slower rate in which the signal increases and decreases, showing capacitance. The second case shows proper compensation since the signal is almost a perfect pulse. In the last case, ringing and oscillation indicate overcompensation.
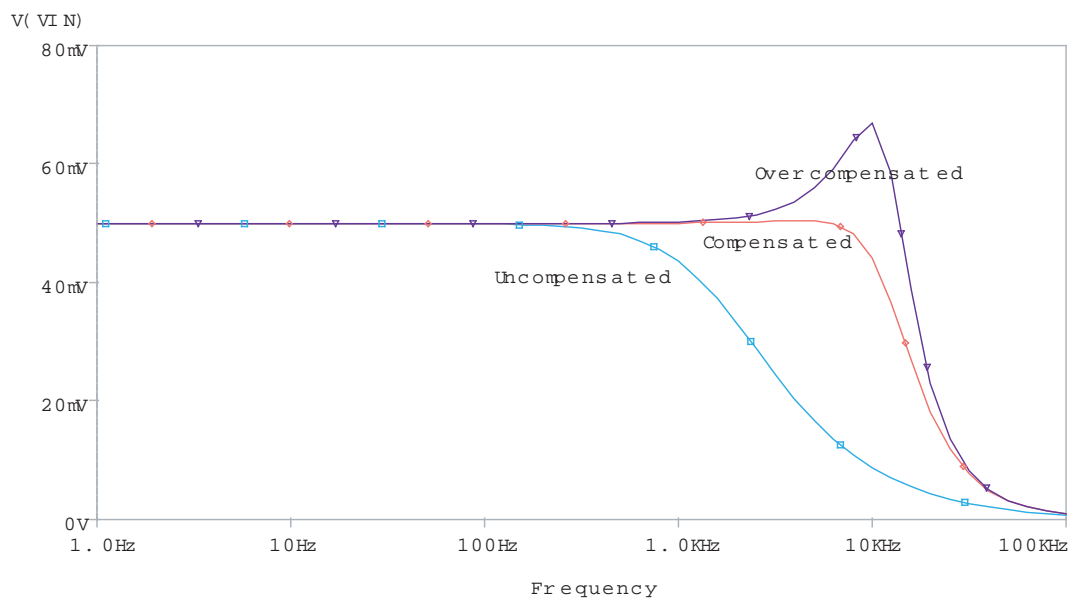
FIGURE 3.21. PSpice simulation of capacitance compensation frequency response. In this simulation an input signal of 50 mV amplitude was used and the frequency response was plotted. Three different cases are shown for three different potentiometer values (R_7 in Figure 3.19). The traces show undercompensation, full compensation, and overcompensation.
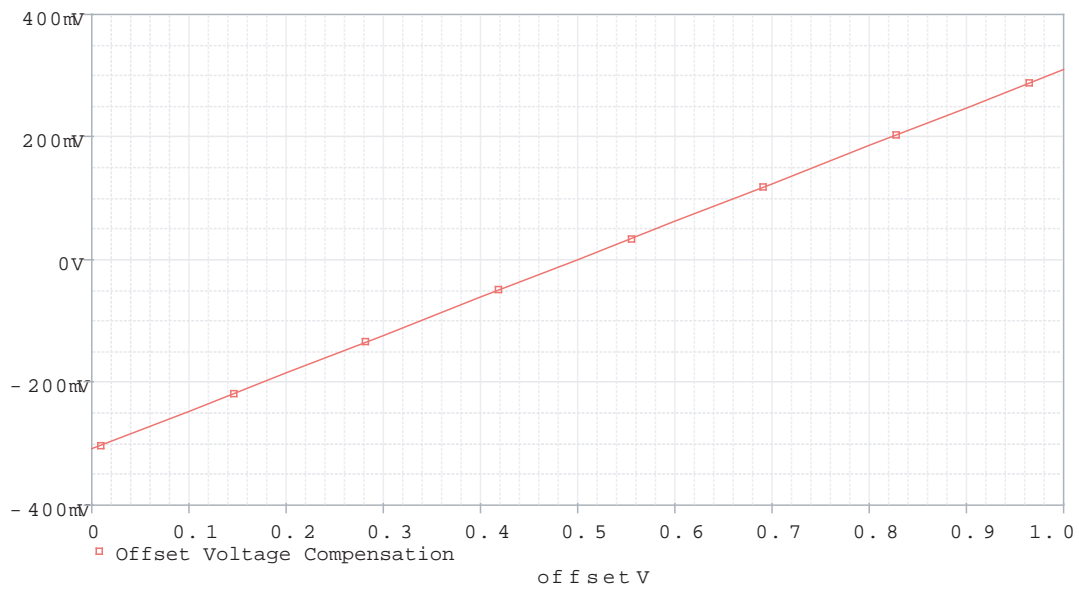
FIGURE 3.22. PSpice simulation of offset compensation. The output DC voltage was plotted while the value of "offsetV", the set parameter of the potentiometer R_6, was changed from 0 to 1. The offset changes linearly from -300 mV to 300 mV.
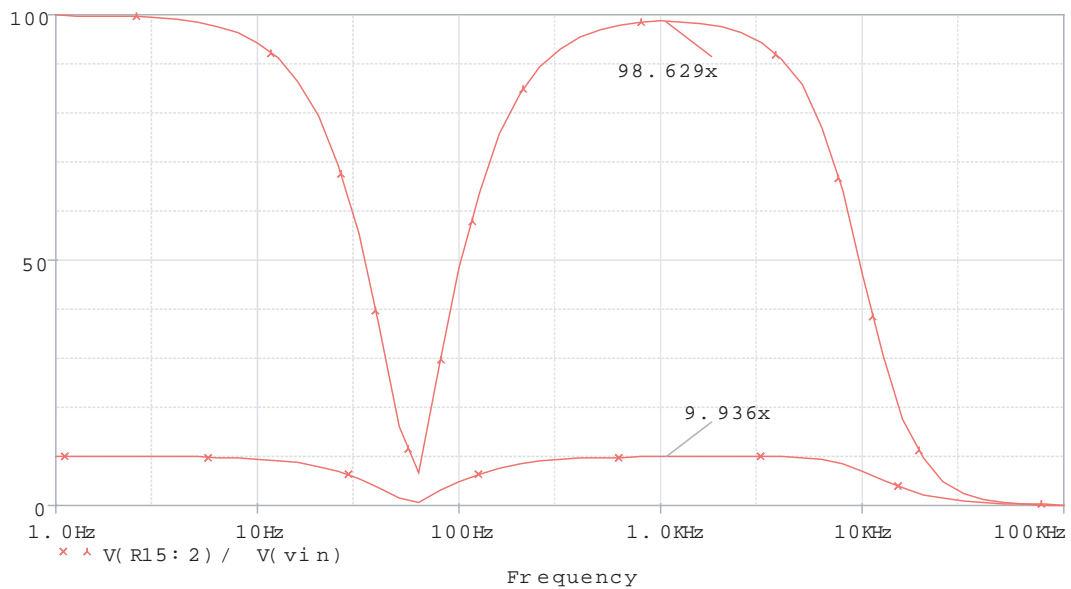

FIGURE 3.23. PSpice simulation of intracellular gain. This plot shows the two available gains (10x and 100x) in the intracellular channel over the range of 1-10K Hz frequency range.
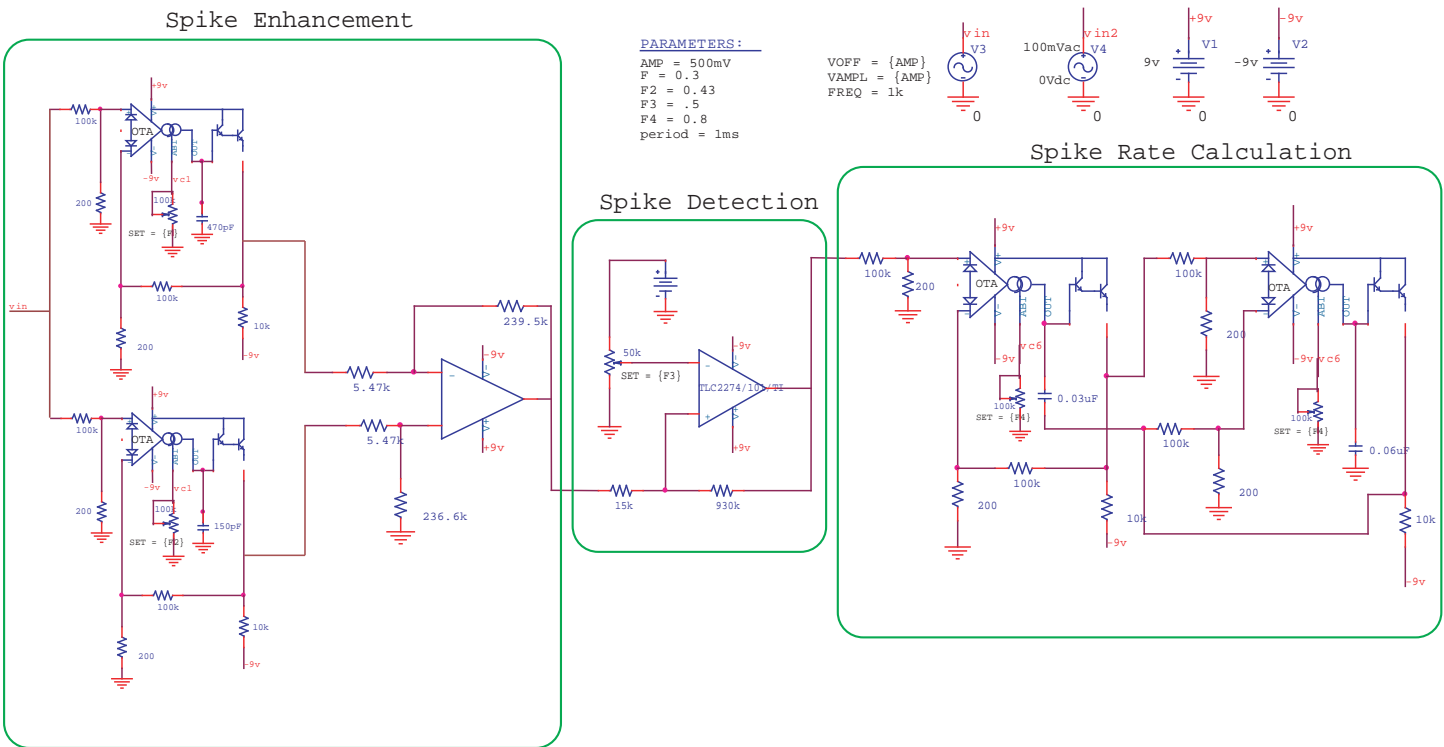
FIGURE 3.24. Spike detection and spike rate calculation. This schematic shows the entire spike detection and rate calculation circuit as it was simulated in PSpice.

(dB)

25.7 dB at 1.4 KHz   25.7 dB at 5.3 KHz
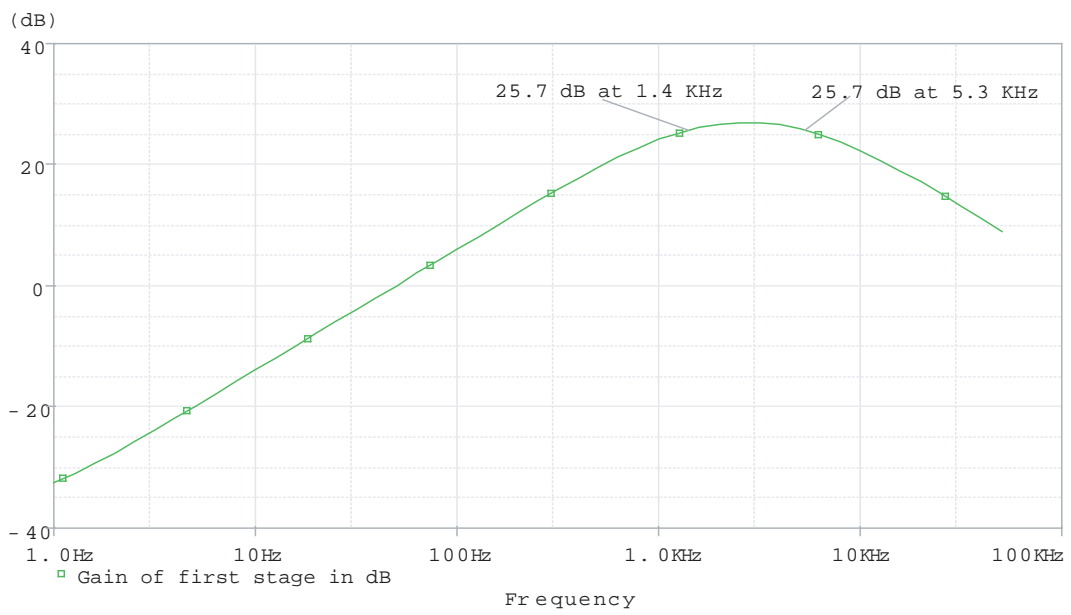
□ Gain of first stage in dB

Frequency

FIGURE 3.25. Frequency response of first stage. The amplified difference of two LPFs with cutoff frequencies of 1.4 KHz and 5.3 KHz respectively was simulated (Spike Enhancement in Figure 3.24), the response is shown over the 1-10K Hz frequency range.
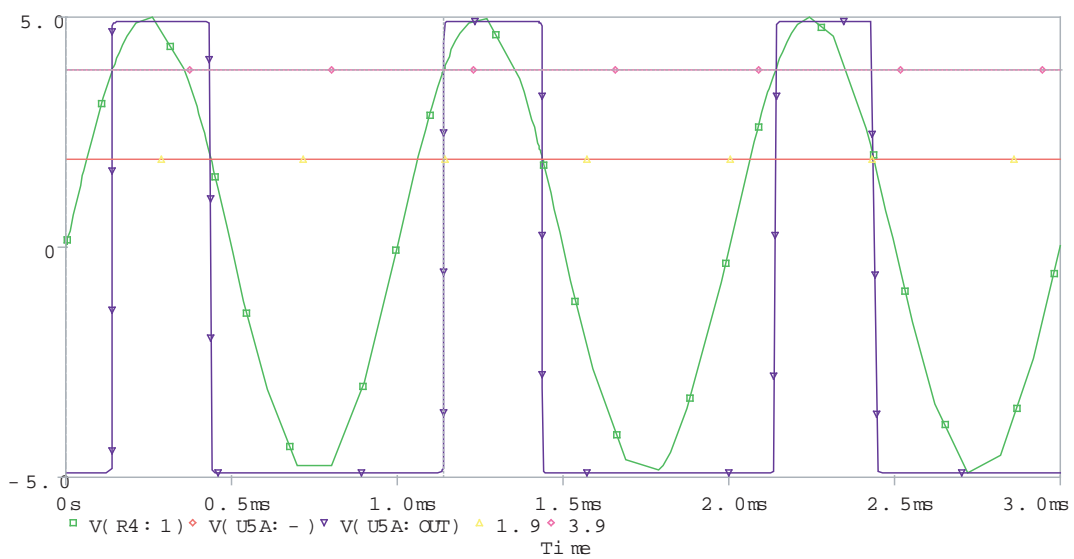
FIGURE 3.26. Spike detection simulation. A sinusoid with an amplitude of 5 V and frequency of 1 KHz was used as input of this stage. The output was observed over a period of 3 ms. The hysteresis shown in the plot is of 2 V, where the high threshold is at 3.9 V and the low threshold is 1.9 V. The output of this stage goes high when the input goes above the high threshold, and it goes low when the low threshold is reached. This plot shows the input and the output waveforms, as well as the switching levels.

Spike Rate Calculated Output Voltage

a)

b)

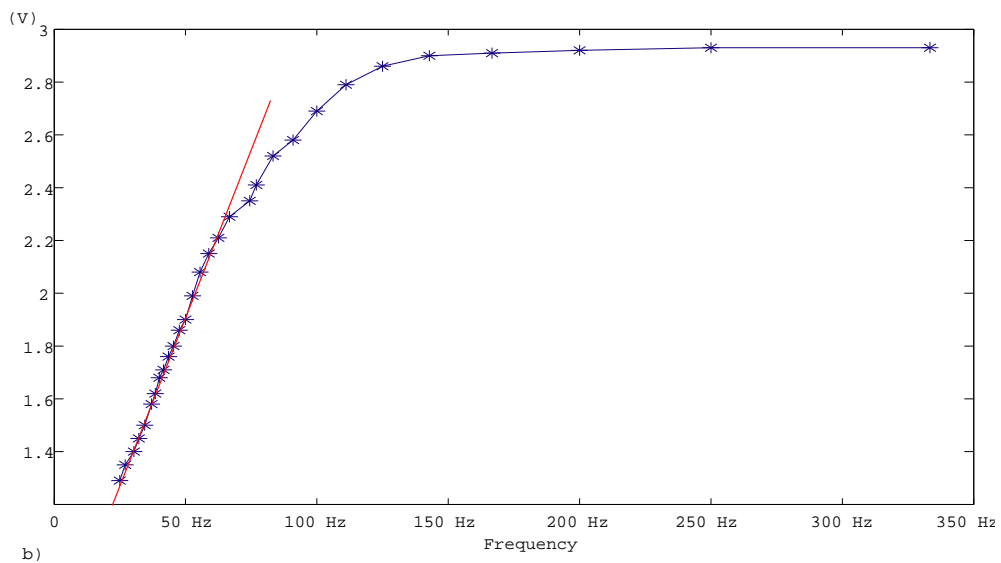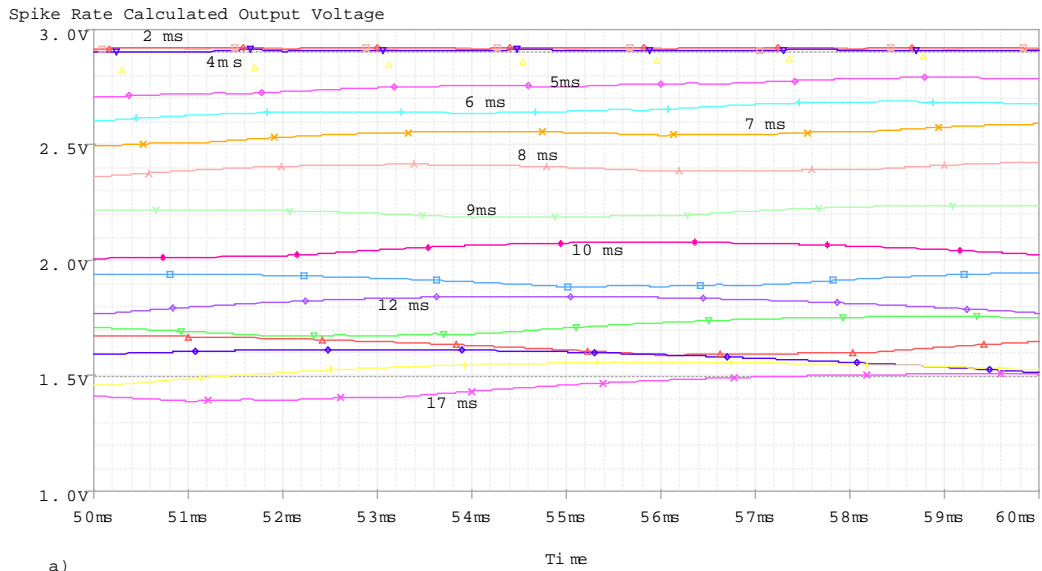FIGURE 3.27. PSpice results of spike rate computation. a) A square wave simulating detected spikes was used as input for the rate computation circuit. Simulations were repeated for square waves with different periods but with the same pulse width. The plot shows how the output of this circuit changes as the period (and rate) changes in the input waveform. b) Plot of the spike rate versus the output voltage.

3.3.1 Data Acquisition

A data acquisition system has the purpose of sampling an analog signal to generate data that can be processed by a digital device such as a computer. This can be achieved by using an ADC and a microprocessor. The microprocessor is in charge of controlling the ADC and manipulating the data once it has been sampled by the ADC (offset circuit not shown). It also provides the communication between the board and the computer via a serial port. Figure 3.28 shows a block diagram of the integration of the data acquisition system to the board.

There are many microprocessors commercially available that are suited for the task. The microprocessor chosen was the ATMEGA168 from Atmel Corporation. This processor has a 16k byte self-programming flash memory, a 1k byte SRAM, a 512 bytes EEPROM, an 8-channel 10-bit A/D converter, and up to 20 MIPS throughput at 20 MHz. This microprocessor was chosen because of all the features previously mentioned and because of its relatively small size (it only has 28 pins). This processor has also a bootloader option that allows the user to program it through the serial port. This is very useful for this project since it means that we can communicate with the system to send commands, read data, change settings, and reprogram the device all through the serial port.

The bootloader is a small program that is saved in a specific place in the processor's memory and that has the job of listening the serial port; when a new program is received, it is in charge of saving the information adequately.

The application program, which is the main code in the microprocessor, contains the algorithm used to compute control sequences for a robot in experiments performed as explained in Chapter 5. This code also allows the user to send specific commands to select various settings as explained in the next subsection. Figure 3.29 shows a simplified flow diagram of the code in the microprocessor.

3.3.2 Wireless Programmability

When conducting this type of experiment, the setup is very delicate since it involves precise positioning of microelectrodes in a living insect. Physically touching the system when a setting on the board needs to be changed can be the cause of a significant setback in the experiment and should be avoided. In order to achieve this, mechanical devices used in the first prototype were replaced in the second prototype by digital devices in the analog recording channels. Additionally, wireless communication was implemented by including a Bluetooth device; ultimately providing a remote interface with the board.

All mechanical potentiometers and switches needed for selecting gains and cutoff frequencies in the first prototype were replaced by digital ones in the second prototype. The components suitable for this design have to support bipolar signals and therefore need to have dual power supplies. There is a limited number of available output
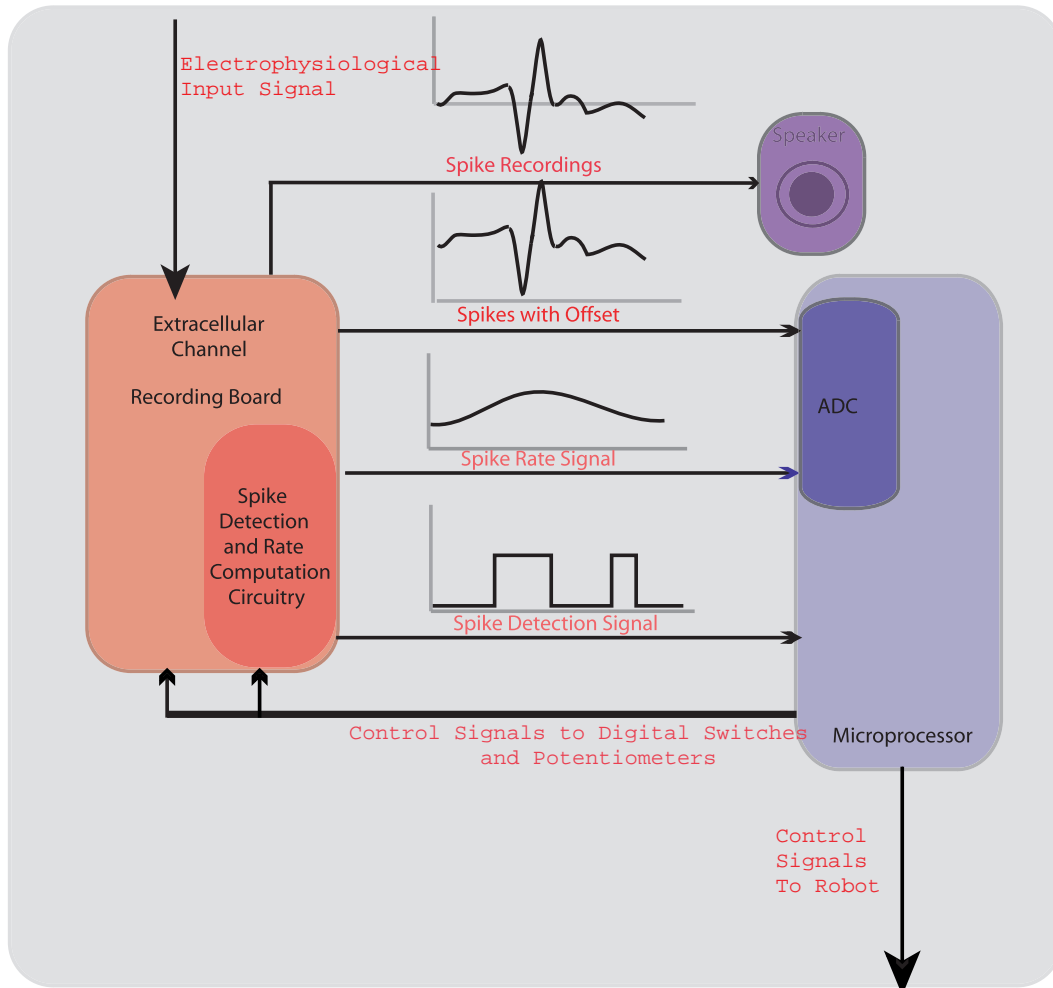
FIGURE 3.28. Extracellular channel and data acquisition block diagram. Each extracellular channel has four different outputs. The first is the filtered and amplified signal after going through the four stages explained in Section 3.1.1. This signal can be directly connected to a speaker. The second output connects to the ADC. This signal is the same as the first output with an additional offset to eliminate negative voltages which can damage the ADC (offset circuit not shown). The third output is the spike rate computation; this signal is positive and it is directly connected to the ADC. The final output signal is the output of the spike detection circuit. This is a digital signal that does not need to be sampled and it is connected to a microprocessor digital input. The microprocessor manipulates the information provided by the analog circuit and computes the control signals that will go to the mobile robot.
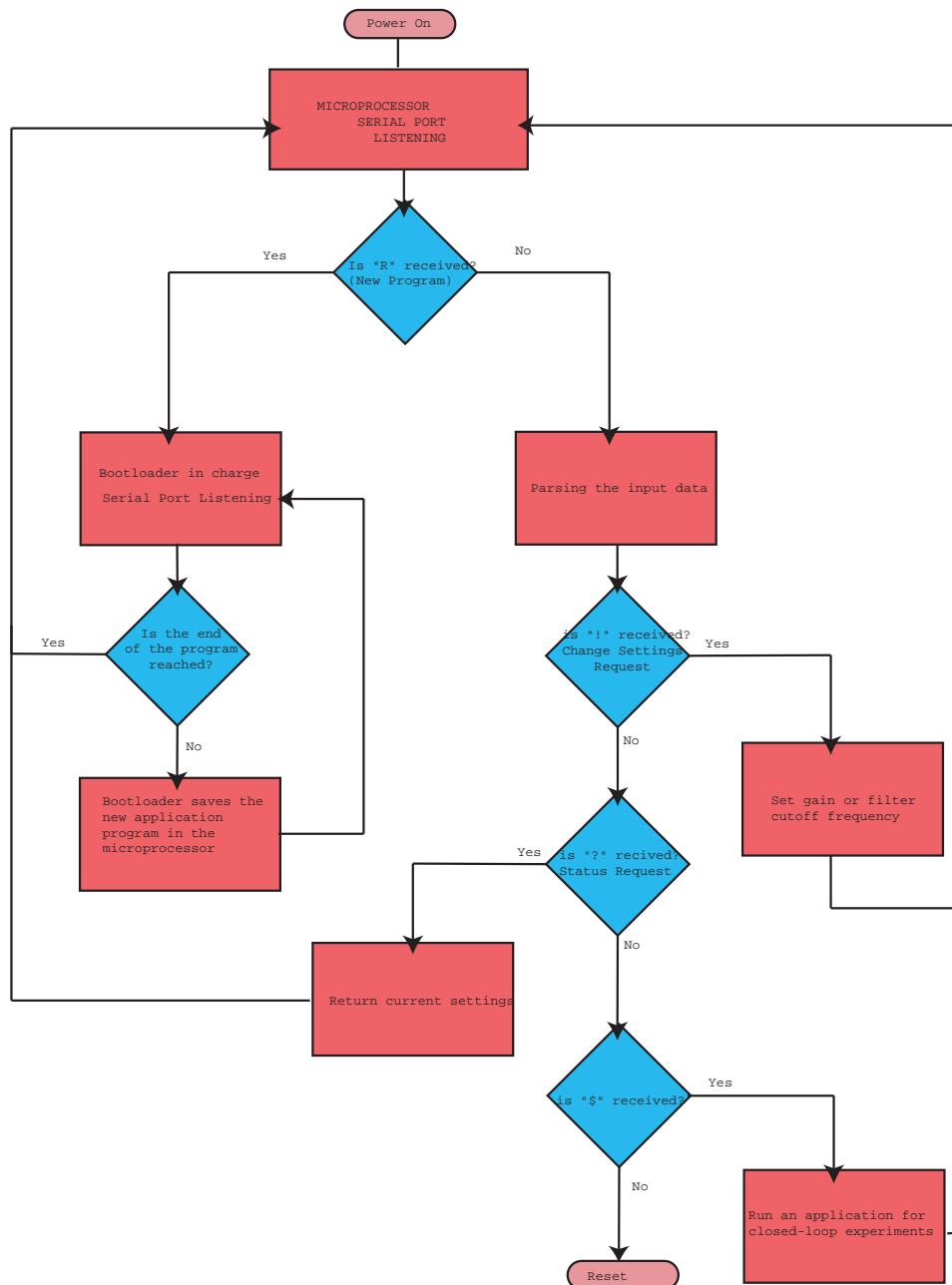
FIGURE 3.29. Microprocessor code flow diagram. Initially, the application program is in control. The data received through the serial port is parsed, and according to this data the program goes to different functions. When a new application program is received, the bootloader is in charge of saving the new program in the appropriate space in memory.

pins in the microprocessor and therefore components supporting serial or Two-Wire Interface (TWI) are ideal for this application. Nine switches and 21 potentiometers are needed to control three extracellular channels with spike detection and rate calculation circuits. Six Intersil X9258 low noise and low power quad digitally controlled potentiometers chips were used. These $100K\Omega$ potentiometers have a 2-wire serial interface and a non-volatile storage of wiper position. Each has a 4-bit device address which can accommodate up to 16 devices on the same serial bus. This bus uses two bidirectional lines where instructions are sent between the microprocessor and the potentiometers. Additionally, 3 MAXIM MAX394 low voltage quad SPDT analog switches were used. These switches do not have a serial port and need one control line per switch, but they were chosen because they have bipolar supply operation and handle rail-to-rail analog signals. For three extracellular channels the number of control lines required to control the switches are 6. Figure 3.30 shows a block diagram of one extracellular channel including the digital devices required to implement software programmability.

Finally, wireless communication was implemented by adding a Bluetooth v2.0 DIP module from Spark Fun Electronics to the board. This module consists of a Blue Radio BR-C40 class 1 radio modem with a serial interface with 100 meter range. It was chosen based on small size and easy configuration. Once this module was connected to the serial port of the microprocessor, the communication between the board and a computer with Bluetooth capability was completely wireless. Figure 3.31 illustrates the different types of information that can be exchanged via the wireless link.

Figure 3.32 shows an extracellular channel schematic with the entire digital design incorporated.

3.4   Layout and Fabrication

The fabrication of a PCB was the next step in the prototype design and the EAGLE Layout Editor was the software used to create the layout of the board. Although PCB layout might seem an easy task for small circuits, it involves a lot of design when components are numerous and there is a constraint on the board size. The first step in this process was to create a complete and accurate schematic that includes all connections between devices. Footprints not found in standard libraries were manually drawn according to size specifications obtained from datasheets. Once the placement of all parts was finished, the signals had to be routed. A very helpful tool available in EAGLE is the autorouting tool. This tool is used as an aid in the routing process but many parts had to be routed manually in order to optimize the layout. The main issues to take into account when laying out a board are:

1. Routing trace size. Thicker traces have lower resistances but take more space. In general, power lines as well as the main signal line should be bigger than
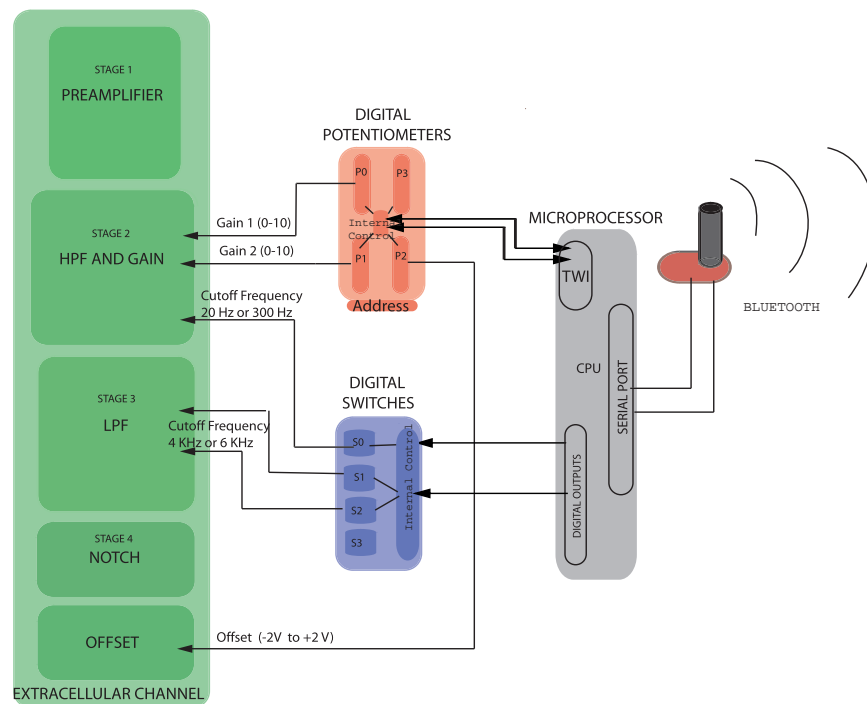
FIGURE 3.30. Software programmable extracellular channel. All mechanical switches and potentiometers were replaced with digital ones which are controlled by a microprocessor. Each channel uses three potentiometers and three switches to select the gain and cutoff frequencies of the filters. The microprocessor has a two-way communication with the 4-potentiometer digital IC via the TWI; and it uses digital outputs to have a one-way communication with with the 4-switch digital IC. The microprocessor uses the serial port to send data through the Bluetooth device.
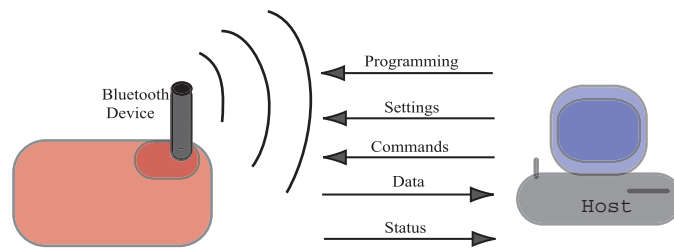
FIGURE 3.31. Wireless communication. The Bluetooth device implements a two-way wireless communication between the board and a computer allowing the user to perform various tasks. First of all, a new application program can be uploaded to the microprocessor whenever is necessary. Secondly, the different recording settings, such as gain and cutoff frequencies, can be selected by sending commands. In addition, other commands can be sent to the microprocessor to start an application during the closed-loop experiments. Finally, recording data as well as the status of the board can be requested at any time from a remote computer.

other lines. Traces should be kept as short as possible.

2. Clearance between traces. It is always better to have more space between traces, especially those containing small signals, which can be affected by very close switching lines. In general, capacitive coupling from trace to trace should be carefully considered.

3. Angles on traces. Using angles larger than 45 degrees should be avoided when possible due to the increased resistance caused.

4. Grounding and Bypassing. It is always better to use separate ground paths for critical parts of the circuit when possible; this will keep noise from one component from affecting others. Using bypass capacitors in all components is also good practice.

Finally, circuit connectivity and electrical clearance between traces, pads and components should be carefully checked before sending the board for fabrication. For this purpose EAGLE has a tool called DRC (Design Rule Checking) which checks the board based on a set of design rules that are previously assigned. Layout files were sent out for fabrication to PCBexpress. Once the fabricated PCB board was received, all components were manually soldered. Later, the board was tested and final results are included in the next chapter.
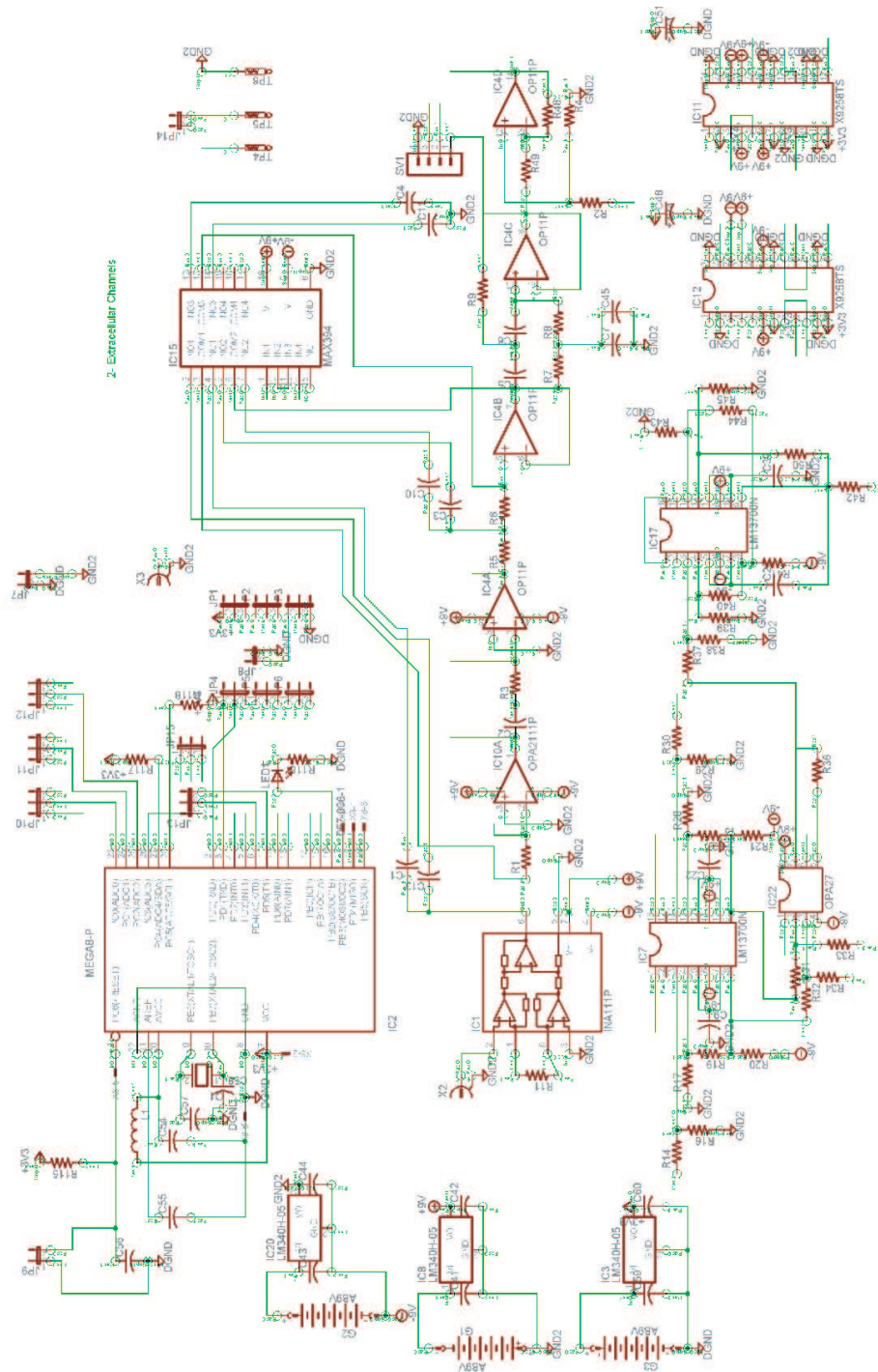
FIGURE 3.32. Digital design. This schematic shows the digital design added to the extracellular channel including microprocessor, digital potentiometers, digital switches, and Bluetooth connections.

3.4.1 First Prototype: Amplification and Filtering Board

All circuits mentioned in Section 3.1 were fully tested on a breadboard, and once they were working as expected the first PCB prototype was built. This prototype is all analog, and contains two extracellular channels and two intracellular channels. Figure 3.33 shows the final layout of this two-layer prototype, and Figure 3.34 shows the fabricated prototype. BNC connectors were chosen to carry the input signal. In order to utilize the minimum space, pin headers and jumper shunts were used instead of mechanical switches as a way of selecting all various board settings. There is also a reference electrode BNC connector which can be used as reference ground for the system. Optionally, the BNC shields can also be connected to the reference electrode signal with a jumper shunt. All outputs are available through pin headers.

3.4.2 Second Prototype: Amplification, Filtering, and Data Acquisition Board

The second prototype built integrates recording channels with data acquisition capability. It contains three extracellular channels from Section 3.1.1, and digital circuitry from Section 3.3. On this board, significant changes were made to the extracellular channels from the first prototype after some experiments revealed the need for different gains and cutoff frequencies. The different gains are achieved because instead of using various resistors to provide different gains, digital potentiometers were used. This board includes LPF cutoff frequencies of 4 KHz and 6 KHz instead of 6 KHz and 10 KHz available in the first prototype. Additionally, an offset circuit was included at the output of the recording channels to avoid negative voltages going to the ADC since it only has a positive power supply and could be damaged by negative voltage signals.

The integration of digital devices into an analog circuit involves certain techniques to avoid introducing extra noise. As far as the layout is concerned, the devices were placed on the board such that high speed and digital devices were closest to the output connectors. A block diagram of this board is shown in Figure 3.32. Figure 3.35 shows the final PCB layout of this board, and Figure 3.36 shows the fabricated prototype.

3.5 Summary

PSpice simulations were conducted to verify a design proposed in Rivera-Alvidrez, 2004 for an electrophysiology board. Additionally, spike detection and rate calculation circuitry was designed and verified using PSpice. After simulation results showed acceptable data, a prototype board was constructed for extracellular and intracellular recordings. Later, digital circuitry was incorporated into the design to provide more features including data acquisition. A second prototype containing both analog and
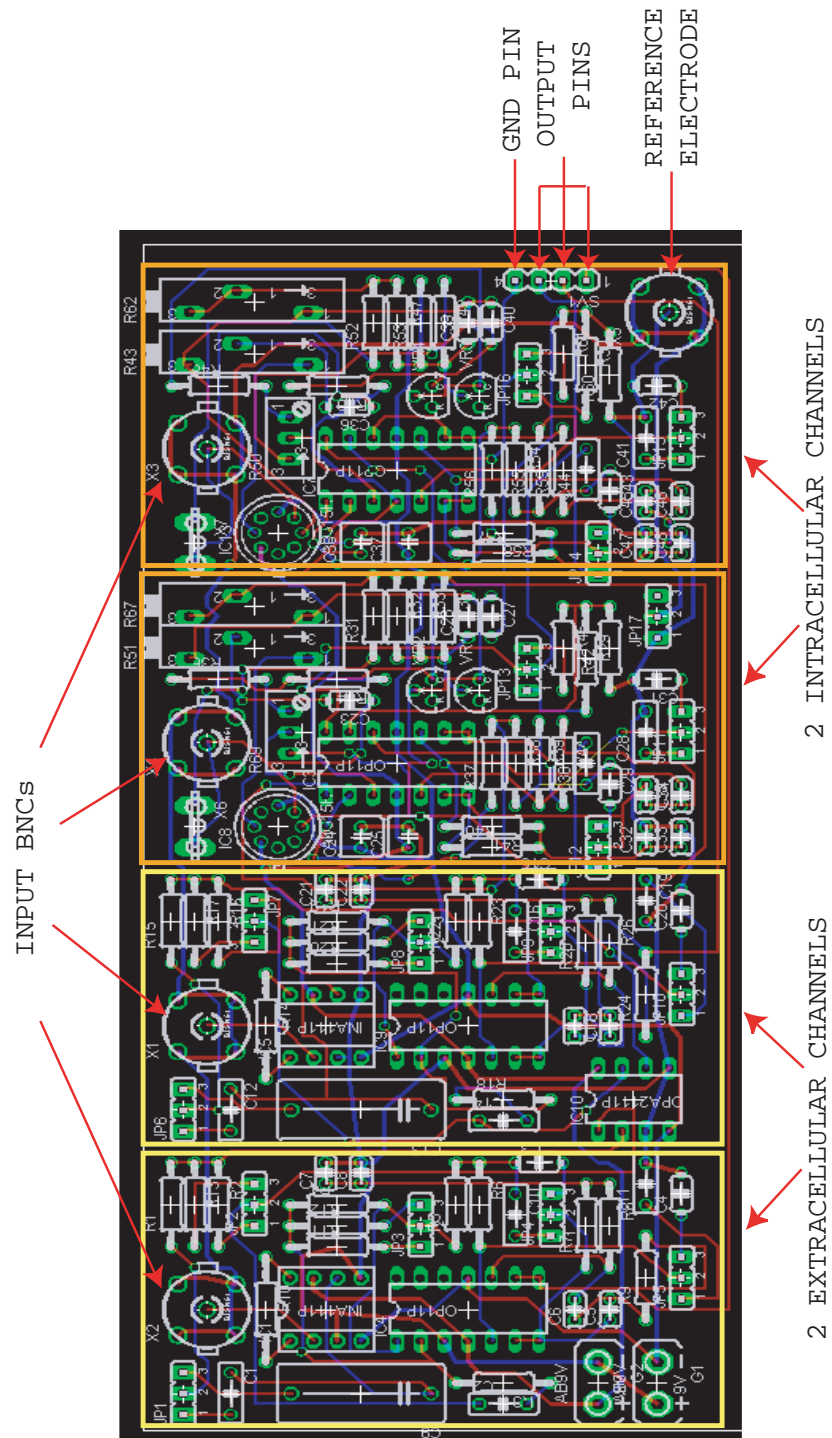
FIGURE 3.33. Actual size illustration of the first prototype layout. This prototype implemented two extracellular channels and two intracellular channels.
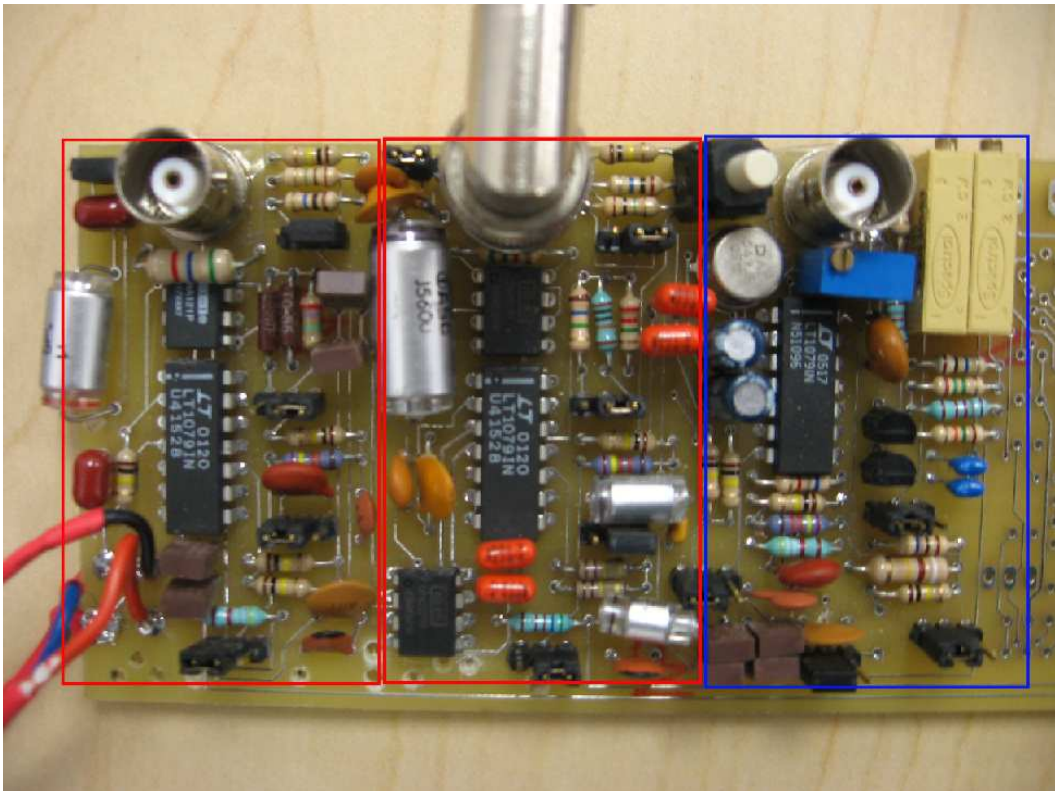
FIGURE 3.34. Photo of the first fabricated prototype. This photo shows three boxed channels; the leftmost two are extracellular, and the remaining one is intracellular. This PCB uses mechanical potentiometers, headers, and jumpers to select the various settings. Two 9 V batteries are required to operate this board.
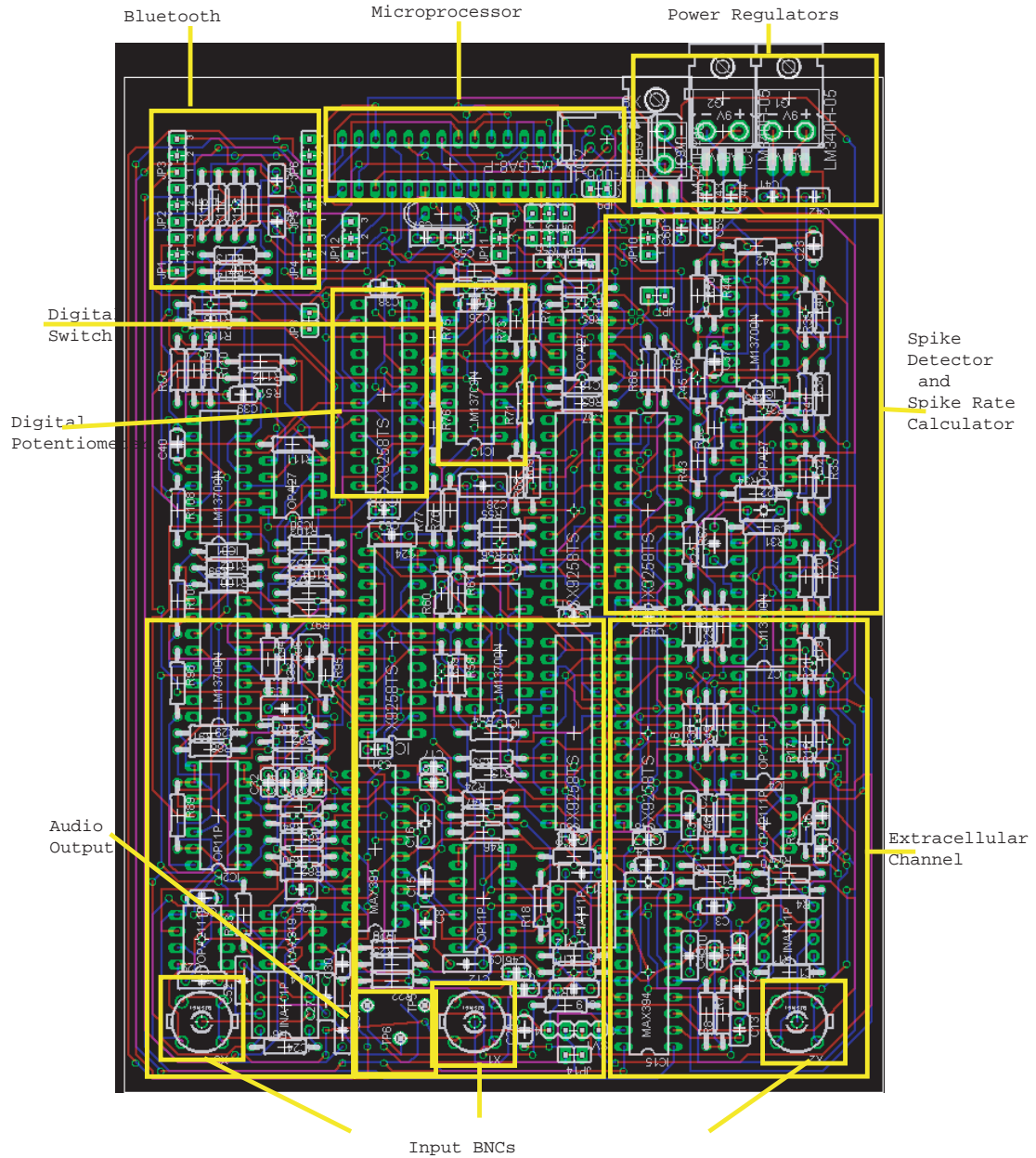
FIGURE 3.35. Actual size illustration of the second prototype layout. This board integrates a 3-channel extracellular electrophysiology board with spike detection and spike rate calculation circuits, and a data acquisition board as shown in Figure 3.32.
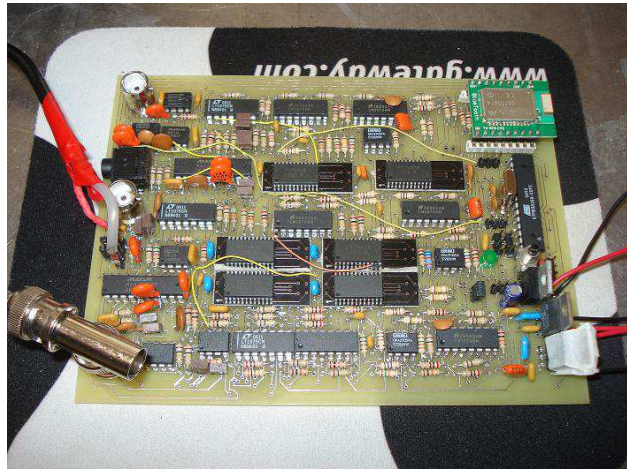
FIGURE 3.36. Photo of the second fabricated prototype. This PCB has three extracellular channels, each with a spike detector and spike rate calculation circuit. Most digital components are located on the right hand side of the board; from top to bottom we see: the Bluetooth device, the microprocessor and the voltage regulators. This board uses digital potentiometers and switches to select the various settings, and it operates with two 9 V batteries.

digital devices was constructed. This prototype can be used as a standalone device in experiments, and is especially suitable for its wireless capability.

Chapter 4

Electrophysiology Board Experimental Characterization Results

This chapter presents the results obtained after testing was performed on both constructed prototypes. The boards were tested with artificial as well as biological data for two main purposes: firstly, to verify if design specifications such as gain and cutoff frequencies were close to those expected; secondly, to qualify the overall performance of the boards compared to the performance of a commercially available system.

4.1 Performance Verification with Artificial Signals

The first prototype board was tested using a sinusoidal signal created by an SRS Model DS40 function generator and this section shows the results obtained. Gains and filter cutoff frequencies were verified by performing a frequency sweep for all extracellular and intracellular channels. The results were compared to PSpice simulations shown in Section 3.2 by plotting them on the same figure. Figures 4.1a and 4.1b show the resulted frequency response from one extracellular channel for two different filter settings. Figures 4.2a and 4.2b show the resulted frequency response for one intracellular channel for two different filter settings. All other channels showed similar plots. The PSpice simulations and actual physical tests show almost identical cutoff frequencies and gains.

4.2 Verification of Spike Analysis with Simulated Biological Data

In this section, simulated biological data were used to test the spike detection circuitry of the second prototype. The artificial data used for these experiments were created using a Noisy Spike Generator tool written in the MathWorks Matlab software (Smith and Mtetwa, 2006). This tool is used to generate noisy spike trains to simulate spike signals obtained from extracellular neural recordings. Figure 4.3 shows an example of the artificial data obtained using this tool that was used in some of the experiments. This data was converted into a "wav" file which was played by a media player in the computer. The audio output of the computer was used as the input from an extracellular channel in the first prototype. Figure 4.3 also shows the output signal of the extracellular channel before and after the spike detection circuitry. All artificial spikes were successfully detected by the circuitry with the correct adjustment of the
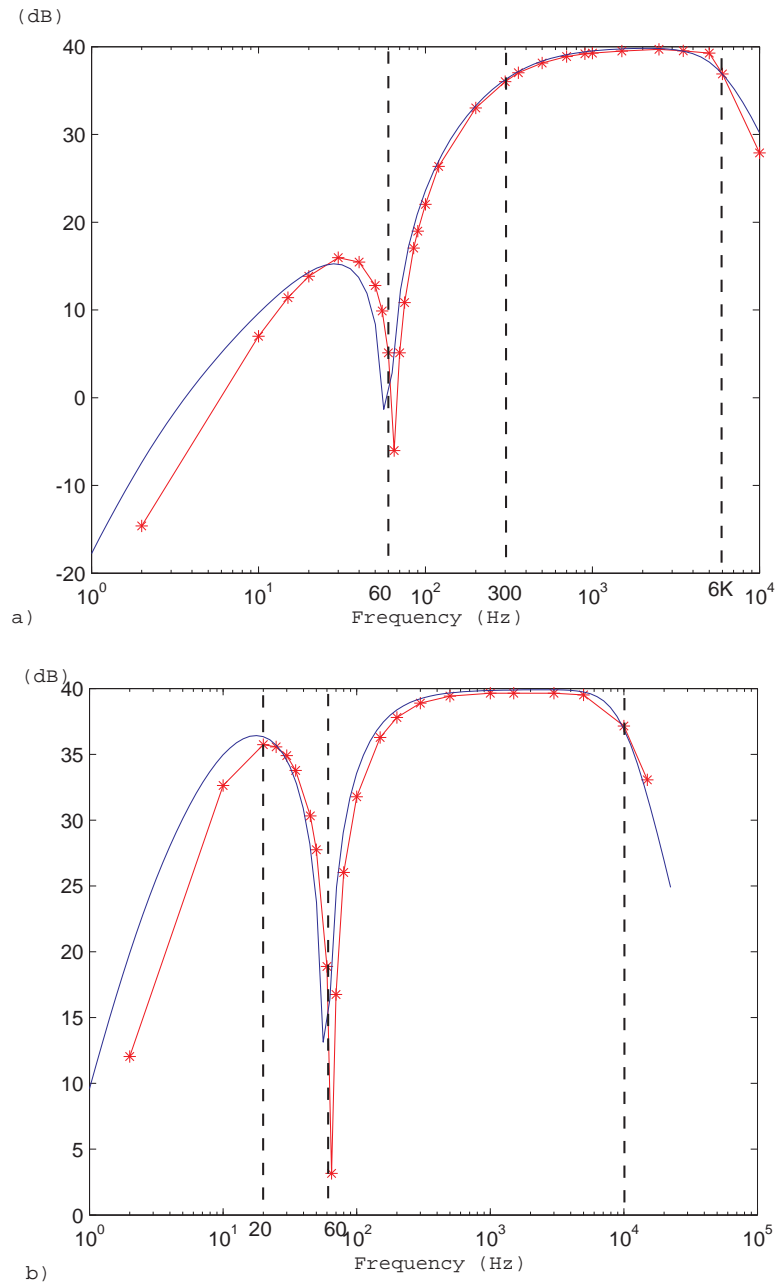
FIGURE 4.1. Frequency response of extracellular channel. The solid plot represents the simulation results from PSpice. The line with the asterisks shows the measured experimental results from the first prototype board. a) Frequency response with settings of 300 Hz HPF and 6 KHz LPF. b) Frequency response with settings of 20 Hz HPF and 10 KHz LPF.
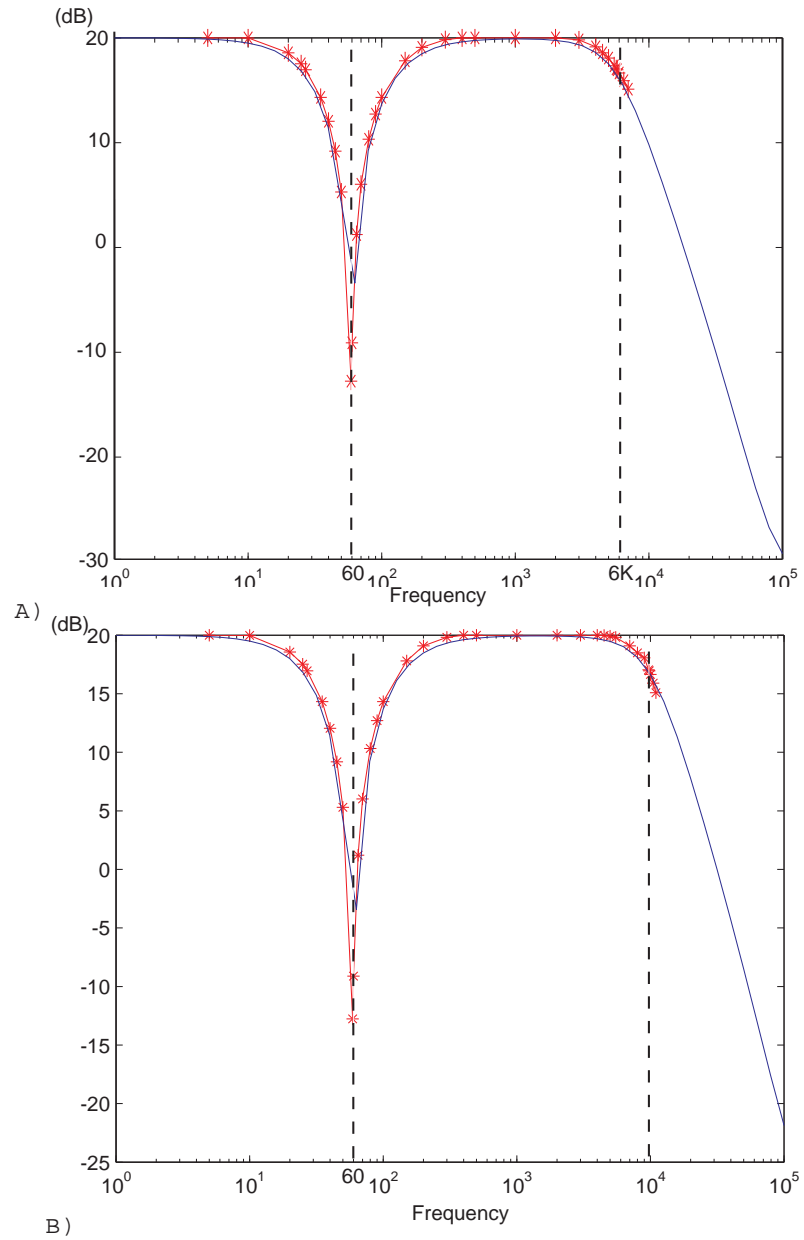
FIGURE 4.2. Frequency response of intracellular channel. The solid plot represents the simulation results from PSpice, and the line with the asterisks shows the measured experimental results from the first prototype board. a) Frequency response with settings of 6 KHz LPF. b) Frequency response with settings of 10 KHz LPF.

threshold. In these results the upper threshold (low-to-high transition) was 0.59 V, and the lower threshold (high-to-low transition) was 0.43 V.
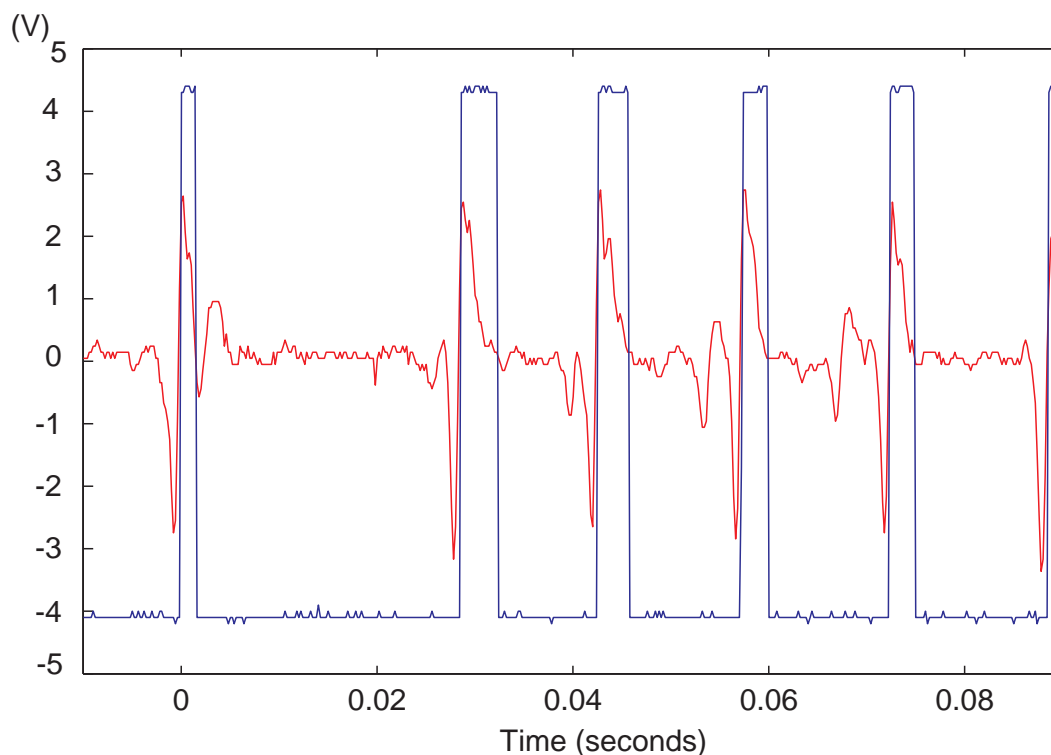

FIGURE 4.3. Verification of spike detection circuitry. This plot shows the input signal that goes into an extracellular channel (second prototype) and it also shows the output signal after the spike detector. All spikes in the signal are successfully detected when the thresholds are set to 0.59 V for low-to-high transitions and 0.43 V for high-to-low transitions.

The number of spikes and the amount of noise in the artificial data can be controlled; this was found especially helpful when testing the spike detection and rate computation circuitry.

4.3 Performance Verification with Biological Data

In this section, real biological data was used to test both prototypes and results were compared to signals recorded using commercially available equipment. It should be noted that the extracellular channels were tested with biological data more extensively than the intracellular channels. This is because extracellular recordings are of more importance to the overall biorobotics project.

SPECIFICATION	A-M SYSTEMS 1700	1st PROTOTYPE
Typical Noise	$1\mu V_{p-p}$	$10 - 100\mu V_{p-p}$
Input Impedance	$10^{12}\Omega|| > 50pF$	$10^{12}\Omega||pF$*
Input Current	$0.4nA$	$< 0.1nA$*
Current Pump	$1nA$	N/A
HPF Cutoff Frequencies	1, 10, 100, or 300 Hz	20 or 300 Hz
HPF Cutoff Rate	40 dB/decade	40 dB/decade
LPF Cutoff Frequencies	0.5, 1, 5, 10, or 20 KHz	6 or 10 KHz
LPF Cutoff Rate	40 dB/decade	40 dB/decade
Notch Cutoff Frequency	50 Hz or 60 Hz	60 Hz
Notch Rejection	-30 dB	< -40 dB
Bandwidth Gain	100x/1000x/10000x	100x/1000x/2500x/10000x/25000x
CMRR	75 dB	100 dB*
Size	43.2 cm x 12.1 cm x 28.6 cm	16.8 cm x 8.6 cm x 1.6 cm
Weight	19 lbs.	< 1 lb
Power Consumption	> 3 W (110 V)	< 0.2 W ($\pm$9 V)

TABLE 4.1. Extracellular channels specifications. Specifications marked with an asterisk were directly taken from the datasheet of the first stage differential amplifiers (Texas Instruments INA121). This table shows that the commercially available instrument has better noise performance, but the rest of the parameters are identical or worse compared to the first prototype. Additionally the size and power consumption is much lower in the prototype than in the commercially available instrument.

SPECIFICATION	A-M SYSTEMS 1600	1st PROTOTYPE
Capacitance Compensation	-4 pF to 30 pF	0 to 20 pF
Voltage Offset Compensation	$\pm 1V$	$\pm 300mV$
Wheatstone Bridge	$50M\Omega$	N/A
Input Impedance	$10^{11}\Omega$	$10^{13}\Omega||pF$*
Input Current	$30pA$	$< 250fA$*
LPF Cutoff Frequencies	1, 2, 5, 10, 20, 50, or 100 KHz	6 and 10 KHz
LPF Cutoff Rate	40 dB/decade	40 dB/decade
Notch Cutoff Frequency	50 Hz or 60 Hz	60 Hz
Notch Rejection	-50 dB	-35 dB
Bandwidth Gain	1x, 10x	10x, or 100x
Size	43.2 cm x 12.1 cm x 28.6 cm	16.8 cm x 8.6 cm x 1.6 cm
Weight	24 lbs. w/ battery	< 1 lb.
Power Consumption	< 3 W (110 V)	< 0.2 W ($\pm$ 9 V)

TABLE 4.2. Intracellular channels specifications. Specifications marked with an asterisk were directly taken from the datasheet of the first stage differential amplifiers (Analog Devices AD549). Although the commercially available instrument shows slightly better performance in notch rejection and capacitance compensation, the rest of the parameters are almost identical and the prototype is a much smaller device that has relatively low power consumption.

The commercially available equipment used was from AM-Systems: model 1600 for intracellular recordings, and model 1700 for extracellular recordings. Tables 4.1 and 4.2 show the specifications of the commercially available equipment next to the specifications of the electrophysiology boards constructed in this research. In order to compare performance between commercially available and custom made electrophysiology equipment, neural signals (from a blowfly) and EMG signals (from a hawkmoth) were recorded. Five sets of data are included in this chapter. Extracellular electrophysiological signals from the same cell were obtained using both commercially available equipment (AM-Systems Model 1700) and the custom board (first prototype). Figures 4.4 and 4.6 show the signals obtained from two lobula plate tangential cells (LPTC) that respond to wide-field patterns of motion. Figures 4.5 and 4.7 show their respective power spectra. Figures 4.8 and 4.9 show signals from a tonically firing cell in the lobula of the fly, and its power spectrum.

Additionally, 10 seconds of electromyogram (EMG) recording were obtained from a hawkmoth flight muscle. This was done for two different bandwidth settings and Figures 4.10 and 4.12 show the recorded signals. Their power spectrum is shown in Figures 4.11 and 4.13 respectively.

In all the cases the power spectrum shows similar harmonics between the commercially available equipment and the first prototype, with the exception that in some

cases 60 Hz and some of its harmonics are present in the first prototype. This was somewhat expected since commercially available equipment is contained in a shielded box of approximately 1/8 of an inch thickness, thus isolating the system from external noise. This feature is currently non-existent in the first prototype; therefore, more noise is expected in noisy environments.
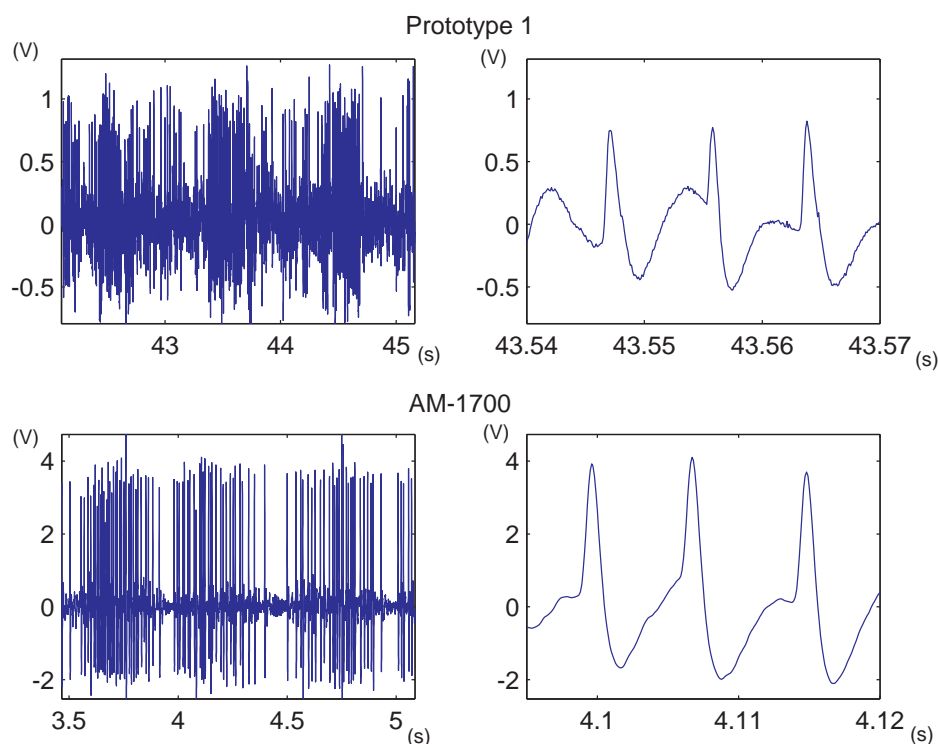

FIGURE 4.4. Extracellular neural recordings from an LPTC in a blowfly. This cell responds to wide-field patterns of motion. These recordings were obtained by Charles Higgins. The x-axis is in seconds and the y-axis in volts. The figures on the left show a few seconds of recorded data while a hand was moving back and forth, and the figures on the right show a typical spike from the recording. The AM-Systems Model 1700 used had the following settings: HPF of 100 Hz, LPF of 1 KHz, and gain of 10000. The first prototype had the following settings: HPF of 20 Hz, LPF of 6 KHz, and gain of 2500. Individual spikes show great similarity.

The intracellular channel was also tested with biological signals obtained from an LPTC in a blowfly and Figure 4.14 shows a few seconds of recorded data. Finally, Figure 4.15 shows the power spectrum of the typical noise present at the time of the neural recordings included in this chapter. To obtain this, the recording electrode was
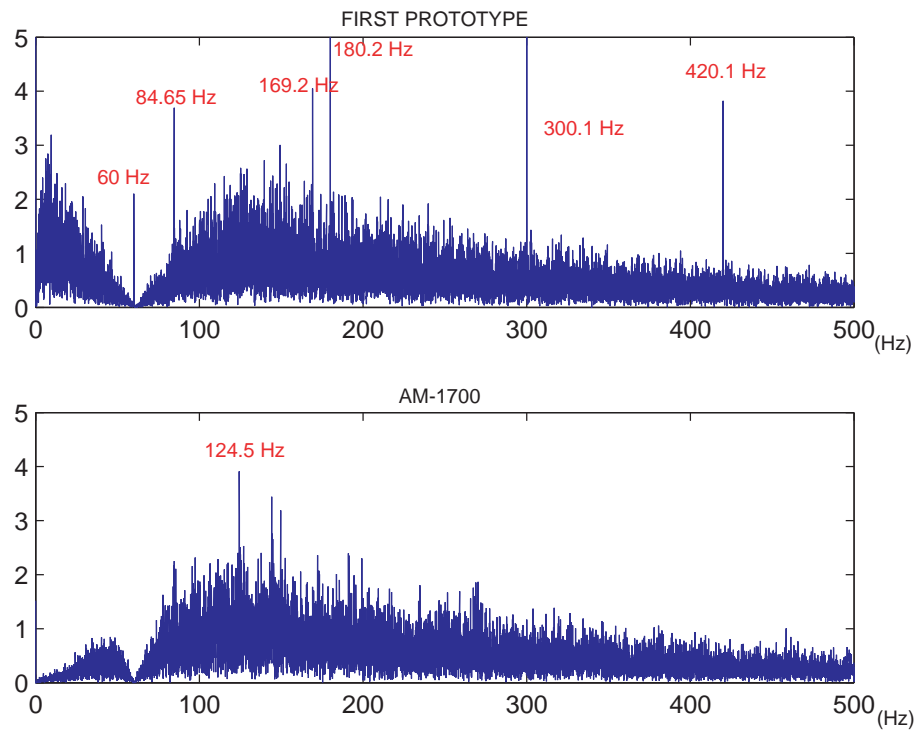
FIGURE 4.5. FFT analysis of data from Figure 4.4. The first difference between the two power spectra is that the first prototype contains more data in the lower frequencies; this is only because the HPF setting at the time of the recording was 20 Hz (versus 100 Hz in the AM-Systems amplifier). Another big difference is the power in the 60 Hz frequency, and some other harmonics (multiples of 60) like 180 Hz, 300 Hz, and 420 Hz. All of these are products of the noisy environment and the lack of a shielded cage around the first prototype. Other than those differences the spectra are very similar.
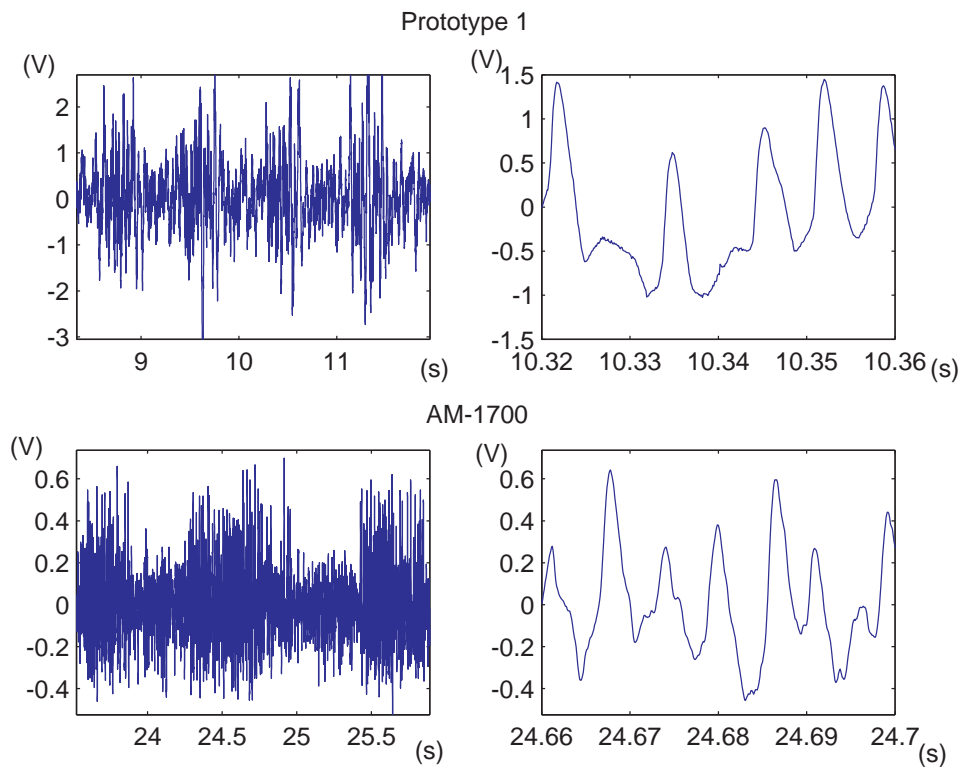
FIGURE 4.6. Extracellular neural recordings from an LPTC in a blowfly. This cell responds to wide-field patterns of motion. These recordings were obtained by Charles Higgins. The x-axis is in seconds and the y-axis in volts. The figures on the left show a few seconds of recorded data while a hand was moving back and forth, and the figures on the right show a typical spike from the recording. The AM-Systems Model 1700 used had the following settings: HPF of 100 Hz, LPF of 1 KHz, and gain of 10000. The first prototype had the following settings: HPF of 20 Hz, LPF of 6 KHz, and gain of 2500. Individual spikes show great similarity.
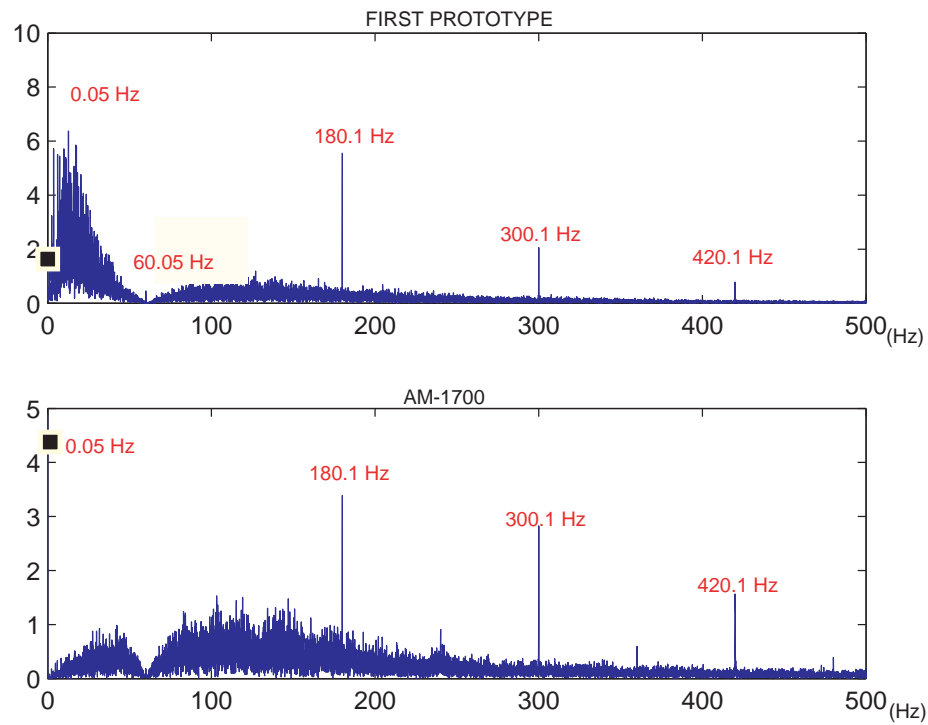
FIGURE 4.7. FFT analysis of data from Figure 4.6. The first difference between the two power spectra is that the first prototype contains more data in the lower frequencies; this is only because the HPF setting at the time of the recording was 20 Hz (versus 100 Hz in the AM-Systems amplifier). Another (small) difference is the power in the 60 Hz frequency, and some other harmonics (multiples of 60) like 180 Hz, 300 Hz, and 420 Hz. In this case they are present in both spectra, but the first prototype shows higher power than the AM-Systems amplifier. Again, all of these are products of the noisy environment and the lack of a shielded cage around the first prototype. Other than those differences the spectra are very similar.
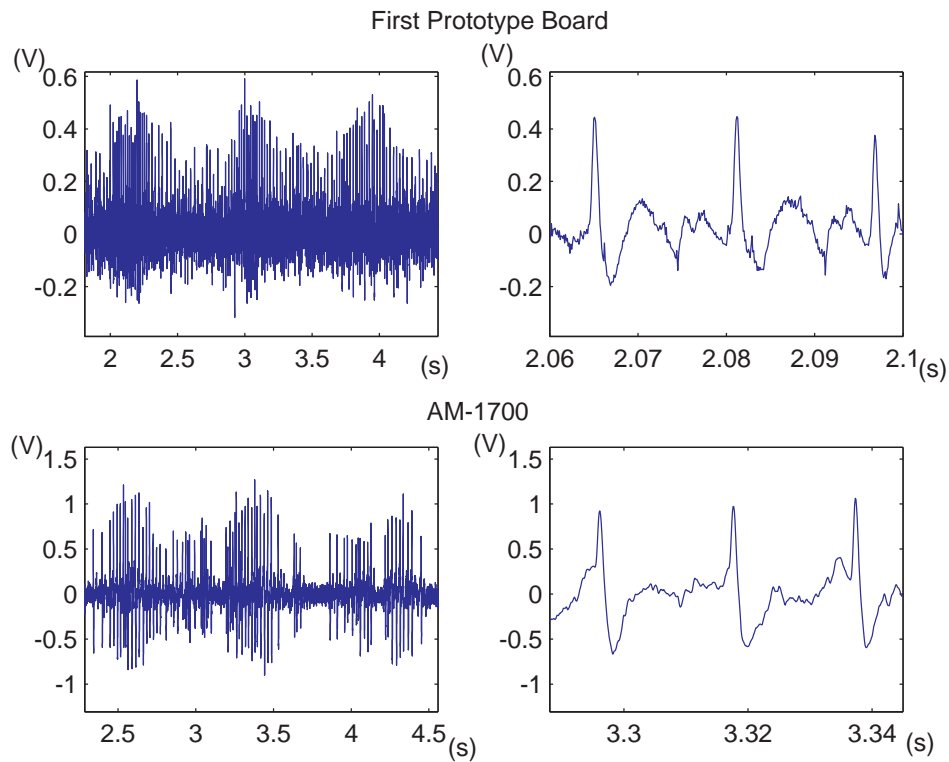
FIGURE 4.8. Extracellular neural recordings of a tonically firing cell in a blowfly. This cell responds to wide-field patterns of motion. The x-axis is in seconds and the y-axis in volts. These recordings were obtained by Charles Higgins. The figures on the left show a few seconds of recorded data, and the figures on the right show a typical spike from the recording. The AM-Systems Model 1700 used had the following settings: HPF of 100 Hz, LPF of 1 KHz, and gain of 10000. The first prototype had the following settings: HPF of 300 Hz, LPF of 6 KHz, and gain of 2500. Individual spikes show great similarity.
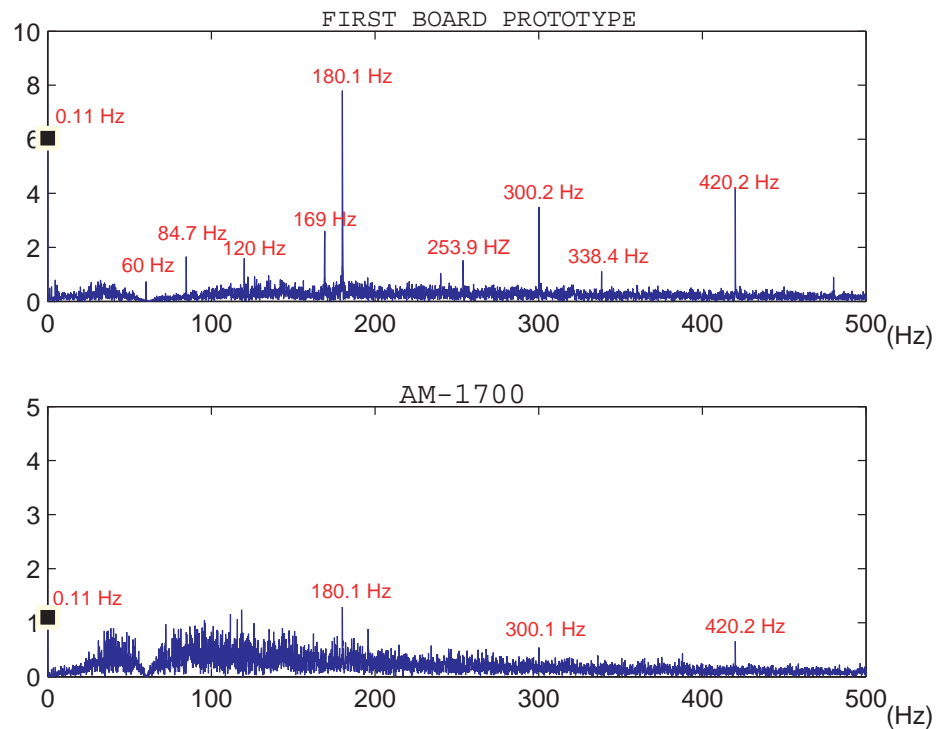
FIGURE 4.9. FFT analysis of data from Figure 4.8. In this case, the HPF setting at the time of the recording was 300 Hz and there is not much difference as far as the lower frequencies spectrum. Higher power in the 60 Hz frequency, and some other harmonics (multiples of 60) like 120 Hz, 180 Hz, 300 Hz, and 420 Hz, is again seen in the first prototype. Additionally there are other frequencies that are significantly big like 84.7 Hz, 169 Hz, and 254 Hz in the first prototype. This shows that this particular recording might have noise from different sources, but Figure 4.8 shows that the spikes recorded still show significant similarities.
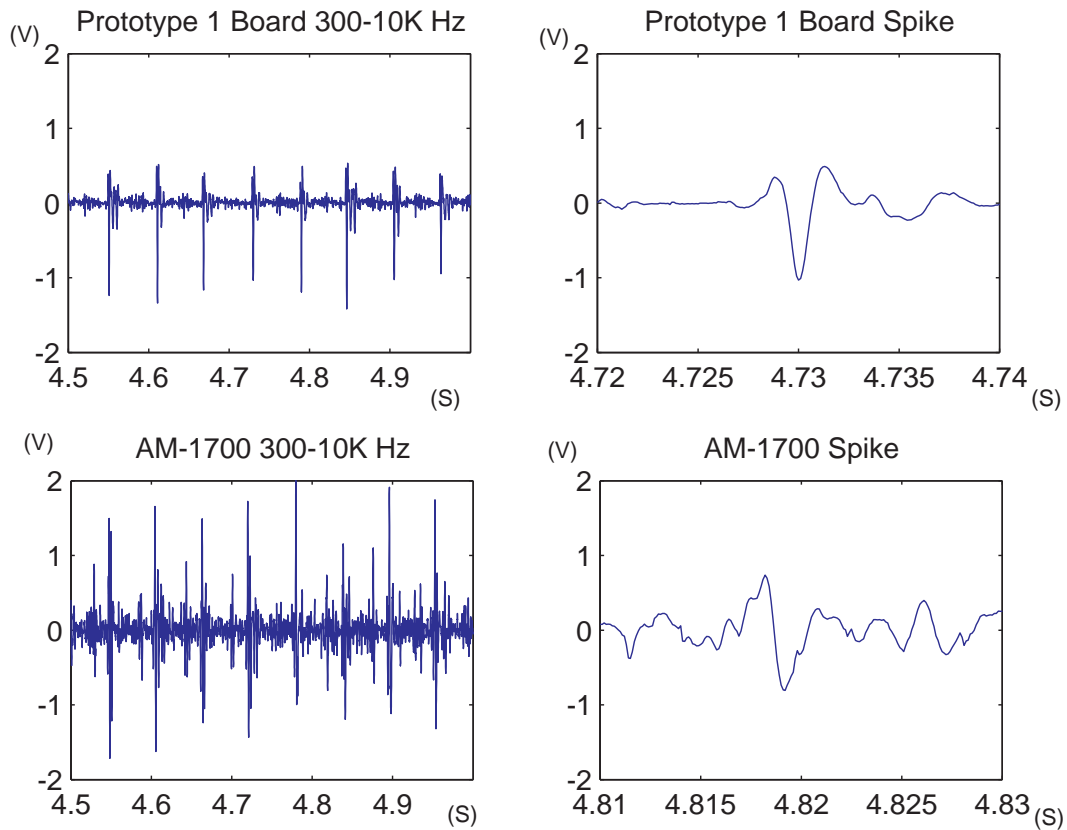
FIGURE 4.10. EMG recordings from a flight muscle in a hawkmoth. These recordings were obtained by Tim Melano. The x-axis is in seconds and the y-axis in volts. The figures on the left show 0.5 seconds of recorded data, and the figures on the right show a typical spike from the recording. The commercially available instrument used and the first prototype had the same settings at the time of the recording: HPF of 300 Hz, LPF of 10 KHz, and Gain of 100.
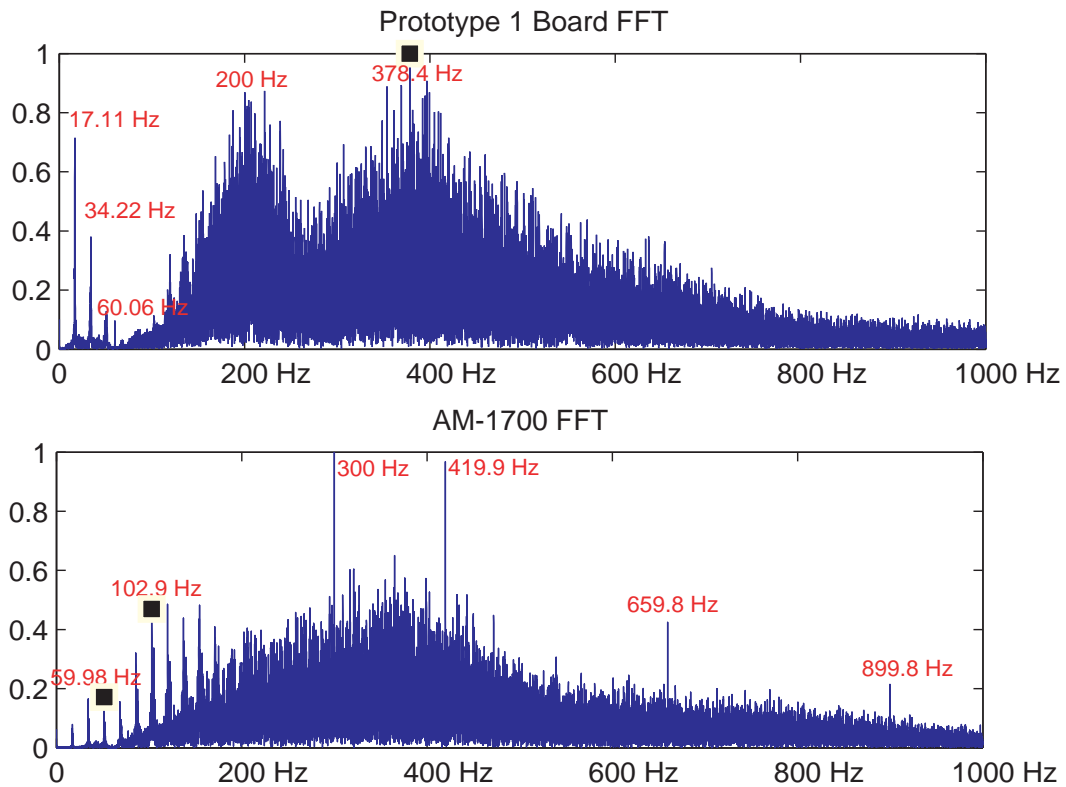
Figure 4.11. Power spectrum of data from Figure 4.10. The spectrum obtained from the first prototype shows two main problems: firstly, it has a big bump at around 200 Hz; secondly, the power at 17 Hz and 34 Hz is considerably high for a HPF cutoff frequency of 300 Hz. This is the only time this has been observed; in order to explain this phenomenon, more experiments should be performed.
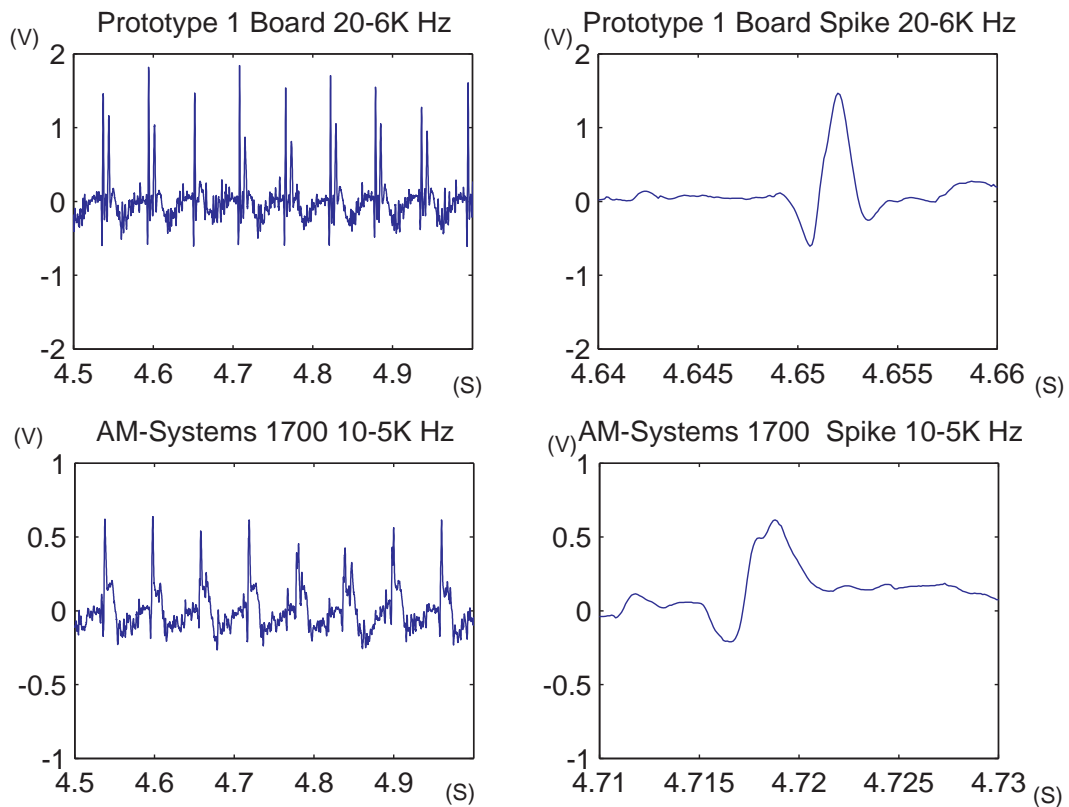
FIGURE 4.12. EMG recordings from a flight muscle in a hawkmoth. These recordings were obtained by Tim Melano. The x-axis is in seconds and the y-axis in volts. The figures on the left show 0.5 seconds of recorded data, and the figures on the right show a typical spike from the recording. The commercially available instrument used had settings of 10 Hz for the HPF and 5 KHz for the LPF; the first prototype had settings of 20 Hz for the HPF, and 6 KHz for the LPF at the time of the recording.

FIGURE 4.13. Power spectrum of data from Figure 4.12. Both spectra show high power in 17 Hz, and 34 Hz frequencies. There is some power in the 60 Hz present in the first prototype. The rest of the spectrum is very similar.

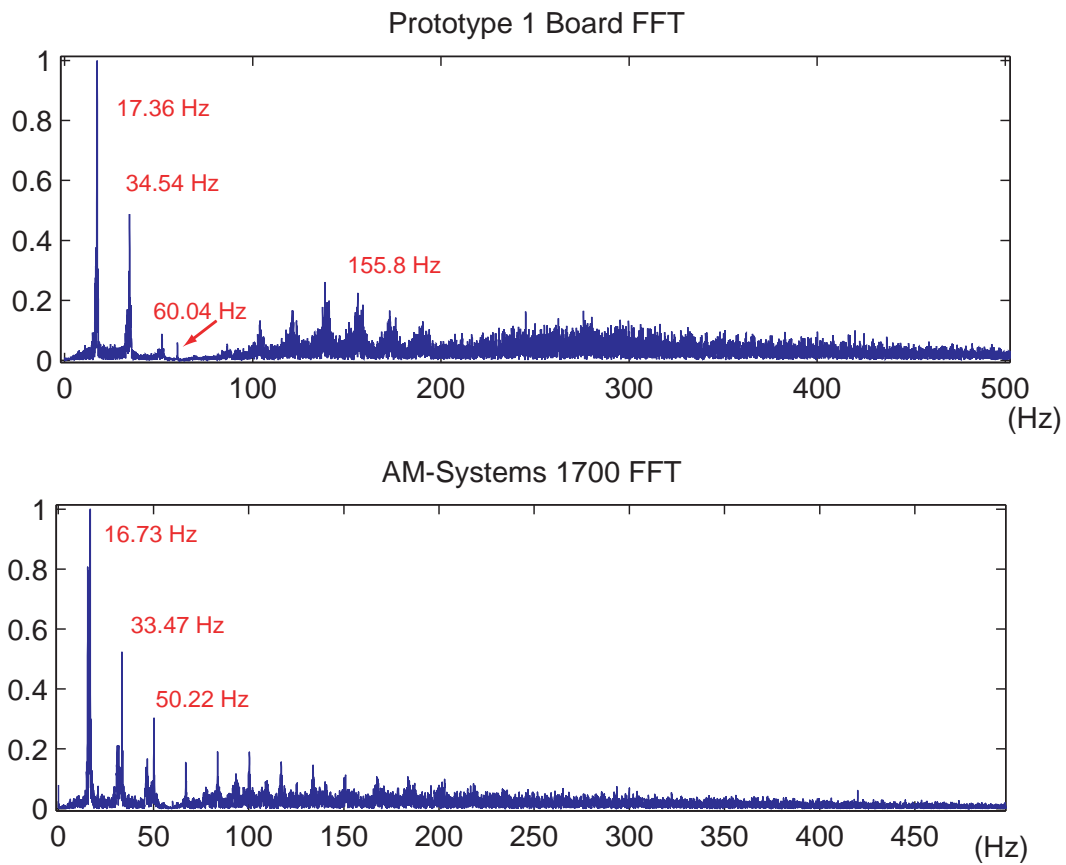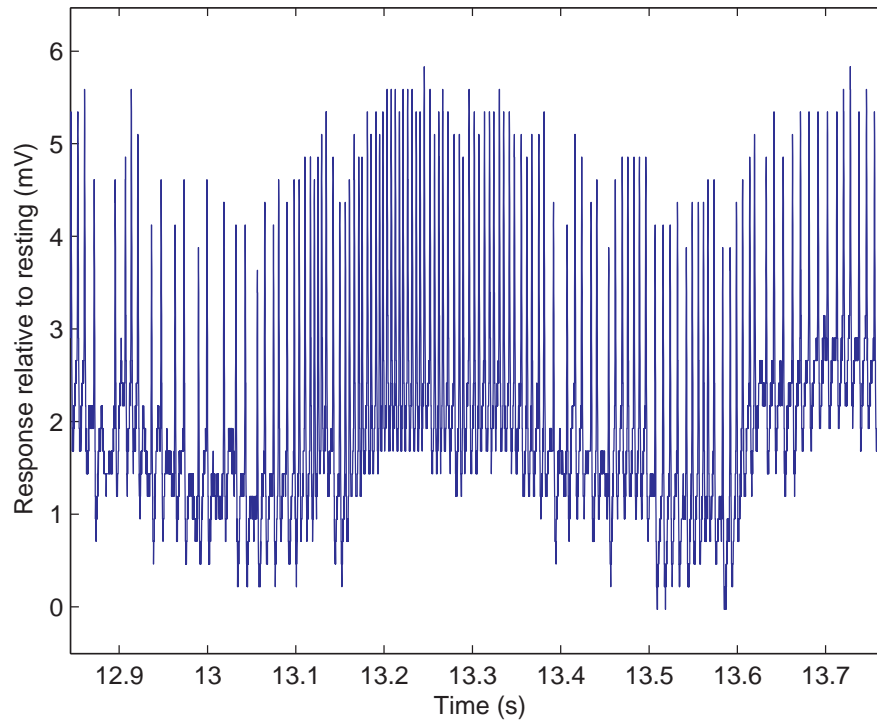FIGURE 4.14. Intracellular neural recordings from an LPTC in a blowfly. This cell responds to wide-field patterns of motion. These recordings were obtained by Charles Higgins. The x-axis is in seconds and the y-axis in volts. The figure on the left shows a few seconds of recorded data while a hand was moving back and forth, and the figures on the right show a typical spike from the recording. The first prototype had the following settings: LPF of 6 KHz, and gain of 100.

placed in the tissue of the insect, but it was not inserted into the brain. Significant power is found in frequencies corresponding to hum and other electrical noise.

FIGURE 4.15. Noise power spectrum. This spectrum was obtained from data recorded with the electrode in the bath but not in the brain by Charles Higgins.

Chapter 5

Mobile Robotics Experiments

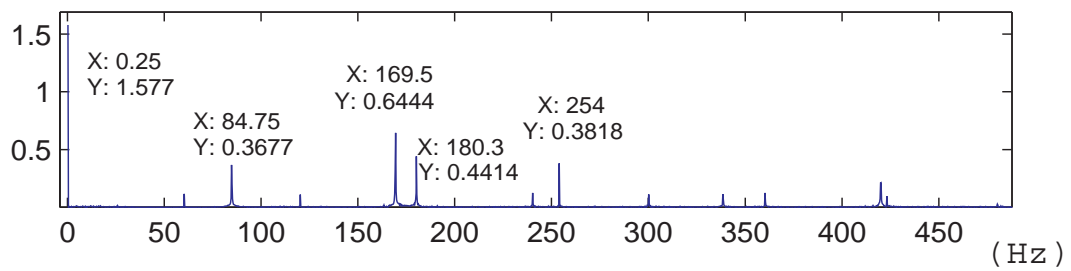The overall goal of the project, of which this thesis describes a part, was to build a reliable platform for closed-loop experiments involving biorobotics. This is a very challenging goal, and complete success in this area is beyond the scope of this thesis; however, a simple experiment was performed in collaboration with Tim Melano, and the results are shown in this chapter. Figure 5.1 shows a block diagram of the elements involved in this closed-loop experiment. First, the system can be divided into artificial, environmental, and biological components. The goal of this experiment was to be able to control the mobile robot just using muscle recordings from the hawkmoth, while doing all the processing required on-board obtaining a completely wireless and autonomous system.
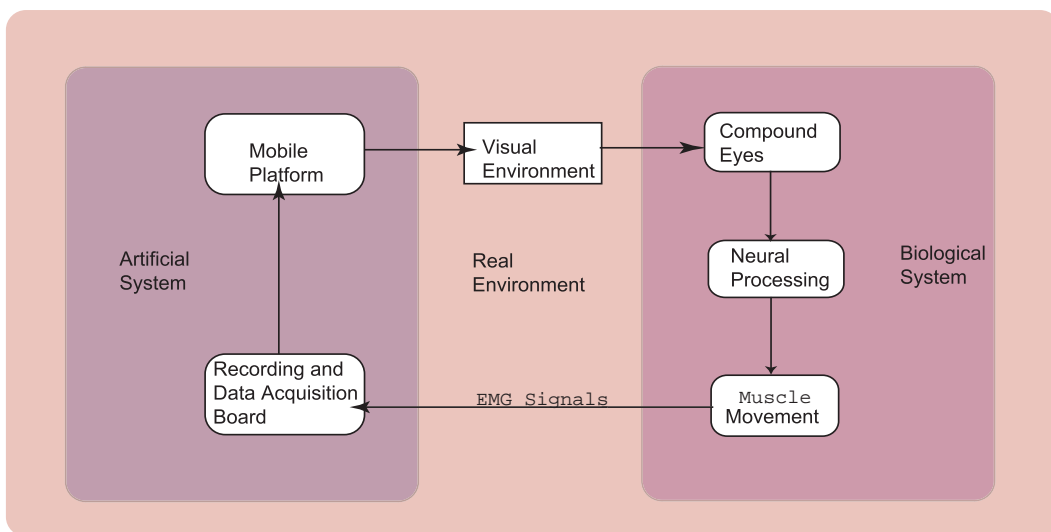
FIGURE 5.1. Closed-loop experiment. The loop involves a communication between the biological and the artificial system. This communication is direct or through the environment. First, the hawkmoth is presented with a visual input that is internally processed. Then, electrodes record flight muscle movements in the hawkmoth. Those signals are detected by the electrophysiology board and later processed by the data acquisition board, which computes the control signals that will go to the mobile platform. The loop is closed by the visual environment surrounding the moth, which will change according to the movement of the robot.

5.1 Methods

The basic idea of this experiment was to obtain electrophysiological signals from the flight muscles of a hawkmoth and use those signals to calculate the control signals for the mobile platform. The robot is expected to move forward whenever the hawkmoth flaps its wings, and stop when there is no movement in the wings. The main components used in this experiment are: the biological system, the mobile robot, and the interface between them. The next sections explain each in more detail.

5.1.1 The Biological System

A hawkmoth (*Manduca sexta*) was used as the biological system (see Figure 5.2). This moth is also called the *tobacco hornworm* because the caterpillars of these moths cause defoliation of tobacco fields. From the Sphingidae family this nocturnal organism is widely used in neurophysiology research because of its short life cycle (they last about 30-50 days, Eichman *et al.*, 2000) and relatively large size (easier dissection). Hawkmoths generate locomotor forces by activating the flight muscles like all flying insects, but variations on aerodynamic forces and torques allow the hawkmoths to have different flight behaviors like fast forward flight and hovering in front of flowers (Hedrick and Daniel, 2006). EMG recordings from the upper mesothoracic second pleurodorsal muscle (PD-II-U) were used in this experiment (see Figure 5.3).

5.1.2 The Mobile Robot

A Palm Pilot Robot Kit (PPRK) from Acroname Robotics was used in this experiment and is shown in Figure 5.4. The kit's name comes from the fact that the platform has a deck sufficiently big to mount a Palm Pilot or other PDA, but it does not require one. This robot has 3 wheels with holonomic movement capability that are driven by three servos. It also has three distance sensors. The system is controlled by a BrainStem General Purpose 1.0 module also from Acroname Robotics. This module has 5 analog inputs (with a 10-bit ADC), and 5 digital inputs.

5.1.3 The Interface

The interface in this system consists of two boards: the first prototype board explained in Section 3.4.1, and an external data acquisition board with Bluetooth capability (see Figure 5.5). This was necessary because the first prototype does not have an ADC on board. One extracellular channel of the first prototype board was used, and the output connected directly to an ADC input on the data acquisition board. A microcontroller in the acquisition board calculated three digital values that control the velocity of the robot. This calculation involved taking the average of the input biological signal over a certain (adjustable) number of samples. Then different thresholds were set for the various available velocities, and when the average went above a threshold a particular digital value was assigned. The robot moved or stopped according to those digital

FIGURE 5.2. The hawkmoth (*Manduca sexta*). This moth is a nocturnal insect with good night vision and an excellent olfactory system, for which is commonly studied. It also has different flight behaviors including fast forward flight and hovering (Hedrick and Daniel, 2006). In the experiment presented here two electrodes were used. The reference electrode was placed in the front abdomen area, and the recording electrode was placed in the upper mesothoracic second pleurodorsal muscle (PD-II-U).

AB abdomen; AES anepisternum;
AX axillary sclerite; EM epimeron;
EPS episternum; FR frenulum;
FW forewing; HW hindwing;
RE retinaculum; PS pleural sulcus;
WP pleural wing process. I prothorax;
H mesothorax; Ill metathorax.
1 "upper unit" of the mesothoracic pleurodorsal
muscle 2;
2 "middle unit" of the mesothoracic pleurodorsal
muscle 2 = II PD2m;
3 "lower unit" of the mesothoracic pleurodorsal
muscle 2;
4 unit a of the metathoracic pleurodorsal muscle 2;
5 unit b of the metathoracic pleurodorsal muscle 2;
6 unit c of the metathoracic pleurodorsal muscle
2 =III PD2c;
7, 7' location of the metathoracic pleurodorsal muscle
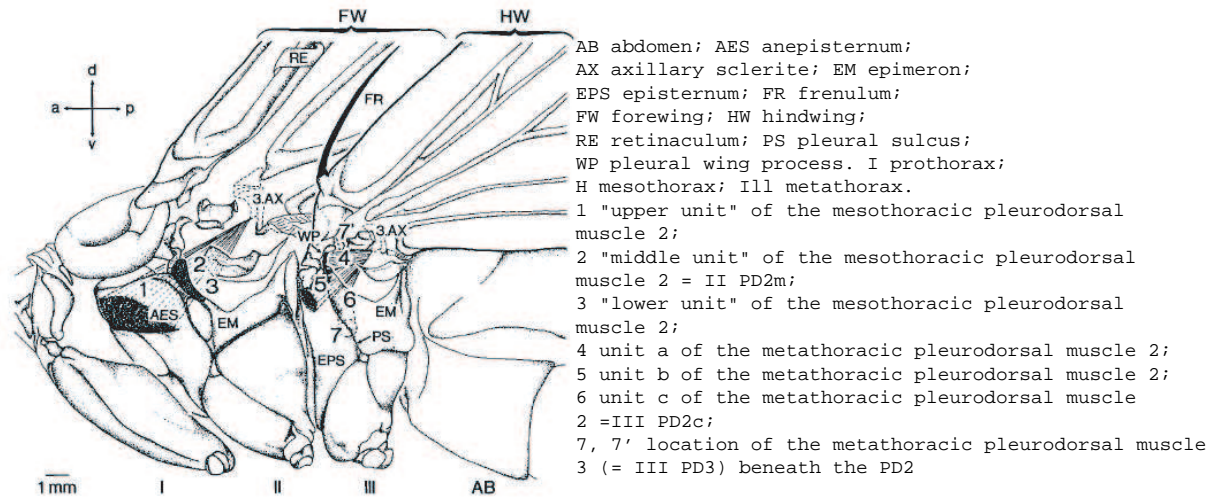3 (= III PD3) beneath the PD2

FIGURE 5.3. Hawkmoth (*Manduca sexta*) thorax. Left side view of the thorax with both wings elevated. This figure is used without permission from Wendler *et al.*, 1993.
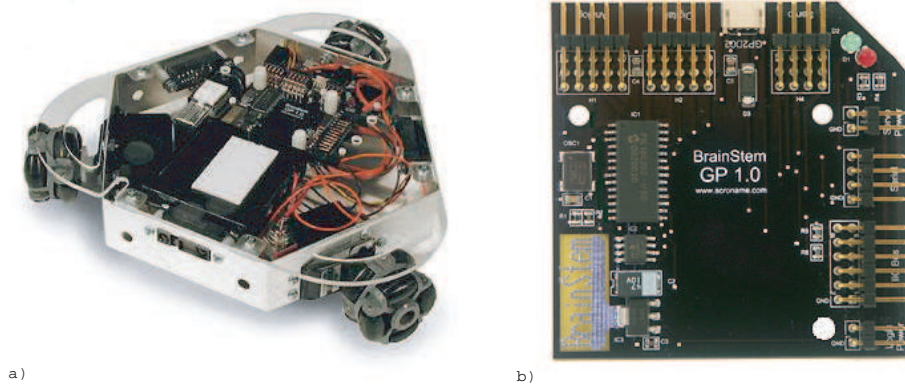

FIGURE 5.4. Robot platform. a) Palm Pilot Robotic Kit. b) BrainStem GP 1.0 Module. Photographs obtained from the Acroname Robotics website at http://www.acroname.com/.

values. Figure 5.6 shows the entire hybrid system, on a lab bench, including both boards used during the experiment. The oscilloscope shows the electrophysiological signals observed during a first test.
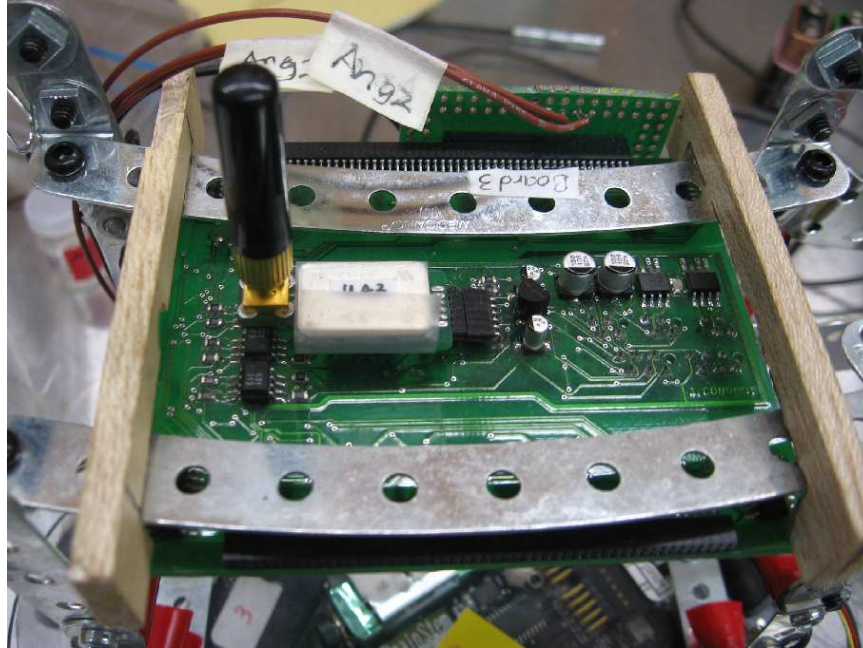

FIGURE 5.5. Data acquisition board with Bluetooth capability. This board was used to convert the biological signals into digital data by an ADC on board. Then, the information was processed by a microprocessor (also on board) to compute three digital outputs in charge of controlling the robot (velocity control).

5.2 Results

The system was tested on the floor and completely wirelessly. The hawkmoth successfully moved the robot forward everytime its wings flapped, making the robot stop as soon as the hawkmoth stopped moving. This shows the platform works as expected, allowing real-time communication between the hawkmoth and the robot. The result is an autonomous robot that does not need external control; with two more electrodes collecting data from specific cells, the system can potentially avoid collisions. Figures 5.7a and 5.7b show the system while operating front and back respectively.
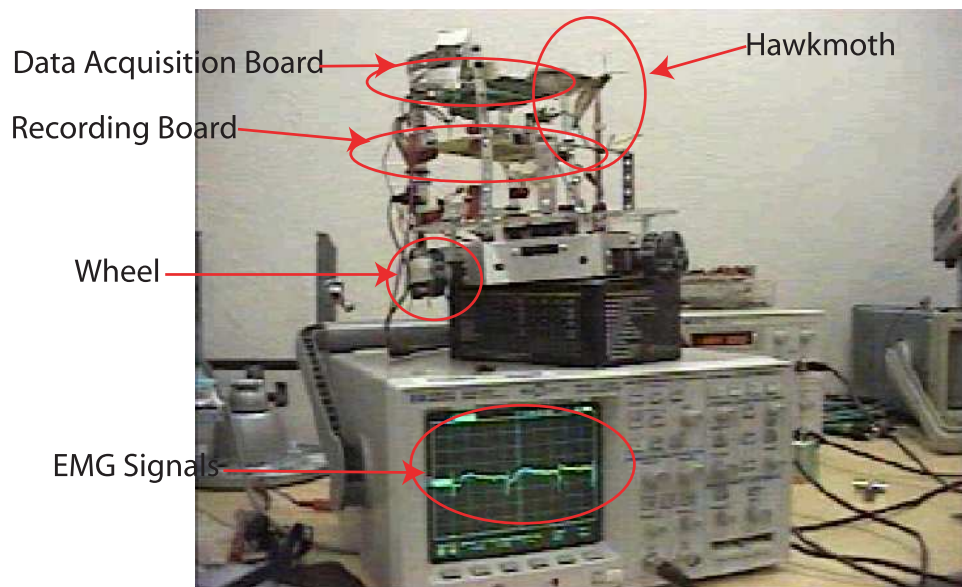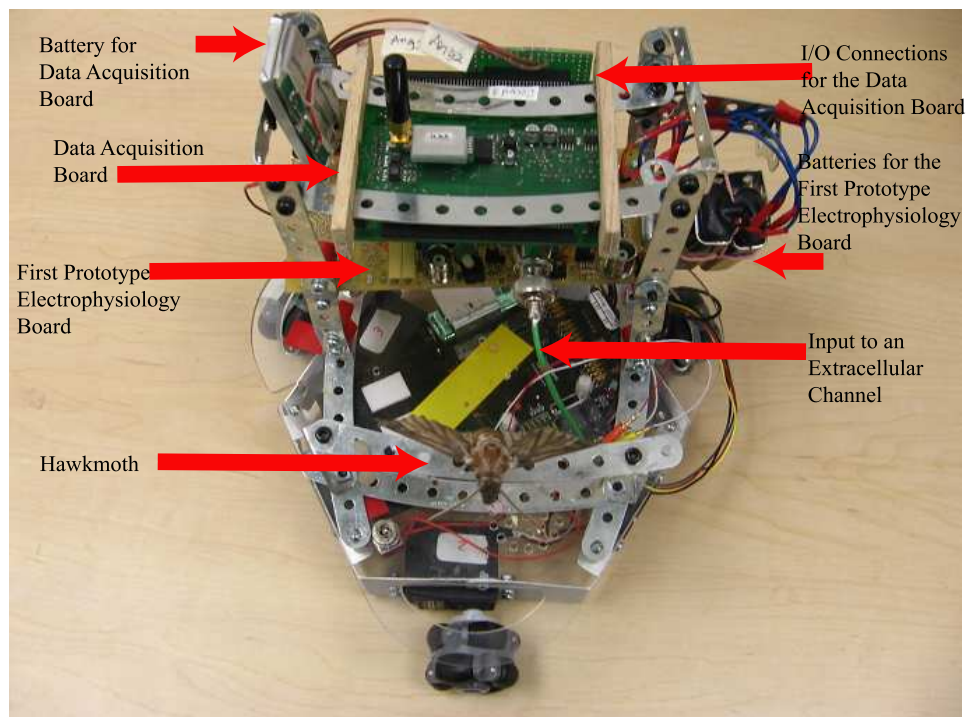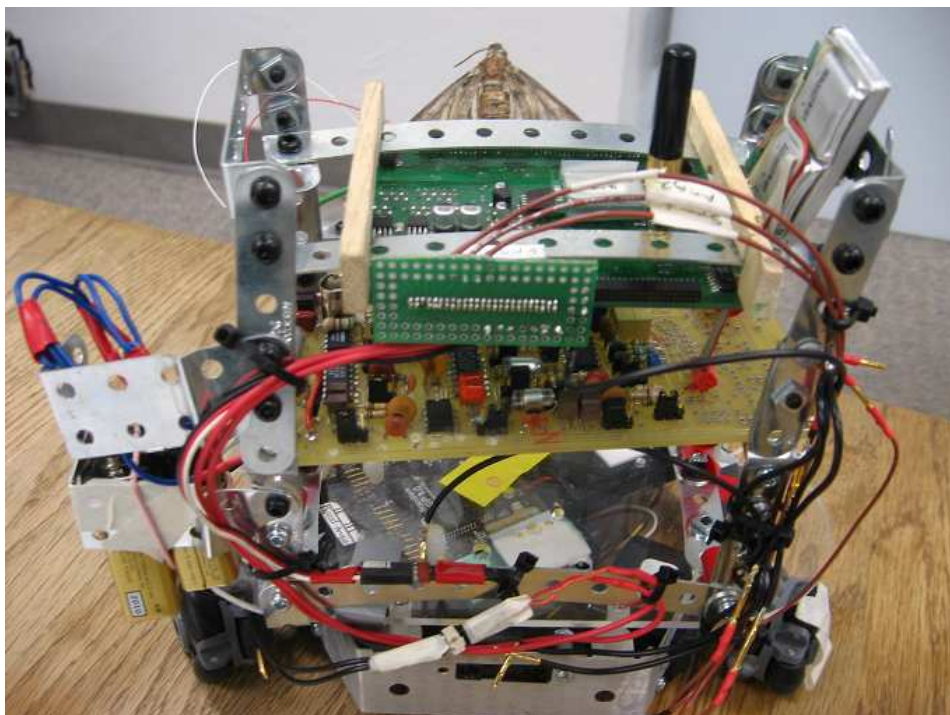
FIGURE 5.6. The hybrid biorobotic system on a lab bench. The oscilloscope shows biological data (EMGs) obtained by an extracellular channel on the first prototype.

a)

b)

FIGURE 5.7. The hybrid biorobotic system, completely wireless. a) Front view. b) Back view.

Chapter 6

Discussion

6.1 System Limitations

The most severe limitation of the current system is the number of channels on the board. With more channels recording data at the same time, more information from the insect could be obtained. Consequently, the range of experiments that could be performed would be increased. In order to add more channels while maintaining the size of the board sufficiently small for mobile robotics, components can be replaced by surface mounted devices (SMD) like SOIC, QSOP, or TSSOP, which take less than half the size of regular components. An SMD version of the second prototype has already been laid out, but that version has not been fabricated.

6.2 Future Work

There are some improvements that can be made to the board that will involve adding components to the system and might increase the size of the board. Ultimately, the board should be fabricated with SMD components and multiple layers so that the following improvements can be achieved in a relatively small board.

6.2.1 Stimulus Circuitry

Electrophysiology is usually performed in conjunction with stimulation. In intracellular recording, stimulation is used to directly test the excitability of a given cell or to measure its biophysical properties (Dichter, 1973). Stimulation can be achieved by injecting current into a cell. In general, having control of the stimulus that activates a neuron which is being recorded is obviously a powerful thing. It also means there are less unknown variables in closed-loop experiments which usually involve stimulation. Adding a stimulator to the current board would be a logical extension to this project since it would broaden the range of experiments that can be performed using this platform. Things to be considered when doing this mainly have to do with the interference caused by the stimulator to the rest of the recording device. Therefore isolation is very important especially when recording is being performed from cells close to the stimulation. Stimulation can also be provided using the same electrode used for recording. This can be achieved by forming a Wheatstone bridge with the electrode, two big resistors and a potentiometer (Dichter, 1973) as shown in Figure 6.1. The idea is that, if the bridge is balanced, the stimulating current will not affect the recording potential.
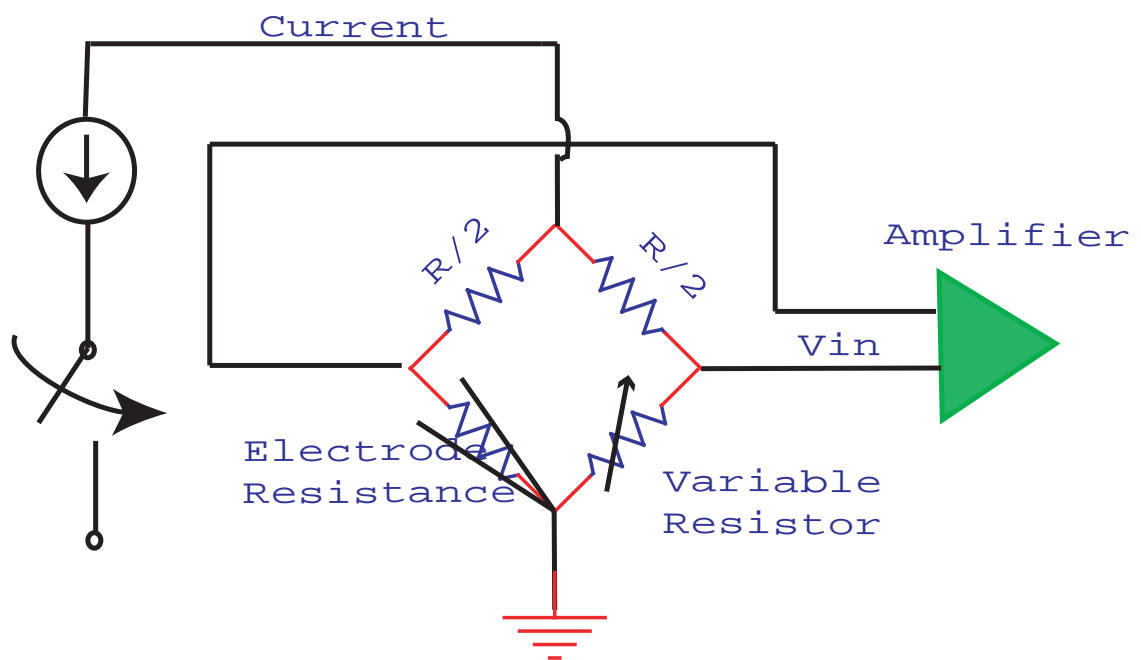
FIGURE 6.1. Wheatstone bridge configuration for stimulation and recording using one electrode. This configuration will "subtract" the potential across the electrode caused by the injected current (stimulus) leaving only the "true" potential in the cell. This is accomplished by using the principle of a Wheatstone bridge were the electrode represents one "leg", and a variable resistor is adjusted until the bridge is balanced. This figure was modified from a figure in Dichter, 1973.

6.2.2 Tunable Notch Filter

The present board contains a fixed 60 Hz notch filter that works pretty well in the USA, but when the board was tested in Australia which has power line frequencies of 50 Hz the notch filter was of no use anymore. A tunable notch filter could be implemented so that the board can be successfully used regardless of the place.

6.3 Summary

The current platform can be used to test theoretical models, previously simulated in a computer, in a real environment. The first prototype can be used to perform reliable electrophysiology in four channels simultaneously (2 extracellular and 2 intracellular), and in conjunction with a data acquisition board, it can be used in mobile robotics. The second prototype can be used as a complete interface between artificial systems and biological systems. It can perform electrophysiology in three extracellular channels, and the biological data can be digitized by an internal 10-bit ADC. The microprocessor on board can be programmed with biological algorithms to be tested, and it can be used to output command signals that can control a mobile robot.

References

Ando, N., I. Shimoyama, and R. Kanzaki (2002). Radio-telemetric recordings of flight muscle activities during flight of sweet potato hornworm, *Agrius convolvuli*. *Journal of Neuroscience Methods* 115: 181–187.

The Axon Guide (1993). *The Axon Guide for Electrophysiology and Biophysics Laboratory Techniques*. Axon Instruments, Inc.

Banks, D. J., W. Balachandran, P. R. Richards, and D. Edwins (2002). Instrumentation to evaluate neural signal recording properties of micromachined microelectrodes inserted in invertebrate nerve. *Physiological Measurement* 14: 437–448.

Buchwald, J. S., S. B. Holstein, and D. S. Weber (1973). Multiple unit recording: Technique, interpretation, and experimental applications. In *Bioelectric Recording Techniques*, Vol. I of *Methods in Physiological Psychology*, chapter 1, pp. 201–238. Academic Press, Inc. (London).

Bures, J. (1962). *Electrophysiological Methods in Biological Research*. Czechoslovak Academy of Sciences, Praha.

Calvert, J.B. (2001). Filters. `http://www.du.edu/ etuttle/electron/elect15.htm.`

Chapin, J. K. (2004). Using multi-neuron population recordings for neural prosthetics. *Nature Neuroscience* 7(5): 452–455.

Dichter, M. A. (1973). Intracellular single unit recording. In *Bioelectric Recording Techniques*, Vol. I of *Methods in Physiological Psychology*, chapter 1, pp. 3–21. Academic Press, Inc. (London).

Du Bois (2006). Emil Heinrich Du Bois-Reymond. Obtained from the Encyclopedia Britannica `http://search.eb.com/eb.com/eb/article-9031292`.

Eichman, A., W. Tripp, and M. Edwards (2000). Tobacco hornworm/carolina sphinx moth. `http://bugs.clemson.edu/museum/moths/local/moth1.htm`.

Giszter, S. F., C. B. Hart, U. I. Udoekwere, S. Markin, and C. Barbe (2005). A real-time system for small animal neurorobotics at spinal or cortical levels. In *2005 2nd Intl. IEEE/EMBS Conference on Neural Engineering*, pp. 450–453, Arlington, Virginia.

Hedrick, T. L. and T. L. Daniel (2006). Flight control in the hawkmoth *Manduca sexta*: the inverse problem of hovering. *Journal of Experimental Biology* 209: 3114–3130.

Jackson, A., C. T. Moritz, J. Mavoori, T.H. Lucas, and E. Fetz (2006). The neurochip BCI: Towards a neural prosthesis for upper limb function. *IEEE Transactions on Neural Systems and Rehabilitation Engineering* 14(2): 187–190.

Land, B. R., R. A. Wyttenbach, and B. R. Johnson (2001). An inexpensive high performance amplifier and electrode for extracellular recording. *Journal of Neuroscience Methods* 106: 47–55.

Mavoori, J., M. Bjorn, J. Longnion, T. Daniel, and C. Diorio (2004). A miniature implantable computer for functional electrical stimulation and recording of neuromuscular activity. In *IEEE Intl. Workshop on Biomedical Circuits and Systems*, Singapore.

Miller, T.A (1979). *Insect Neurophysiological Techniques.* Springer-Verlag.

National Semiconductors LM13700 datasheet (1999). Lm13700/lm13700a: Dual operational transconductance amplifiers with linearizing diodes and buffers. `http://www.national.com`.

Neihart, N.M. and R.R. Harrison (2005). Micropower circuits for bidirectional wireless telemetry in neural recording applications. *IEEE Transactions on Biomedical Engineering* 52: 1950–1959.

Obeid, I., J. C. Morizio, K. A. Moxon, M. A. L. Nicolelis, and P. D. Wolf (2003). Two multichannel integrated circuits for neural recording and signal processing. *ieeebme* 50: 255–257.

Purves, R.D. (1981). *Biological Techniques Series. Microelectrode methods for intracellular recording and ionophoresis.* Academic Press, London, UK.

Pyk, P., S. Badia, U. Bernardet, P. Knüsel, M. Carlsson, J. Gu, E. Chanie, B. S. Hansson, T. C. Pearce, and P. M. F. J. Verschure (2006). An artificial moth: Chemical source localization using a robot based neuronal model of moth optomotor anemotactic search. *Journal of Autonomous Robots* 20(3): 197–213.

Reger, B. D. (2000). A Neuro-robotic Interface for the Study of Synaptic Plasticity in Sensorimotor Adaptation. Ph.D. dissertation, Department of Mechanical Engineering, Northwestern University, Evanston, Illinois.

Reger, B. D., K.M Fleming, V. Sanguineti, S. Alford, and F. A. Mussa-Ivaldi (2000). Connecting brains to robots: The development of a hybrid system for the study of learning in neural tissues. In *Proc. of the 7th Intl. Conf. on Artificial Life*, pp. 263–272.

Rivera-Alvidrez, Zuley (2004). Design of analog filtering circuits for intracellular and extracellular insect electrophysiology. Unpublished Independent Study Report.

Rogers, C. L. and J. G. Harris (2004). A low-power analog spike detector for extracellular neural recordings. *IEEE Intl. Conf. on Electronics, Circuits and Systems* pp. 290–293.

Smith, L. S. and N. Mtetwa (2006). Manual for the noisy spike generator MATLAB software. University of Stirling, Scotland, UK.

Snodderly, M. D. (1973). Extracellular single unit recording. In *Bioelectric Recording Techniques*, Vol. I of *Methods in Physiological Psychology*, chapter 6, pp. 137–162. Academic Press, Inc. (London).

Thomas, M. (1997). Optopatch manual: Capacitance and resistance compensation. `http://www.cairnweb.com/menus/menustub-technotes.html`.

Towe, A. L. (1973). Sampling single neuron activity. In *Bioelectric Recording Techniques*, Vol. I of *Methods in Physiological Psychology*, chapter 4, pp. 79–93. Academic Press, Inc. (London).

Wendler, G., M. Müller, and U. Dombrowski (1993). The activity of pleurodorsal muscles during flight and at rest in the moth *Manduca sexta* (l.). *Journal of Comparative Physiology A: Sensory, Neural, and Behavioral Physiology* 173(1): 65–75.